ON USING HEAT FOR WATER DESALINATION AND PURIFICATION

by

SABER KHANMOHAMMADI

A dissertation submitted in partial fulfillment of the
requirements for the degree of

DOCTOR OF PHILOSOPHY IN MECHANICAL ENGINEERING

2025

Oakland University
Rochester, Michigan

Doctoral Advisory Committee:

Jonathan Maisonneuve, Ph.D., Chair
Sarah Beetham, Ph.D.
Laila Guessous, Ph.D.
Ziming Yang, Ph.D.

For a while, we became students as children
For a while, we rejoiced in our own mastery
Listen to the end of the tale and what befell us
We came from dust and turned to wind

Omar Khayyám

ACKNOWLEDGMENTS

I dedicate this work to my late father, whose memory continues to inspire me, and to my mother, whose unwavering love and support have been my greatest strength. Their sacrifices and encouragement have shaped my journey, and I am forever grateful.

I extend my deepest appreciation to my advisor, Dr. Jonathan Maisonneuve, whose steadfast guidance, mentorship, and support have been instrumental in this journey. His insightful perspectives, patience, and encouragement have not only shaped this work but have also inspired me to grow as a researcher, thinker, and scholar.

I also sincerely appreciate my dissertation committee members for their invaluable expertise, insightful feedback, and critical evaluations, which have significantly enriched this work. Their guidance has pushed me to refine my research and strive for excellence, and I deeply value their contributions to this project.

To my lab mates and colleagues, I am incredibly thankful for your companionship, thought-provoking discussions, and collaborative spirit. The shared challenges, profound brainstorming sessions, and unwavering support have made this journey not only possible but also deeply rewarding.

Finally, to my friends and family who have stood by me through this journey, your patience, understanding, and belief in me have been a source of constant motivation. This accomplishment is a testament to the collective support and inspiration I have received from each of you.

Thank you.

Saber Khanmohammadi

ABSTRACT

ON USING HEAT FOR WATER DESALINATION AND PURIFICATION

by

Saber Khanmohammadi

Adviser: Jonathan Maisonneuve, Ph.D.

The global freshwater crisis, intensified by population growth, climate change, and industrial demands, necessitates more energy-efficient and sustainable water treatment technologies. This dissertation explores how low-grade thermal energy can be harnessed to improve the performance and energy efficiency of membrane-based desalination systems. Four thermally integrated desalination strategies are investigated: thermally enhanced reverse osmosis, thermally driven reverse osmosis, membrane distillation, and ocean thermal membrane distillation.

For thermally enhanced reverse osmosis, a detailed thermodynamic analysis reveals that preheating feedwater can reduce specific energy consumption by up to 24% for seawater and 33% for brackish water desalination. While higher feed temperatures reduce pumping work by enhancing membrane permeability and reducing polarization, the trade-off with thermal input is critically analyzed to identify net energy savings under high-efficiency thermal recovery conditions. We conclude that the benefit of thermal enhancement is marginal, as it requires a substantial amount of heat input to achieve only a slight reduction in pump work.

For thermally driven reverse osmosis, a fundamentally new process is introduced where thermal energy directly drives mechanical desalination via a thermally driven piston system. A theoretical model evaluates the system's efficiency under various design parameters, demonstrating competitive performance compared to conventional thermal methods when optimized for low-grade heat sources.

A feasibility study of an ocean thermal membrane distillation (OTMD) system is conducted for application in remote islands, using cold deep-sea water as a thermal sink. Experimental and theoretical studies show that under optimized conditions, the OTMD system can outperform conventional reverse osmosis (RO) systems in specific energy consumption, offering a low-carbon, resilient solution for water-scarce regions.

Finally, for membrane distillation, performance is further enhanced through real-time control strategies that adjust operating parameters, feed temperature, flow rates, and distillate conditions, to reduce specific energy consumption. Experimental results from a lab-scale direct contact membrane distillation system validate the proposed control method and report specific thermal energy consumptions of 274 kWh/m^3 which is significantly lower than those reported in the literature.

Overall, this dissertation demonstrates that, if properly integrated, heat can significantly reduce the energy use of membrane desalination systems, especially in locations with access to waste heat, solar thermal, or ocean thermal gradients.

TABLE OF CONTENTS

TABLE OF CONTENTS—Continued

TABLE OF CONTENTS—Continued

TABLE OF CONTENTS—Continued

TABLE OF CONTENTS—Continued

TABLE OF CONTENTS—Continued

LIST OF TABLES

LIST OF FIGURES

NOMENCLATURE

A	area (m^2)
A_0	constant
B_0	constant
C	constant
C_0	constant
c	concentration (mol m^{-3})
cp	specific heat (J/kg.K)
cop	coefficient of performance
E	energy (J)
GOR	gain output ratio
H	enthalpy (J)
h	specific enthalpy (J/kg)
i	number of ions
K	dimensionless ratio
m	mass (kg)
n	number of time intervals
p	pressure (Pa)
p_g	gage pressure (Pa)
Q	heat (J)
q	specific heat (kWh/m^3)
R	gas constant (J/mol.K)

r	recovery ratio
t	time (s)
T	temperature (K)
U	internal energy (J)
u	specific internal energy (J kg-1)
V	volume (m^3)
v	molar volume (m^3/mol)
v	specific volume (m^3 kg^{-1})
ΔV	permeate volume (m^3)
W	work (J)
w	specific work (kWh/m^3)

Subscripts and Superscripts

'	working fluid
*	point of minimum heat
1	initial state
2	final state
atm	atmosphere
cr	critical
D	distillate
F	feed
f	saturated liquid

g	saturated vapor
I	first law
II	second law
in	membrane inlet
max	maximum
min	minimum
net	net
out	membrane outlet
p	permeate
sat	saturation

Greek symbols

Δ	difference over time
λ	sizing ratio
η	efficiency
π	osmotic pressure (Pa)

CHAPTER ONE

INTRODUCTION

1.1 Motivation

According to the United Nations World Water Development Report 2023, approximately 2 to 3 billion people in the world face water scarcity [1]. This challenge is intensified by growing population, climate change and urbanization which put a lot of pressure on water resources. The agricultural sector which utilizes 70% of world freshwater withdrawals is experiencing more pressure due to the rising population. This sector's water usage is anticipated to grow by about 19% by 2050 to meet the food demands of people. Simultaneously, it is anticipated that other sectors, including industries and energy, will experience a high rise in water usage, which will be nearly 400% [2], [3].

In the United States, water needs are considerable and diverse, reflecting the country's large population, industrial base, and agricultural demands. On average, the U.S. consumes 322 billion gallons of water per day, with 87% coming from freshwater sources. The largest shares of this water use belong to thermoelectric power generation (41%), irrigation (37%) and domestic use (12%) respectively [4], [5]. One of the challenges that the U.S. is dealing with is providing the water needs in remote islands like Hawaii, American Samoa, and the U.S. Virgin Islands. For example, in Hawaii some islands like Oahu which are facing a severe water shortage significantly rely on underground aquifers which take a long time to be replenished. Or in American Samoa, water use is estimated at round 11 million gallons per day mostly coming from

groundwater wells. This region despite its tropical climate, is facing significant water challenges due to aging infrastructure, contamination of water sources and other factors [6], [7], [8].

1.2 Desalination

Desalination methods have been in use for thousands of years, with roots dating back to ancient civilizations. In the 4th century BCE, Greek sailors used woolen condensers to distill seawater, and the philosopher Aristotle described ideas regarding the water cycle and a distillation process in the 3rd century BCE. The first large-scale land-based desalination plant was set up in Tunisia in 1560, producing a daily capacity of up to 40 barrels of freshwater per day [9].

Significant advancements in desalination technology occurred during the industrial revolution. A vertical tube seawater distillation apparatus was patented in 1852, and it soon became widespread for shipboard use. The 20th century witnessed a faster rate of development in desalination technology that resulted in the invention of multi-effect flash and multi-stage flash methods. The history of desalination was marked by another significant development in the 1960s when reverse osmosis (RO) membranes were discovered by Sydney Loeb [10]. The first RO plant developed for commercial use was built in Coalinga, California, in 1965. It confirmed the promise of RO as it highlighted its advantages compared to existing methods, such as being more efficient, operating at room temperature, and being scalable [9].

By the early 2000s, there were over 2,000 desalination plants in use globally, showing the rapid adoption of this technology. This progress accelerated more, and by 2020, there were over 22,000 desalination plants in use, showing its central place in mitigating water

shortages. Among these advancements, large-scale projects such as the Ras Al Khair desalination plant in Saudi Arabia, the world's largest with a capacity of 1,401,000 m^3/day, show this trend [9].

The U.S. desalination market is estimated to reach $2.63 billion by 2028, growing at a rate of 8.30% from 2023 to 2028 [11]. California, Texas, and Florida are leading states in the U.S. desalination market, due to various challenges they have including water scarcity and the need for alternative water sources. These states have significantly invested in desalination to ensure water security. As of August 2024, Texas operates 60 municipal desalination plants treating brackish groundwater, surface water, and reclaimed water, designed to produce about 172 million gallons per day [12].

1.3 Desalination Technologies

Desalination technologies can be broadly categorized based on their primary energy sources, such as thermal, electrical, or renewable energy. These categories help distinguish between methods like multi-effect distillation, reverse osmosis, and solar-driven processes. Figure 1.1 illustrates the categorization of desalination technologies based on their primary energy sources.

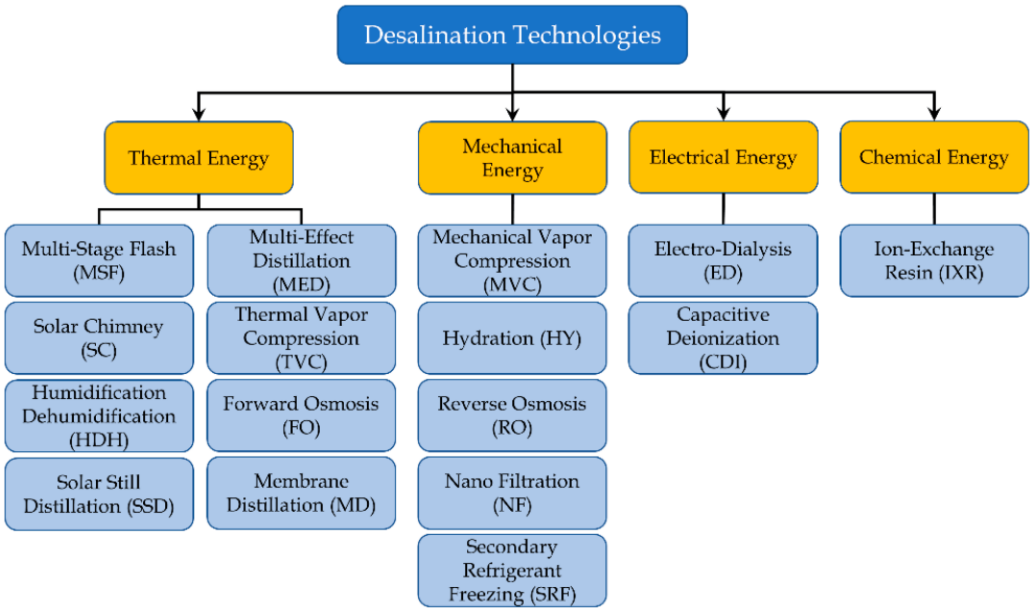

Figure 1.1 Classification of desalination technologies based on the primary energy source used for water treatment [13].

Reverse osmosis (RO) is a common desalination technology applied globally, which is both efficient and scalable. The process involves the application of high pressure on brackish to let it flow through a semi-permeable membrane that selectively filters dissolved salts and impurities (Figure 1.2). RO has several advantages like production of high-quality water with minimal total dissolved solids, low energy consumption compared to thermal desalination methods, and suitability for scaling up for different uses. On the other hand, it does have some drawbacks like the requirement for high pressure and energy input, an enormous brine disposal problem, and deterioration of the membranes with time, which adds to the maintenance cost. RO is one of the most energy-efficient desalination technologies available today. The theoretical minimum energy consumption for RO is 1.07 kWh/m^3, while typical commercial RO plants require 3 to 10 kWh/m^3 [14]. Advancements in technology have significantly reduced energy

consumption, with some modern sea water RO plants achieving as low as 2.5 kWh/m³ [15].

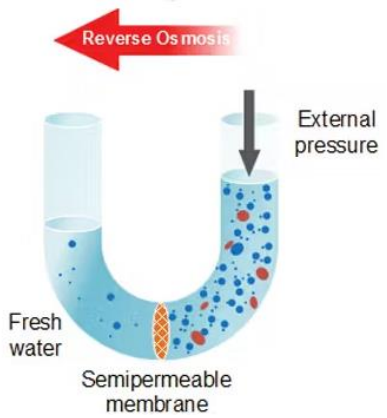

Figure 1.2 Schematic representation of the reverse osmosis process, where applied pressure forces saltwater through a semi-permeable membrane, separating contaminants and producing fresh water [16].

A second major desalination technology is multi-stage flash (MSF) distillation, which works on the principle of flash evaporation, where water is rapidly vaporized by reducing pressure rather than increasing temperature. The process involves several stages as shown in Figure 1.3. Seawater is heated to 90-110 °C under high pressure then the heated water passes through multiple stages with decreasing pressure. In each stage, a portion of the water rapidly vaporizes (flashes) due to the pressure drop, and the vapor is condensed on cooling tubes. At the end, the condensed fresh water is collected as the product. Some of the advantages of this system include high reliability for large-scale desalination, producing high-quality water with low total dissolved salt, and capability of integration with power plants to efficiently utilize waste heat. These systems also have some disadvantages including substantial thermal energy requirement, making them less energy-efficient than membrane-based processes like RO. They have high capital cost and also their high operating temperatures can cause corrosion and scaling. In terms of

energy consumption, MSF requires significant energy compared to common desalination systems like RO. Combining thermal and electrical energy requirements, the total specific energy consumption for MSF systems is reported to be in the range of 80-120 kWh/m³ plus electrical energy of 1.5-4 kWh/m³ [17].

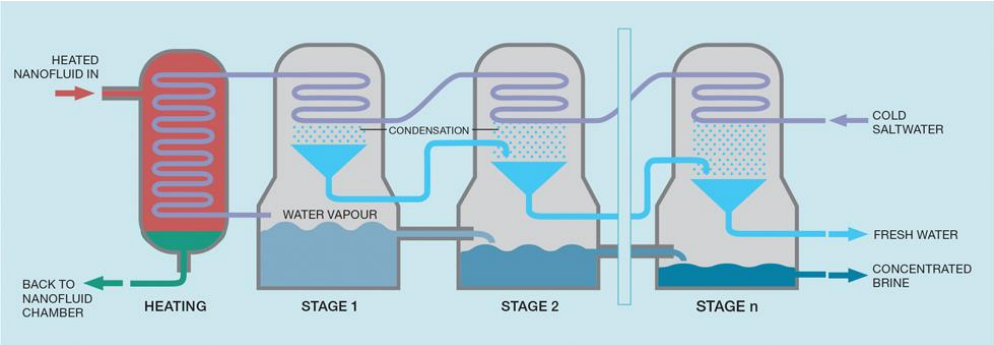

Figure 1.3 Schematic representation of a multi-stage distillation process where water vapor is condensed to produce fresh water while concentrating brine [18]

A third major desalination technology is multi-effect distillation (MED) which is another thermal process that uses multiple stages (effects) to efficiently distill seawater. Each effect is a separate chamber where water is evaporated and condensed. Steam from one effect is used to heat water in the next effect. The process operates at lower temperatures and pressures in each subsequent effect. Multi-effect distillation is more energy-efficient than multi-stage flash distillation and can use low-temperature heat sources. Multi-effect distillation plants typically have 2-16 effects and can produce high-quality distilled water. Based on the reports MED systems usually consume around 14-21 kWh/m^3 which is lower than MSF technology [19]. This lower specific energy consumption could be attributed to efficient use of heat, and lower operational temperature in MED systems.

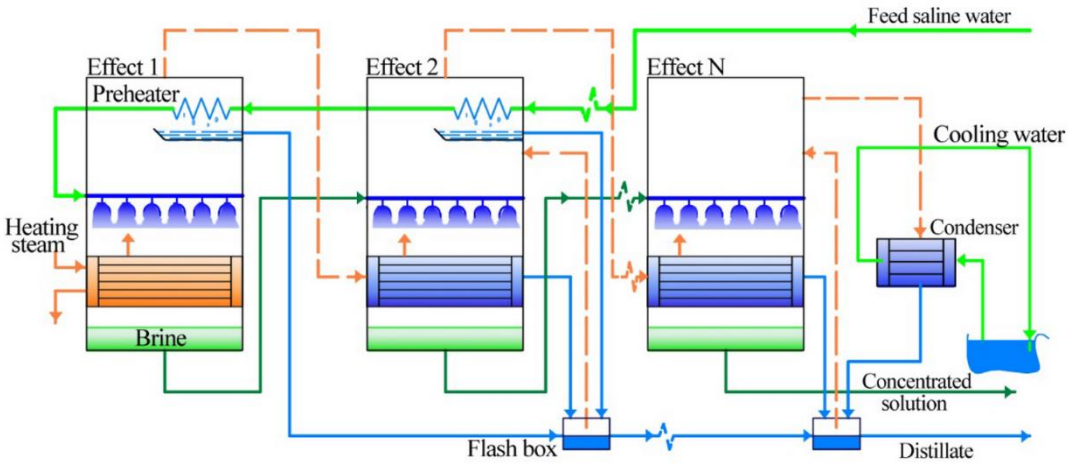

Figure 1.4 Schematic representation of a multi-effect distillation (MED) system, where heating steam drives evaporation and condensation stages to produce fresh water while concentrating brine [20].

A fourth more recent desalination technology is membrane distillation (MD) which is a thermally driven process that uses a hydrophobic microporous membrane to facilitate the separation of vapor from water. As indicated in Figure 1.5, a temperature difference across the membrane causes a gradient in vapor pressure. Water vapor travels through the membrane pores and subsequently condenses on the low-temperature side. MD is operated at temperatures lower than other thermal processes and can achieve up to 99.9% rejection of non-volatile compounds, yielding high-quality water. MD can be driven by renewable energies or low-grade waste heat, e.g., solar thermal. The absence of high hydraulic pressure lowers membrane fouling compared to pressure-driven processes, and MD is particularly effective in the treatment of very concentrated hypersaline solutions and brines. On the other hand, there are some limitations for MD systems including membrane wetting in long-term operation which lead to reducing separation efficiency, and lower water production rates compared to pressure-driven membrane processes. The specific energy consumption in MD systems varies depending on the system configuration and operating conditions. Based on the available literature, the specific

energy consumption for different MD configurations fall within the ranges of 100-1600 kWh/m^3 [21].

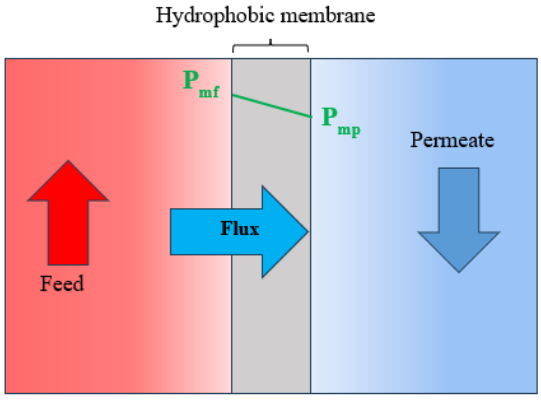

Figure 1.5 Schematic representation of a direct contact membrane distillation (DCMD), where a hydrophobic membrane allows vapor flux from the heated feed side to the permeate side, driven by a transmembrane vapor pressure gradient.

1.4 Low-Grade Heat

It is estimated that 72% of the world's primary energy is lost after conversion. More specifically, 63% of the waste heat flows are at temperatures less than 100 °C, with most originating from electricity generation, followed by transportation and industry [22]. Despite its vast availability, this thermal energy is not effectively harnessed for practical applications. For instance, industrial waste heat in the European Union is estimated to reach around 300 TWh annually, excluding contributions from power generation and transportation sectors [23]. In the US, power plant condensers release nearly 4000 TWh of waste heat each year, mainly in the temperature range of 40–49 °C [24].

Another low-temperature source that can be utilized is geothermal energy. This energy source is a great potential of low-grade heat for use in different applications. This renewable resource is based on the thermal energy stored within the earth and can be exploited in various ways depending on the temperature of the geothermal source. Low-

temperature geothermal resources are those with temperatures no greater than 150 °C [25]. These resources are more widely available than high-temperature geothermal sources and can be used for various applications including direct use in heating and cooling systems, small-scale power generation, and industrial processes [26]. Using geothermal energy would have a wide range of advantages like high availability, low CO_2 emissions compared to conventional heating and cooling methods, and extensive application in rural and urban areas. While there is huge potential in low-temperature geothermal resources, some of the challenges they face are economic feasibility, especially for electricity generation from lower temperatures, site-specific design needs and experience in system operation, and capital investment in the developing infrastructures [27], [28], [29].

In addition to industrial and geothermal sources, another promising reservoir of low-grade heat is ocean thermal gradients. The Ocean thermal gradient refers to a difference in temperature between the warm surface ocean waters and the cold deep ocean waters. This natural phenomenon forms the basis for ocean thermal energy conversion technology. The ocean thermal gradient typically comprises warm surface waters at approximately 25-30 °C in tropical waters and cold deep waters at approximately 4-7 °C at depths of around 1000 meters. The gradient is relatively consistent throughout the year, which makes it a potentially consistent energy source [30], [31].

1.5 Objectives and Outline

The goal of this work is to examine the role of thermal energy in improving the efficiency and performance of membrane-based desalination processes. To achieve this goal, we investigate how heat can be leveraged in three specific desalination

technologies: (1) thermally enhanced reverse osmosis, (2) thermally driven reverse osmosis, (3) membrane distillation. Each of these processes has particular opportunities and challenges for the application of low-grade or waste heat, with the aim of reducing energy consumption and improving the efficiency of water production. Harnessing low-grade thermal energy, which is readily obtained from sources like industrial waste heat, solar thermal energy, and geothermal energy, is a promising approach to improving water treatment plants sustainability. Successful integration of low-grade heat with desalination and membrane-based water treatment systems can greatly improve energy efficiency and sustainability with less reliance on fossil-fuel-based energy sources. Through a combination of thermodynamic analysis, experimental validation, and numerical modeling, we investigate three specific methods of using heat in desalination.

This study is framed around the following critical research questions, which guide the analysis and methodologies used to evaluate different desalination technologies: How does feedwater temperature affect the performance and energy requirements of reverse osmosis systems? Can thermal energy be directly used to drive the RO process through innovative configurations such as thermally driven reverse osmosis (TDRO)? Is it feasible to use ocean thermal gradient for driving membrane distillation systems? What are the most effective strategies for enhancing the energy efficiency of MD systems through operational control?

Findings and methods are organized into the following chapters, each addressing an important aspect of integrating thermal energy into membrane desalination systems:

Chapter Two evaluates the potential of using thermal energy to enhance reverse osmosis (RO) desalination systems by examining the effects of feedwater temperature on

water flux, energy requirement, permeate quality, and operation pressures. Through this study the overall energy balance of thermally enhanced RO is examined for the first time, including the trade-off between mechanical pump work saving and supplementary thermal energy input.

In Chapter Three a detailed investigation of thermally driven reverse osmosis (TDRO) as a novel approach to desalination, leveraging low-grade heat to drive the separation process is investigated. The study explores the thermodynamic limits of TDRO, comparing its performance with conventional desalination methods such as reverse osmosis (RO) and thermal desalination. A theoretical model is developed to quantify the energy requirements and efficiency of the process, including key design parameters.

In Chapter Four, a feasibility study is conducted to evaluate the integration of ocean thermal energy with membrane distillation technology, referred to as the ocean thermal membrane distillation (OTMD) system. The study explores the potential of utilizing deep seawater as a cold source to drive the direct contact membrane distillation process specifically in remote islands like American Samoa. Both theoretical and experimental investigations are performed to determine water production rates, specific energy consumption, and mechanical work associated with different cold water pumping configurations. A lab-scale test bench is developed to identify key performance metrics under controlled perturbations in flow rate and temperature. By analyzing the thermal and hydraulic behavior of the system, the objective is to identify viable OTMD designs that have lower energy requirements and show a specific energy consumption less than commonly used reverse osmosis systems.

In Chapter Five, an experimental investigation is conducted to explore strategies for controlling operating conditions to enhance the energy efficiency of a direct contact membrane distillation (DCMD) system. This study focuses on monitoring and adjusting operational system parameters including feed temperature, feed flow rate, and distillate flow rate, to optimize performance. By carefully adjusting these variables, the objective is to reduce specific energy consumption and specific work, ensuring that the process approaches maximum efficiency. Finally, the results will identify a locally optimal set of operating conditions, where the system reduces energy consumption while maintaining the highest possible permeate flux.

CHAPTER TWO

REDUCING THE SPECIFIC ENERGY USE OF SEAWATER DESALINATION WITH THERMALLY ENAHNCED REVERSE OSMOSIS

2.1 Introduction

In recent years, there has been renewed interest in harnessing thermal energy for water desalination [32]. Thermal energy from sources such as solar radiation, ocean thermal gradients, geothermal, and power plant waste heat is abundant and represents a tremendous resource for improving the sustainability of water infrastructure. This has led to advances and innovation in a number of thermally-driven desalination technologies, such as membrane distillation [33], multi flash distillation [34], and thermally driven RO [131]. In all such technologies, heat is used as the primary energy source and driver. Also, the possibility of using heat to thermally enhance RO has also been considered, wherein small amounts of heat could be used to pre-heat RO feed water, incoming water supplied to the system that needs to be purified by removing dissolved salts and other impurities, in order to improve RO performance [36], [37]. The concept of thermally-enhanced RO is largely motivated by the fact that warmer feed water permeates more quickly across a RO membrane [38], [39], [40], [41], making it possible to produce more water with a given unit of mechanical work. For example, some studies have shown mechanical energy savings of up to 12 % when seawater feed is heated from 15 to 45 °C, and up to 45 % when brackish water feed is heated from 15 to 45 °C [38], [42]. This is mostly the result of an apparent increase in the membrane permeability that is caused by lower feed viscosity as a function of temperature [40], [43]. The other advantage of warm

feed is that high permeability facilitates operation at lower applied pressures, which is helpful for mitigating the risks of membrane mechanical failure and membrane fouling [44], [45]. For these reasons, it is generally agreed that RO operation in warm climates is more favorable [46], [47]. However, it is less clear whether it is advantageous to use an external source of thermal energy to preheat RO feed water. In such a case, the energy savings from reduced pumping work (and associated cost savings) would need to outweigh the thermal energy input (and associated costs). To date, this balance between thermal energy input and mechanical pump savings for thermally enhanced RO has not yet been considered in the literature. Also unclear is whether the energy saving benefits of thermally-enhanced RO outweigh the disadvantages, including increased reverse salt flux and permeate concentration, loss of membrane structural integrity, and increased scaling [38], [39].

In this chapter, we investigate the process of thermally enhanced RO and analyze the tradeoff between thermal energy input and mechanical pump savings. A transport model is developed and used to establish the energy balance of both conventional RO and thermally enhanced RO. This is the first time that thermal energy input has been included in the overall energy balance analysis of thermally enhanced RO. Parametric analysis is conducted across a range of conditions to identify under what circumstances the resulting energy balance is favorable. RO application to a number of different feed water sources is considered, including seawater, brackish water, and oil and gas produced water. Other variables include different membrane properties (permeability and selectivity), different operating targets (water permeate rates and feed recovery ratios), different equipment specifications (thermal and mechanical efficiencies), and different environmental

conditions (ambient temperatures). Recommendations are provided for future applications of thermally enhanced RO.

2.2 Theory

2.2.1 Energy Balance of Reverse Osmosis

In a standard RO system, concentrated feed solution is introduced to a membrane module and then pressurized above the osmotic pressure (defined as the pressure needed to counteract natural solvent flow), to drive clean water permeate across the membrane for collection. A standard RO system is illustrated in Figure 2.1. The energy consumption of RO is related to the pumping power that is required to pressurize the feed solution above its osmotic pressure potential. To reduce this pumping load and improve energy efficiency, pressure from the super-concentrated waste brine (which is defined as the super-concentrated water volume left after desalination) is typically recycled back to the incoming feed via a mechanical pressure exchanger.

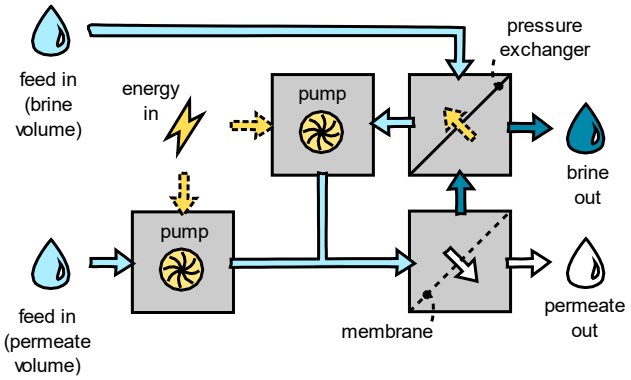

Figure 2.1 Schematic of a standard reverse osmosis (RO) desalination plant. Energy is supplied for mechanical pumping to pressurize feed solution above its osmotic potential, and thereby drive clean water permeate across the membrane.

The energy performance of RO can be conveniently expressed in terms of specific work input w_{RO}, which is defined as the pump work W_{RO} per unit volume of water permeate that is collected V_P. As described in equation (2.1) and as illustrated in Figure

2.1, the pumping load can be distributed between two pumps, with one to handle a portion of the feed equal to the permeate volume, and another to handle a portion equal to the brine volume. This configuration facilitates the integration of the pressure exchanger for recovering mechanical work from the pressurized brine solution and recycling it back to the incoming feed. The work requirements of both of these pumps, $\dot{w}_p$ and $\dot{w}_B$, are defined in equations (2.2) and (2.3), and a detailed derivation of both expressions is provided in Supplementary Note 2.1.

$$\dot{w}_{RO} = \frac{\dot{W}_{RO}}{\dot{V}_P} = \dot{w}_P + \dot{w}_B \tag{2.1}$$

$$\dot{w}_P = \frac{1}{\eta_{pump}} \Delta p \tag{2.2}$$

$$\dot{w}_B = \frac{1}{\eta_{pump}} \left(\frac{1}{r} - 1\right) \Delta p \left(1 - \eta_{pex}\right) \tag{2.3}$$

Where η_{pump} is the pump efficiency, η_{pex} is the efficiency of the pressure exchanger, and r is the recovery ratio, which is the ratio of the permeate volume relative to the feed volume (i.e. $r = \dot{V}_P / \dot{V}_F$), and Δp is the applied pressure.

Applied pressure Δp is an operating parameter that can be controlled to achieve certain targets for the RO plant. For example, it may be desirable for the RO plant to achieve a high recovery ratio so that excessive volumes of feed are not handled, although this will increase the specific energy use, as shown later on. Or it may be desirable for the RO plant to maintain a certain rate of water permeate production per unit of membrane surface area, which will be proportional to the plant's return on investment, also shown later on. The relationship between applied pressure and these targets is defined in equation (2.4), and an expanded derivation is provided in Supplementary Note 2.2.

$$\Delta p = \frac{\dot{V}_P}{a} A^{-1} + \Delta\pi \quad (2.4)$$

Where $\dot{V}_P / a$ is the rate of permeate water production per unit membrane surface area, A is the membrane water permeability, and $\Delta\pi$ is the osmotic pressure difference across the membrane, which can be approximated with the Van't Hoff equation.

$$\Delta\pi = i R T \Delta c \quad (2.5)$$

Where i is the number of ions, R is the gas constant, T is the absolute temperature of solution, and Δc is the concentration difference across the membrane.

Importantly, the concentration difference Δc will vary along the length of the membrane as water permeate is recovered from the feed and as salt leaks through the imperfect membrane. It will also be a function of polarization, as non-linear concentration gradients will develop normal to the membrane surface due to limited diffusivity. To account for these dynamics, a variety of 2D and 3D finite element models have been proposed in the literature [48], [49], [50]. A simplified expression is used here to describe concentration difference Δc as a function of the logarithmic mean of the concentration from inlet to outlet, and as a function of an exponential polarization factor [51], [52], [53].

$$\Delta c = \exp\left(\frac{\dot{V}_P}{a} k^{-1}\right)\left(\frac{c_B - c_F}{\ln c_B - \ln c_F}\right) - c_P \quad (2.6)$$

Where k is the mass transfer coefficient, and c_F, c_B, and c_P are concentrations of the feed, brine, and permeate respectively. While the inlet concentration c_F is set by the seawater feed source, the outlet concentrations for brine c_B and permeate c_P will be a function of the balance between water and salt permeate. Expressions for these can be

developed by taking a mass balance of salt and water permeate, and by considering the diffusion mechanism by which salt leaks towards the permeate. Expressions for both c_B and c_P are provided below, and a detailed derivation is provided in Supplementary Note 2.3.

$$c_B = \frac{c_F - r\, c_P}{1 - r} \tag{2.7}$$

$$c_P = \frac{a}{\dot{V}_P} B\, \Delta c \tag{2.8}$$

Where B is the membrane salt permeability.

Together, equations (2.1)-(2.8) describe the pump work required for a reverse osmosis system w_{RO} as a function of (i) the properties of the feed solution including concentration c_F and temperature T, (ii) the properties of the membrane including water and salt permeability A and B, (iii) the severity of polarization, which is related to the mass transfer coefficient k, and (iv) the target recovery ratio and permeate flux, r and $\dot{V}_P / a$. For reference, the thermodynamic limit of RO can be obtained from equations (2.1)-(2.8) by assuming no losses, perfect pump and pressure exchanger efficiency $\eta_{pump} = \eta_{pex} = 1$, no reverse salt leakage $B = 0$, no polarization $k \rightarrow \infty$, and a target recovery ratio and permeate rate of zero, $r \rightarrow 0$ and $\dot{V}_P / a \rightarrow 0$.

2.2.2 Energy Balance of Thermally Enhanced Reverse Osmosis

In a thermally enhanced RO system, concentrated feed solution is heated prior to being introduced to the membrane module. This decreases fluid viscosity, allowing clean water to permeate across the membrane more rapidly. Energy savings are thus achieved as lower applied pressures (and hence less pumping work) are needed to achieve the target water permeate rates. Pumping work is therefore partially displaced by thermal

energy. A thermally enhanced RO system is illustrated in Figure 2.2. As shown, thermal energy can be efficiently managed by recovering it from the brine and permeate volumes and then recycling it back to the incoming feed via heat exchangers.

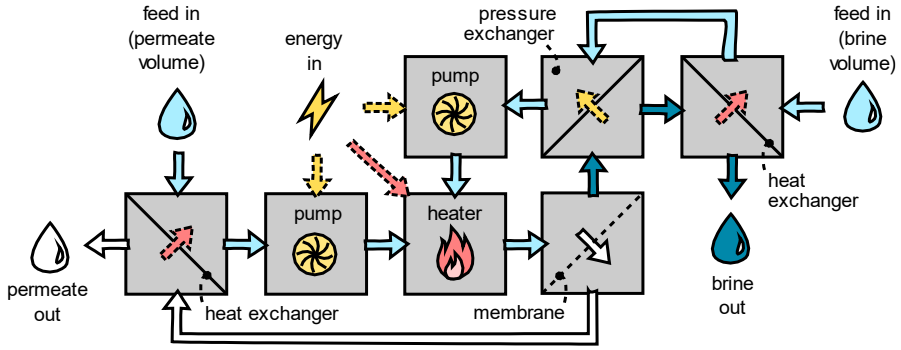

Figure 2.2 Schematic of a thermally enhanced RO plant designed to use heat to reduce the required mechanical pump work. Other configurations are also possible so that incoming feed can either be heated first or pressurized first.

The overall energy balance of thermally enhanced RO is therefore the sum of the reduced mechanical pumping work and the added thermal energy. This is expressed in equation (2.9) which shows the overall specific energy balance of thermally enhanced RO $\dot{w}_{TE-RO}$ as a function of the coefficient of performance *cop*, used to relate the specific thermal energy input q to the mechanical work of RO $\dot{w}_{RO}$. The specific thermal energy input $\dot{q}$ is defined in equation (2.10) as a function of the temperature to which feed is heated ΔT and the efficiency with which heat is recycled η_{Tex}. A detailed derivation of this energy balance is provided in Supplementary Note 2.4.

$$\dot{w}_{\mathrm{TE-RO}} = \dot{w}_{\mathrm{RO}} + \frac{\dot{\mathrm{q}}}{\mathrm{cop}} \qquad 2.9$$

$$\dot{\mathrm{q}} = \frac{\dot{\mathrm{Q}}}{\dot{\mathrm{V}}_{\mathrm{P}}} = \frac{1}{\mathrm{r}}\,\rho\,\mathrm{c_p}\,\Delta\mathrm{T}(1-\eta_{\mathrm{hex}}) \qquad 2.10$$

Where ρ and c_p are the density and specific heat input of the feed. Note that the coefficient of performance for an ideal Carnot heat pump operating at its thermodynamic

limit, $cop = T / \Delta T$. Also note that in the ideal case, where ambient heat loss is eliminated considering heat is completely recycled $\eta_{hex} \rightarrow 1$, the thermal energy input is reduced to zero $\dot{q} \rightarrow 0$.

The energy balance of thermally-enhanced RO is affected by several competing dynamics as illustrated in Figure 2.3, including (a) the apparent increase in membrane water permeability caused by changes in the fluid viscosity, (b) the decrease in concentration polarization caused by higher salt diffusivity, (c) the increase in osmotic pressure, and (d) the apparent increase in membrane salt permeability caused by higher salt diffusivity.

The energy savings from a thermally enhanced RO system are achieved primarily from an increase in the apparent water permeability of the membrane that is observed in the presence of warm feed. This dynamic has been studied extensively throughout the literature, and it is generally agreed that much of the observed increase is the result of reduced fluid viscosity, rather than because of any significant change in the membrane structure [43], [54], [55]. Equations (2.11) and (2.12) approximate the relationship between membrane water permeability A, feed viscosity μ, and feed temperature T [56], [57], [58]. The relationship is also illustrated in Figure 2.3 (a) which shows a near doubling of the membrane's apparent water permeability as feed is heated from 20 to 50 °C. Supplementary Note 2.5 provides additional supporting information about equation (2.11).

$$\mathrm{A} = \mathrm{A}_{20\,^{\circ}\mathrm{C}}\,\frac{\mu_{20\,^{\circ}\mathrm{C}}}{\mu} \tag{2.11}$$

$$\mu = 0.4599\,\exp(1.796 \times 10^{3}\,\mathrm{c} - 0.021\,\mathrm{T}) \tag{2.12}$$

To a lesser extent, thermally enhanced RO also benefits from reduced concentration polarization. As shown in equations (2.13) and (2.14), the salt mass transfer coefficient *k* is directly proportional to the salt diffusivity *D*, which increases with temperature *T* [59], [60], [61].

$$\mathrm{k} = \mathrm{D}\,\frac{\mathrm{Sh}}{\mathrm{d}} \tag{2.13}$$

$$\mathrm{D} = 6.725 \times 10^{-6} \exp\left(9.034 \times 10^{-3}\,\mathrm{c} - \frac{2513}{\mathrm{T}}\right) \tag{2.14}$$

$$\mathrm{Sh} = 0.46\,\mathrm{Re}^{0.36}\,\mathrm{Sc}^{0.36} \tag{2.15}$$

Where *Sh* is Sherwood number and *d* is the hydraulic diameter. Various empirical equations have been proposed to described the Sherwood number in different RO membrane configurations, but it is generally described as a function of the Reynolds number *Re* and the Schmidt number *Sc* [62], [63], [64].

Figure 2.3 (b) shows that k increases by almost 70 % from 20 to 50 °C. This helps to reduce the concentration difference across the membrane because the polarization factor is proportional to the exponent of k^{-1}, as described previously in equation (2.6). This enables energy savings as target permeate flux can be achieved with lower applied pressures. It also reduces the driving force for undesirable salt leakage, which may assist in producing a lower concentration permeate water product, although other dynamics mitigate this benefit, as explained below.

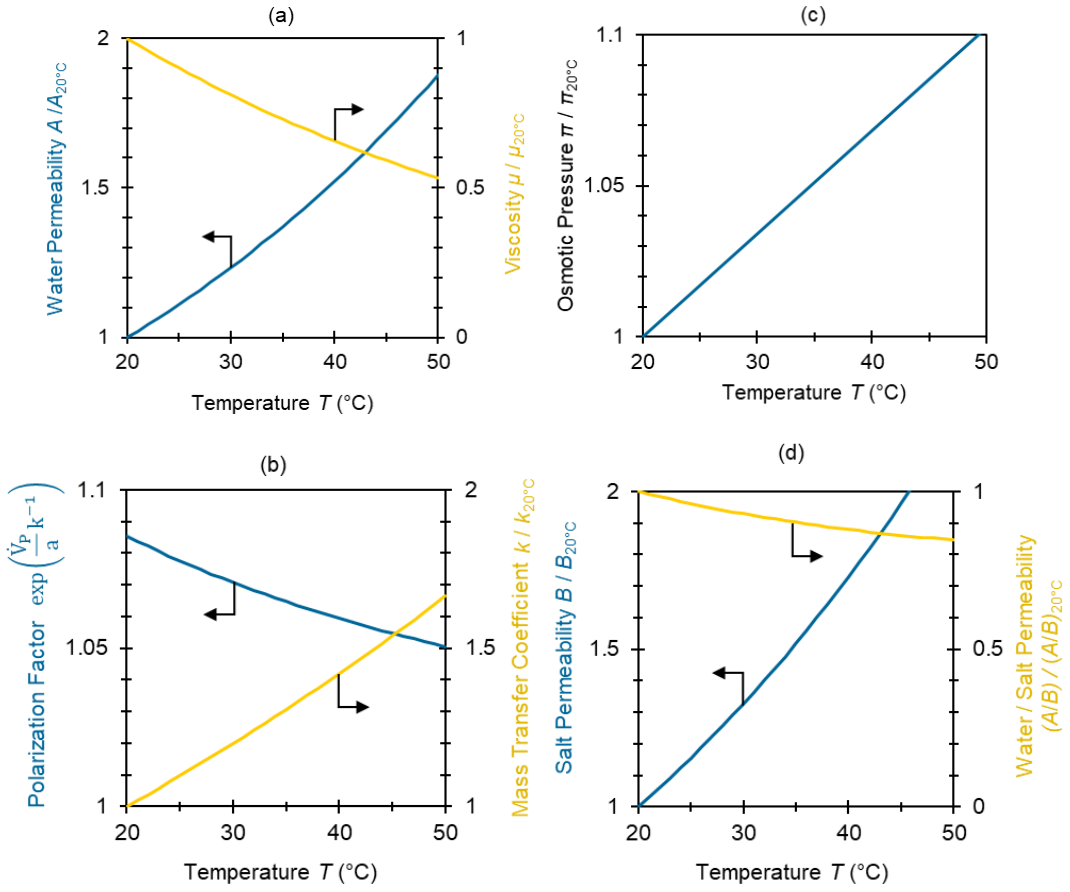

Figure 2.3 (a) Membrane water permeability is inversely proportional to viscosity, as described in equations (2.11) and (2.12). (b) Concentration polarization factor $\exp\left(\frac{\dot{V}_P}{a}k^{-1}\right)$ and mass transfer coefficient as a function of temperature, as described in equation (2.13). (c) Osmotic pressure of feed as a function of temperature calculated using equation (2.5). (d) Membrane salt permeability as a function of temperature can be predicted from the proportional change in salt diffusivity, as described in equation (2.16).

The benefits of thermally enhanced RO are mitigated by (i) an increase in the osmotic pressure difference as a function of feed temperature, and (ii) an increase in the salt permeability of the membrane. As described previously in equation (2.5), osmotic pressure is proportional to the absolute temperature of the feed. For example, Figure 2.3 (c) shows a 10 % increase in osmotic pressure as feed is heated from 20 to 50 °C. This increases the pumping pressure, and hence mechanical work, that must be applied in order to achieve the target water permeate rates, and therefore mitigates the energy

savings of thermally enhanced RO. Interestingly, there is some temperature that optimizes this tradeoff and yields the minimum specific energy of RO.

The second drawback of thermally enhanced RO is the increase in membrane salt permeability that is associated with heat. This dynamic is well studied in the literature, and it is generally agreed that much of the perceived increase in salt permeability is due to the increase in salt diffusivity rather than any change in the membrane structure itself [55], [65], [66]. For this reason, the change in the apparent membrane salt permeability B can be approximated by the proportional change in salt diffusivity D, as expressed in equations (2.14) and (2.16). As illustrated in Figure 2.3 (d) salt diffusivity and hence salt permeability more than double as feed is heated from 20 to 50 °C. Because this increase in salt permeability is greater than the increase in water permeability reported previously in Figure 2.3 (a), the ratio of water to salt permeability A/B drops by almost 20 % from 20 to 50 °C. This increase in B and this drop in A/B are certainly not desirable, but their significance can only be properly evaluated by considering their net effect on specific energy consumption and levelized cost of water. For example, it is very possible that a small change in A can be more significant than a large change in B. Supplementary Note 2.5 provides additional supporting information about equation (2.16).

$$\mathrm{B} = \mathrm{B}_{20\,^{\circ}\mathrm{C}}\ \frac{\mathrm{D}}{\mathrm{D}_{20\,^{\circ}\mathrm{C}}} \tag{2.16}$$

2.3 Methods

To evaluate the performance of thermally enhanced RO an analytical model was developed in Excel 2019 software (Microsoft, Redmond WA) to solve the system of

equations described in Section 2.3. This includes a simple numerical guess and check algorithm used to solve equations (2.6)-(2.8) to within < 0.01 % convergence error.

Performance was evaluated in terms of the specific work of RO $\dot{w}_{RO}$ and the overall specific energy balance of thermally enhanced RO $\dot{w}_{TE-RO}$ (given a certain heat pump coefficient of performance cop) as a function of operating temperature. For most commercial membranes, maximum recommended operating temperatures typically range from 35-40 °C, but recent publications have shown promising materials advances for high temperature operation well above typical values [67]. Therefore, a temperature range of 20 to 50 °C is considered here to provide a view of performance across both current and possible future operating conditions.

In general, the minimum specific energy was identified as a function of operating temperature, while respecting targets for recovery ratio r and permeate flux $\dot{V}_P$ / a, and limits for permeate concentration cP and applied pressure Δp. Performance was evaluated across a range of conditions including for a variety of common feed sources (brackish water, seawater, and oil and gas produced water, each approximated with NaCl concentrations of cF = 10, 35, and 70 g/l respectively) and for a variety of membrane water permeabilities and salt selectivities (A = 0.5, 1, and 2 lmh/bar, and A/B = 5, 10, and 20 bar^{-1}). Table 2.1 defines the default modelling input conditions. Efficiency of mechanical equipment were assumed to be constant, although empirical expressions for efficiency as a function of temperature are available in the literature and can be included for more detailed analysis [68].

Table 2.1. Default case study conditions unless otherwise specified.

Operating Targets	
Permeate flux $\dot{V}_P$ / a	25 lmh
Recovery ratio r	0.5
Operating Limits	
Applied pressure Δp	< 100 bar
Permeate concentration c_P	< 0.5 g/l
Feed Properties	
Solute	NaCl
Concentration c_F	35 g/l
Temperature T	20 °C
Velocity	0.1 m/s
Viscosity μ [69]	$0.4599 \exp(1.796\mathrm{c}\left(\frac{mol}{m^3}\right) - 0.021\mathrm{T}(K))(Pa.s)$
Density ρ [41], [70]	$1005 + 7.062 \times 10^5\mathrm{c}\left(\frac{g}{cm^3}\right) - 0.3148 (\mathrm{T}(K) - 273.15) - 824.3 (\mathrm{T} - 273.15) \mathrm{c} - 3.783 \times 10^8\ \mathrm{c}^2 \left(\frac{kg}{m^3}\right)$
Salt diffusivity D [71]	$6.725 \times 10^{-6} \exp(1.546 \times 10^{-4} \mathrm{c}\left(\frac{mol}{m^3}\right) \mathrm{M}\left(\left(\frac{g}{mol}\right)\right) - 2513 / T(K)) \left(\frac{m^2}{s}\right)$
Membrane Properties	
Water permeability A	1 lmh/bar
Salt permeability B	0.1 lmh
Hydraulic diameter d	0.001 m
Equipment Efficiency	
Pump η_{pump}	0.8
Pressure exchanger η_{pex}	0.9
Heat exchanger η_{hex}	0.9
Coefficient of performance *cop*	$T(K) / \Delta T$

2.4 Results

2.4.1 Energy Use of Reverse Osmosis for Seawater Desalination

Figure 2.4 shows the specific pump work of RO $\dot{w}_{RO}$ for a common application of seawater desalination operated at ambient baseline temperature of T_o = 20 °C (input parameters and assumptions are provided in Table 2.1). As shown, specific pump work can be minimized by balancing the recovery ratio. When the recovery ratio is too high, the feed water becomes very concentrated and as a result a very large, applied pressure

(i.e. more energy) is required to maintain the target permeate rate. On the other hand, when the recovery ratio is too low, large volumes of brine need to be handled, and therefore any inefficiencies in the pressure exchanger are exacerbated and quickly lead to high energy use. When these competing dynamics are balanced, the minimum specific pump work is obtained. For the scenarios shown, this is achieved at recovery between r = 0.3–0.5.

Energy efficiency is also shown to improve at low permeate flux because this allows for low applied pressures to be used. For example, the minimum specific pump work in Figure 2.4, $\dot{w}_{RO}$ = 2.0 kWh/m^3 is achieved when the process is operated at low permeate rates of $\dot{V}_P / a = 10\ lmh$. Operation at even lower permeate flux would allow for even lower specific pump work, and the thermodynamic limit of seawater desalination of 0.8 kWh/m^3 is achieved as permeate flux approaches zero, $\dot{V}_P / a \rightarrow 0$. On the other hand, operating at such low permeate flux requires oversizing the desalination plant, which is costly. There is a practical and economic requirement to maintain reasonably high flux in order for RO to be cost effective. Or in other words, lower specific pump work associated with lower flux can only be justified if these energy cost savings are greater than the cost of building a larger plant. This illustrates that optimizing the specific energy of RO must be done while also respecting other performance targets and operating limits, including costs as well as the permeate quality and the membrane integrity, as explained next.

Figure 2.4 also shows the concentration of the permeate c_P that is produced from the RO desalination process. This permeate concentration is important because it is a measure of the quality of the produced water permeate. As shown, operating at low

recovery ratios and with high permeate flux will tend to produce lower concentration water permeate.

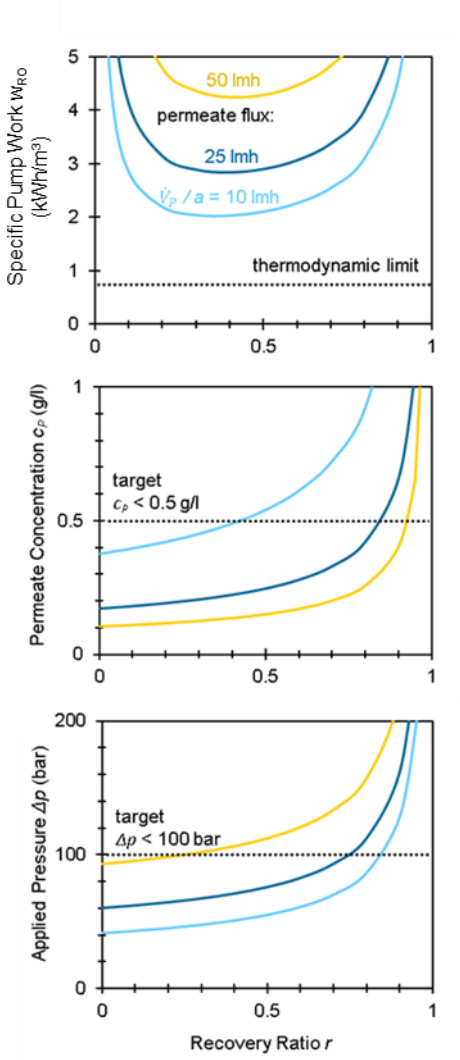

Figure 2.4 Specific pump work $\dot{w}_{RO}$, concentration of permeate c_P, and applied pressure Δp for reverse osmosis desalination of seawater given a range of recovery ratios r and a range of normalized permeate rates $\dot{V}_P / a$. Default input parameters and assumptions are provided in Table 2.1.

This is because (i) low recovery ratios minimize the accumulation of salts in the feed and hence lower the concentration driving force for salt diffusion, and (ii) higher permeate flux dilutes the permeating salts, lowering the permeate concentration. A water quality target of c_P < 0.5 g/l is provided for reference [72], [73].

Figure 2.4 also shows the applied pressure Δp that drives RO and that is necessary to achieve the targets for recovery ratio and permeate flux. The applied pressure scales with both of these targets and may exceed the mechanical limits of the membrane unless care is taken to avoid such failure. For example, if high permeate flux $\dot{V}_P / a = 50$ lmh is desired, then recovery must be limited to $r < 0.25$ so as to avoid exceeding the membrane burst pressure. A RO membrane burst pressure of 100 bar is shown here for reference [74].

2.4.2 Advantages of Using Heat to Thermally Enhance Reverse Osmosis

To illustrate the advantages of using heat to thermally enhance RO, consider again the application to seawater desalination. Figure 2.5 shows the specific pump work of RO $\dot{w}_{RO}$ as feed temperature is increased above the ambient baseline of 20 °C (other input parameters and assumptions are provided in Table 2.1). As shown, specific pump work reduces as feed is heated. The improvement is especially marked in cases where either high water permeate flux or a high recovery ratio is targeted, or both. For example, for the case where flux is maintained at $\dot{V}_P / a = 50$ lmh with a recovery ratio $r = 0.5$, specific pump work is reduced by 24 % as feed is heated to $T = 50$ °C. Such improvements are consistent with what has been reported elsewhere in the literature [38], [58], [74], [75]. On the other hand, an increase in permeate concentration is also observed. For the same example, the permeate concentration almost doubles from $c_P =$ 0.15 to 0.28 g/l, although importantly it still remains below the water quality limit of 0.5 g/l.

These energy savings are the result of thermally enhanced transport dynamics previously described in Section 2.3 (i.e. higher apparent membrane permeability and

reduced polarization), which allow for target flux and recovery ratios to be achieved with lower applied pressures. Operating at lower applied pressure not only reduces pump energy use, it also reduces the mechanical force applied to the membrane and thereby reduces the risks of membrane failure. For example, for the same case where flux is maintained at $\dot{V}_P / a$ = 50 lmh with recovery ratio r = 0.5, the applied pressure at T = 20 °C initially exceeds the specified membrane burst pressure of 100 bar. But as the feed is heated to T = 50 °C the applied pressure is reduced to a much lower and acceptable pressure of Δp = 86 bar. This suggests that thermally enhanced RO can provide an energy efficient means of achieving high water permeate flux and high recovery ratios while mitigating the risks of membrane failure. Other advantages of operating at lower applied pressures have also been reported in the literature, including less fouling and crystallization at the membrane surface [76], [77].

Analysis of the energy balance is incomplete however without consideration for the thermal energy input during thermally enhanced RO. This depends largely on the efficiency of the thermal energy system, including the heat source's coefficient of performance and the heat recovery efficiency. Both of these variables are explored further in Section 4.5.3, but here the energy balance is shown assuming an ideal Carnot heat pump operating at its thermodynamic limit $cop_{max} = T / \Delta T$ and assuming heat exchanger efficiency of η_{Tex} = 0.9. As shown, the energy balance remains favorable even with consideration for the thermal energy input. Again, the most significant energy savings are observed when high flux and high recovery ratios are targeted. Referring to the same example as previously, where flux is maintained at $\dot{V}_P / a$ = 50 lmh and recovery ratio r = 0.5, the overall specific energy balance of thermally-enhanced RO is

reduced from $\dot{w}_{TE-RO}$ = 4.3 kWh/m^3 at ambient temperatures of T = 20 °C down to a minimum of $\dot{w}_{TE-RO}$ = 3.8 kWh/m^3 at T = 41 °C , for a reduction of almost 12 %.

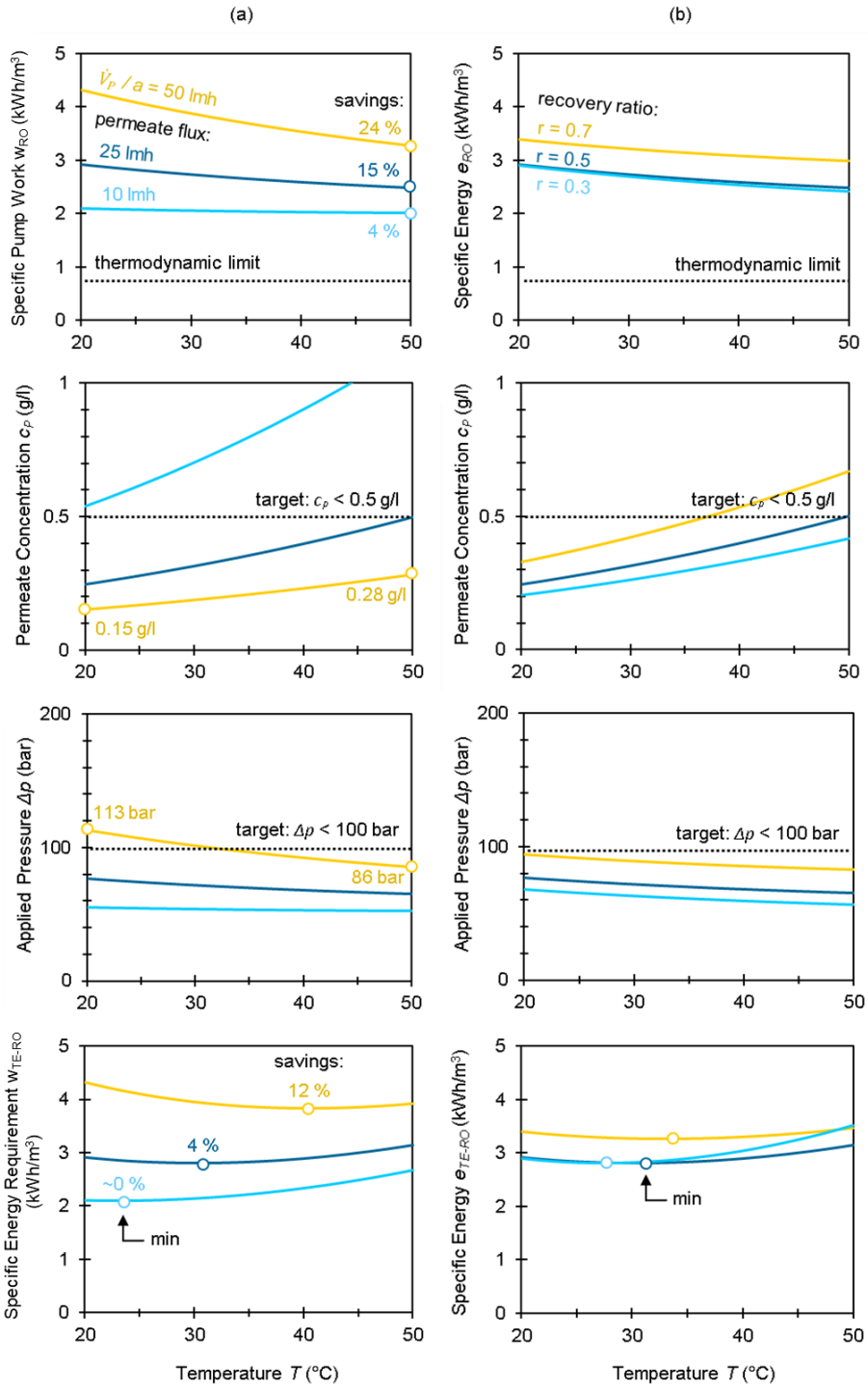

Figure 2.5 Specific pump work of RO $\dot{w}_{RO}$, concentration of permeate c_P, applied pressure Δp, and overall specific energy requirement of thermally enhanced RO $\dot{w}_{TE-RO}$

for desalination of seawater at (a) several different rates of water permeate flux $\dot{V}_P / a$ and (b) several different recovery ratios *r*. Default input parameters and assumptions are provided in Table 2.1.

2.4.3 Importance of High Thermal Efficiency and of an Abundant Source of Heat

The overall energy balance of thermally enhanced RO depends largely on the efficiency with which heat can be delivered to and recycled within the system. Figure 2.6 shows the specific work of thermally enhanced RO $\dot{w}_{TE-RO}$ in response to a range of different heat source coefficients of performance cop and different heat exchanger efficiencies η_{Tex}. As shown, the overall energy balance can be favorable and produce savings if thermal efficiency is high. For example, with an ideal heat pump operating at its thermodynamic limit $cop_{max} = T / \Delta T$ and assuming heat exchanger efficiency of $\eta_{Tex} = 0.9$, the given scenario shows a minimum specific work of $\dot{w}_{TE-RO} = 2.8$ kWh/m^3 at T = 31 °C, equal to energy savings of 4 % relative to baseline temperature. On the other hand, when less optimistic thermal efficiencies are considered, the energy balance becomes unfavorable. For example, given cop = 1 or even 5, heating the feed increases the overall energy use. Similarly, a reduction in the heat exchanger efficiency also shows less favorable results. This suggests that for thermally enhanced RO to yield energy savings, very efficient thermal energy systems are required. Note that a perfect heat exchanger essentially eliminates the need for thermal energy input as heat is recycled from the brine and permeate volumes and returned to the incoming feed.

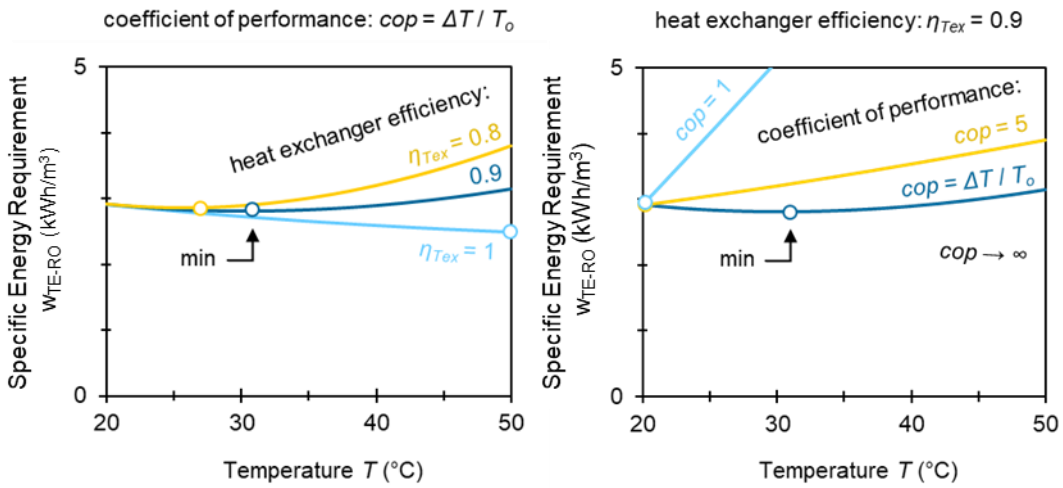

Figure 2.6 Specific energy requirement of thermally enhanced RO $\dot{w}_{TE-RO}$ for desalination of seawater at a range of different feed temperatures T and for several different coefficients of performance *cop* and several different heat exchanger efficiencies η_{Tex}. Default input parameters and assumptions are provided in Table 2.1

In analyzing the overall energy balance of thermally enhanced RO, it is important to also consider that two different forms of energy are included: (i) mechanical work for pumping, and (ii) thermal energy for heating feed. The coefficient of performance previously introduced in equation (2.9) and analyzed above implies that mechanical work would be used to generate heat, but there are of course many alternatives such as solar thermal energy or waste heat from a power plant. In such cases, it is more appropriate to consider the energy balance of work and heat separately, as they each have their own distinct value [78]. Figure 2.7 shows the specific energy balance of work and heat for the default scenario from Table 2.1. As shown, the thermal energy input clearly exceeds the savings in mechanical pumping work (by a factor of between 11-16), and yet such a tradeoff may be acceptable in certain applications. For example, if waste heat is abundant and free, the investment of the necessary heat exchangers could be justified by the electricity savings associated with less mechanical pumping work. Such

a determination would require further techno-economic analysis in future work, but it does suggest another avenue forward for the proposed concept.

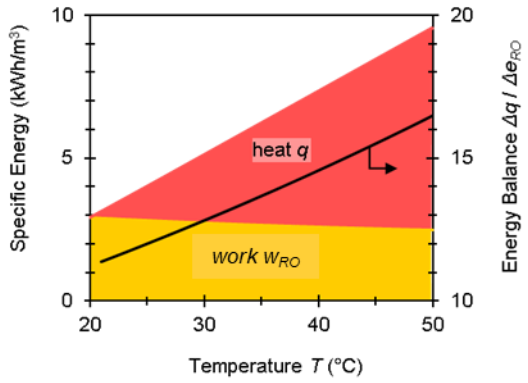

Figure 2.7 Energy balance of thermally-enhanced RO in terms of mechanical pumping work $\dot{w}_{RO}$ and thermal energy input $\dot{q}$ for desalination of seawater at a range of different feed temperatures T. The right-axis shows the ratio between thermal energy input and savings in mechanical work $\dot{q}$ / $\dot{w}_{RO}$ relative to baseline temperature. Default input parameters and assumptions are provided in Table 2.1.

2.4.4 Suitability of Thermally Enhanced RO for a Variety of Feed Sources

Figure 2.8 shows the performance of thermally enhanced RO when applied to different feed water sources. Several scenarios are considered including desalination of (i) seawater with concentration c_F = 35 g/l, (ii) brackish water with c_F = 10 g/l, and (iii) produced wastewater from oil and gas production with c_F = 70 g/l. In each case, the targets for water permeate flux and recovery ratio are adjusted so as to be consistent with conditions typical for treatment of these different sources. For (i) seawater, the water permeate flux and recovery ratio are set to the default targets, $\dot{V}_P$ / a = 25 lmh and r = 0.5. For (ii) brackish water, the targets are set to $\dot{V}_P$ / a = 50 lmh and r = 0.75. And for (iii) produced wastewater, the targets are set to $\dot{V}_P$ / a = 10 lmh and r = 0.25.

As the results show, the advantages of thermally-enhanced RO are much more pronounced in applications with high water flux and recovery targets, which are typically

associated with low concentration feed sources. For example, in the case of brackish water desalination, energy savings from reduced mechanical pumping reach up to 33 % when feed is heated to T_F = 50 °C. And even when thermal energy input is considered, the overall specific energy savings from thermally-enhanced RO reach up to 18 % when feed is heated from T_F = 20 to 46 °C. This is much more than the 4 % savings observed for the base case of seawater desalination. For produced water, the energy savings are negligible, mostly due to the fact that a low water permeate flux of only $\dot{V}_P / a$ = 10 lmh is targeted, which tends to mitigate the benefits of heating feed. The low flux and recovery targets for produced wastewater are selected so as to moderate the very high applied pressures that are associated with RO of such a high concentration feed source. For this reason, several publications have suggested alternative RO cycles or membrane distillation for such feed [79], [80].

Figure 2.8 also shows the significance of the ambient water temperature of the feed source. As shown, heating the feed from a baseline temperature of either T_o = 10, 20, or 30 °C can be advantageous as it reduces energy use and applied pressure. Similar plots are shown for the specific work $\dot{w}_{RO}$, permeate concentration c_P, and applied pressure Δp which confirms that transport dynamics are a function of feed temperature but not the baseline reference temperature. But the overall energy balance of the three cases does show some difference, because thermal efficiency of the theoretical Carnot heat pump is slightly higher if the reference temperature is lower. This confirms that higher thermal energy inputs can be justified when the feed has a cooler ambient reference temperature.

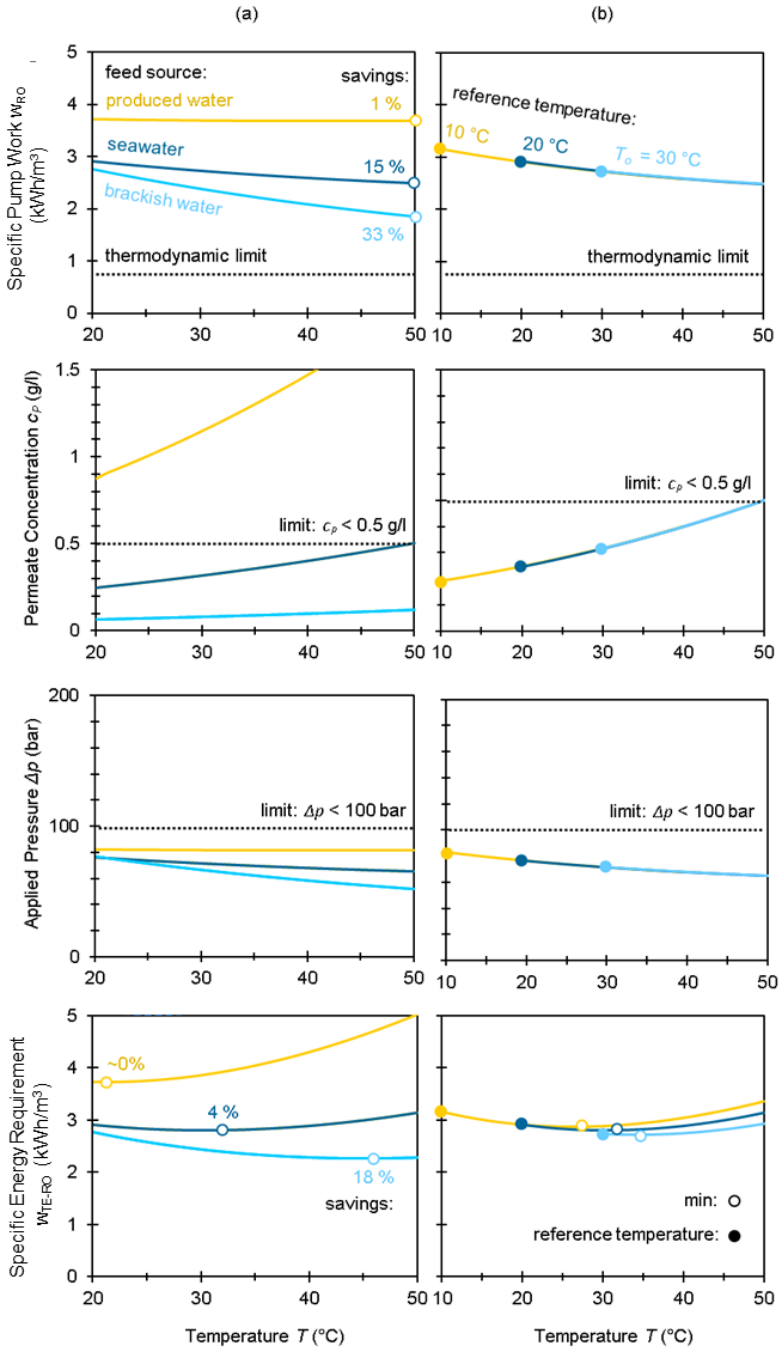

Figure 2.8 Specific pump work of RO $\dot{w}_{RO}$, concentration of permeate cP, applied pressure Δp, and specific energy requirement of thermally-enhanced RO $\dot{w}_{TE-RO}$ for (a) desalination of several different feed sources, and for (b) desalination of seawater at a several different ambient temperatures To. Feed sources include seawater, brackish water, and produced wastewater with concentrations of cF = 35, 10, and 70 g/l respectively, water flux targets of $\dot{V}$P / a = 25, 50, and 10 lmh, and water recovery targets of r = 0.5, 0.75, and 0.25, respectively. Other input parameters and assumptions are provided in Table 2.1.

2.4.5 Suitability of Thermally-Enhanced RO to a Variety of Membranes

Figure 2.9 shows the significance of thermally-enhanced RO on the performance of different membranes with a variety of water and salt permeabilities A and B. Three membranes are defined to provide a sample of common membrane parameters across the permeability / selectivity limits established for RO membranes (similar to the Robeson limits for gas membranes) [50–52]. The defined membranes include (i) a low permeability / high selectivity membrane with A = 0.5 lmh/bar and A/B = 20 bar^{-1}, (ii) a high permeability / low selectivity membrane with A = 2 lmh/bar and A/B = 5bar^{-1}, and (iii) the default membrane with A = 1 lmh/bar and A/B = 10 bar^{-1}. While heat is beneficial in all three membranes, the energy savings $\dot{w}_{TE-RO}$ and reductions in applied pressure Δp are most significant with the low permeability membrane. For example, in the defined low permeability membrane, overall specific energy savings of thermally-enhanced RO reach 9 % when the feed is heated to 39 °C. This is to be expected since higher applied pressures are needed to achieve the target flux with low permeability membranes, and hence additional energy savings can be obtained. This is also consistent with the previous observation that thermally-enhanced RO is most beneficial in high flux applications, since here a particular target flux would be relatively greater for a low permeability membrane. Interestingly, the drawback of higher permeate salt concentration cP is also largely mitigated with the low permeability / high selectivity membrane. This suggests that thermally-enhanced RO may be particularly suited for systems involving low permeability / high selectivity membranes.

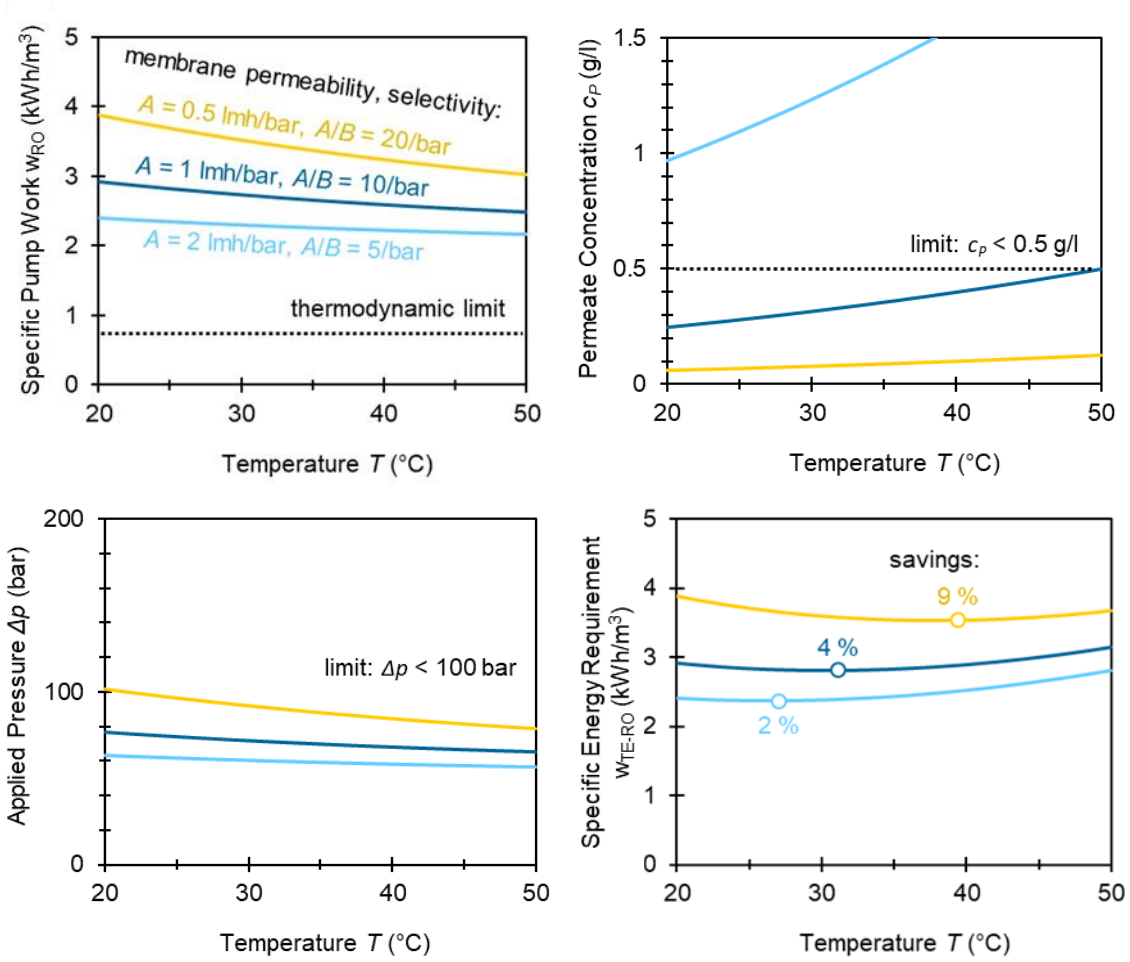

Figure 2.9 Specific pump work of RO $\dot{w}_{RO}$, concentration of permeate cP, applied pressure Δp, and specific energy requirement of thermally-enhanced RO $\dot{w}_{TE-RO}$ for desalination of seawater with several different membranes, including different water permeabilities A and different water/salt selectivity A/B. Default input parameters and assumptions are provided in Table 2.1

2.5 Conclusions

In this study the potential for using low-grade heat to thermally-enhance RO desalination was evaluated. In general, adding thermal energy to increase the temperature of the RO feed was shown to significantly improve water permeate flux leading to important savings in mechanical work. Reductions in specific energy of up to 24 % were observed for high flux seawater desalination and up to 33 % for brackish water, when the feed temperature was increased from 20 to 50 °C. Such improvements are consistent with

what has been reported elsewhere in the literature [58], [81], [82], however until now the thermal energy input required to heat feed has been mostly unaccounted for.

For the first time, an overall energy balance of thermally-enhanced RO was considered to evaluate the tradeoff between savings in mechanical pump work and input of thermal energy. Results suggest that this tradeoff is favorable only under very optimistic conditions. In particular, there is a need for both a very high heat pump coefficient of performance (if work is used to supply heat), and very high heat exchanger efficiency for recycling thermal energy within the system. Under these conditions, overall energy savings of up to 12 % were observed for seawater desalination when feed temperature was increased from 20 to 41 °C, and up to 18 % for brackish water desalination with feed heated to 46 °C.

Other key variables were also identified. The energy balance was found to be particularly favorable in applications where high water flux is desired, such as in desalination of brackish water, and in applications where membrane water permeability is low and represents a limiting factor. Thermally enhanced RO is also recommended for applications where high feed concentrations typically require elevated applied pressures. In such cases, thermally enhanced RO can provide a means of reducing the mechanical force applied to the membrane and thereby reduce the risks of membrane failure. On the other hand, additional consideration should be given to the thermal stability of membranes when exposed to high temperatures for sustained periods of time.

Encouragingly, recent publications suggest that advanced membranes show stable operation at elevated temperatures [83].

Other important drawbacks should also be considered in future work. A significant increase in salt leakage was observed throughout the analysis, resulting in increased permeate concentrations. For example, for the case of seawater desalination where 12 % overall energy savings were reported, permeate concentration increased from 0.15 to 0.23 g/l when feed temperature was increased from 20 to 41 °C. Similar increases were observed across the various scenarios considered. Although this particular case remained below our target of 0.5 g/l, other scenarios may be more significant and for certain applications tolerances may be lesser, possibly necessitating an additional RO pass of the permeate. For example, of particular concern is leakage of boron, for which permeate concentrations of less than 0.5 mg/l are often targeted [84]. Boron leakage is likely to be exacerbated at high temperatures, although recent studies have managed to achieve promising boron selectivity even at high temperatures [83]. Also, of concern is the precipitation of calcium nitrate and other scaling agents that are typically exacerbated at high temperatures [85]. Chemical and mechanical cleaning can mitigate such scaling, but at a cost.

To further clarify the potential of thermally enhanced RO we suggest that future work consider the techno-economic balance between the cost savings of reduced mechanical pumping work and the cost of adding thermal energy, including additional operating and capital costs. In such an analysis, the levelized cost of water can be optimized based on the cost of electricity and the cost of thermal energy. There are several abundant sources of low-grade heat such as solar radiation and power plant waste heat that can be considered, thereby avoiding the need for using electricity or fuel to generate heat, but even in such cases the capital cost of the heat recovery systems would need to be

justified. Therefore, while this study suggests that the concept of thermally enhanced RO has thermodynamic merit, with a favorable energy balance under the right conditions, it remains to be seen whether an economic and practical case can be made for the concept. If future work confirms this, then thermally enhanced RO may represent a means of improving the sustainability of water infrastructure and increasing global access to freshwater.

2.6 Supplementary Note

2.6.1 Supplementary Note 2.1: RO Work Used by Pumps

The energy consumption of RO is related to the pumping power that is required to pressurize feed solution above its osmotic pressure potential. As described in equation S2.1, the pumping load can be distributed between two pumps, with one to handle a portion of the feed equal to the permeate volume, and another to handle a portion equal to the brine volume. This configuration facilitates the integration of a pressure exchanger capable of recovering mechanical energy from the pressurized brine solution and recycling it back to the incoming feed. A simple derivation of the energy requirements of both of these pumps is provided below.

$$\dot{w}_{RO} = \frac{\dot{W}_{RO}}{\dot{V}_P} = \dot{w}_P + \dot{w}_B \qquad \text{S2.1}$$

The work use of the first pump $\dot{W}_P$ is simply the product of the applied pressure Δp, the volume through it (which is equal to the permeate volume $\dot{V}_P$), and the inverse of the pump efficiency η_{pump}. When normalized per unit volume of permeate, it can be expressed as the specific pump work w_P.

$$\dot{W}_P = \frac{1}{\eta_{pump}} \dot{V}_P \, \Delta p \qquad \text{S2.2a}$$

$$\dot{w}_P = \frac{\dot{W}_P}{\dot{V}_P} = \frac{1}{\eta_{pump}} \Delta p \qquad \text{S2.2}$$

The energy use of the second pump $\dot{W}_B$ is the product of the volume through it (which is equal to the brine volume $\dot{V}_B$), the pressure that is needed to make up for losses in the pressure exchanger, and the inverse of the pump efficiency. Note that in an ideal system, with a perfect pressure exchanger $\eta_{pex} \rightarrow 1$, the load on this brine pump would be reduced to zero $\dot{W}_B \rightarrow 0$. When normalized per unit volume of permeate, it can be expressed as the specific pump work $\dot{w}_B$.

$$\dot{W}_B = \frac{1}{\eta_{pump}} \dot{V}_B \Delta p \left(1 - \eta_{p\,ex}\right) \qquad \text{S2.3a}$$

$$\dot{W}_B = \frac{1}{\eta_{pump}} \dot{V}_P \left(\frac{1}{r} - 1\right) \Delta p \left(1 - \eta_{p\,ex}\right) \qquad \text{S2.3b}$$

$$\dot{w}_B = \frac{\dot{W}_B}{\dot{V}_P} = \frac{1}{\eta_{pump}} \left(\frac{1}{r} - 1\right) \Delta p \left(1 - \eta_{p\,ex}\right) \qquad \text{S2.3}$$

Where *r* is the recovery ratio. Pressure losses due to friction in the system are neglected.

2.6.2 Supplementary Note 2.2: Applied Pressure

Applied pressure is an operating parameter that can be controlled to achieve target rates of water permeate recovery. The relationship between applied pressure Δp and water permeate rate $\dot{V}_P$ is described by the solution-diffusion model [86], [87], [88].

$$\dot{V}_P = a \, A \, (\Delta p - \Delta \pi) \qquad \text{S2.4a}$$

$$\Delta p = \frac{\dot{V}_P}{a} A^{-1} + \Delta\pi \quad \text{S2.4}$$

Where *a* is the membrane surface area, *A* is the membrane water permeability, and $\Delta\pi$ is the osmotic pressure difference across the membrane.

2.6.3 Supplementary Note 2.3: Permeate and Brine Concentrations

Concentration will vary along the length of the membrane as water permeate is recovered from the feed and as salt leaks through the imperfect membrane. To account for this variation and its important effect on osmotic pressure, the concentration difference is defined in equation (2.5) as a function of the logarithmic mean between the inlet c_F and the outlet c_B. Alternatively, the feed side concentration could be simplified with just the arithmetic mean as in equation (S2.5a).

$$\Delta c = \exp\left(\frac{\dot{V}_P}{a} k^{-1}\right)\left(\frac{c_B - c_F}{\ln c_B - \ln c_F}\right) - c_P \quad \text{S2.5}$$

$$\Delta c = \exp\left(\frac{\dot{V}_P}{a} k^{-1}\right)\left(\frac{c_B + c_F}{2}\right) - c_P \quad \text{S2.5a}$$

The concentration of the brine c_B can be defined by taking a simple mass balance of the salt that is present in the feed, permeate, and brine, respectively $\dot{m}_F$, $\dot{m}_P$, and $\dot{m}_B$. This is shown in equation (2.6). Note that for low recovery ratios $r \rightarrow 0$, the concentration of the outlet brine approaches that of the inlet feed, $c_B \rightarrow c_F$.

$$\dot{m}_F = \dot{m}_P + \dot{m}_B \quad \text{S2.6a}$$

$$\dot{V}_F c_F = \dot{V}_P c_P + \dot{V}_B c_B \quad \text{S2.6b}$$

$$c_F = \frac{\dot{V}_p}{\dot{V}_F} c_P + \frac{\dot{V}_B}{\dot{V}_F} c_B \quad \text{S2.6c}$$

$$c_F = r\, c_P + (1 - r)\, c_B \quad \text{S2.6d}$$

$$c_B = \frac{c_F - r\, c_P}{1 - r} \qquad \text{S2.6}$$

The concentration of the permeate c_P, can be defined by considering the mechanism by which salt is transported across the membrane. Equation (S2.7a) defines the mass permeate rate of salt $\dot{m}_P$ as a function of diffusion driven by the concentration difference across the membrane Δc, where B is the membrane's salt permeability. This can be reorganized to obtain an expression for permeate concentration c_P as provided in equation (2.7). Note that for an ideal membrane that is impermeable to salt $B \rightarrow 0$, the concentration of the permeate is negligible $c_P \rightarrow 0$.

$$\dot{m}_P = a\, B\, \Delta c \qquad \text{S2.7a}$$

$$\dot{V}_P\, c_P = a\, B\, \Delta c \qquad \text{S2.7b}$$

$$c_P = \frac{a}{\dot{V}_P}\, B\, \Delta c \qquad \text{S2.7}$$

Together, equations (S2.5)-(S2.7) describe the salt mass balance between feed, brine, and permeate. To solve for the resulting concentration difference Δc, the system of equations presented here requires a numerical approach to solve, such as an iterative guess and check method. Alternatively, it may be of interest in certain cases to approximate the feed concentration with a simple arithmetic mean, as shown previously in equation (S2.5a). This makes it possible to obtain an analytical solution for Δc, as shown below, but it also introduces additional error to the analysis, which is why it is not employed here.

$$\Delta c = \exp\left(\frac{\dot{V}_P}{a} k^{-1}\right)\left(\frac{c_F + c_B}{2}\right) - c_P \qquad \text{S2.5a}$$

$$\Delta c = \exp\left(\frac{\dot{V}_P}{a} k^{-1}\right)\left(\frac{c_F + \left(\frac{c_F - r\, c_P}{1-r}\right)}{2}\right) - \frac{a}{\dot{V}_P} B\, \Delta c \quad \text{S2.5b}$$

$$\Delta c = \exp\left(\frac{\dot{V}_P}{a} k^{-1}\right)\left(\frac{c_F + \left(\frac{c_F - r\, \frac{a}{\dot{V}_P} B\, \Delta c}{1-r}\right)}{2}\right) - \frac{a}{\dot{V}_P} B\, \Delta c \quad \text{S2.5c}$$

$$\Delta c = c_F \frac{\left(1 + \frac{1}{1-r}\right)}{\left(2\frac{1 + \frac{a}{\dot{V}_P} B}{\exp\left(\frac{\dot{V}_P}{a} k^{-1}\right)} + \left(\frac{r}{1-r}\right)\frac{a}{\dot{V}_P} B\right)} \quad \text{S2.5d}$$

2.6.4 Supplementary Note 2.4: Thermal Energy Use

The thermal specific energy consumption is a measure of the thermal energy required to raise the feed temperature, considering the recovered heat by heat exchangers from the brine and permeate flows. We also have considered the efficiency of heater which shows the performance of heater in converting the electrical power to thermal energy. The following lines provide a detailed derivation of thermal specific consumption equations.

$$\dot{Q} = \dot{Q}_F - \dot{Q}_B - \dot{Q}_P \quad \text{S2.8a}$$

$$\dot{Q}_F = \rho\, c_p \dot{V}_F\, \Delta T \quad \text{S2.8b}$$

$$\dot{Q}_B = \rho\, c_p \dot{V}_B\, \Delta T_B \quad \text{S2.8c}$$

$$\dot{Q}_P = \rho\, c_p \dot{V}_P\, \Delta T_P \quad \text{S2.8d}$$

The change in temperature across either the brine or permeate heat exchangers ΔT_B and ΔT_P can be written as a fraction of the change in feed temperature ΔT and as a function of heat exchanger efficiency η_{hex}. Figure S2.1 shows the boundary conditions of

heat exchangers used at the brine and permeate to recover heat and recycle to feed inlets. Additional heat required to heat the feed to desired temperature after recovering heat from brine and permeate is supplied using a heat pump.

$$\dot{Q}_B = \rho\, c_p \dot{V}_B\, \eta_{hex} \Delta T \qquad \text{S2.8e}$$

$$\dot{Q}_P = \rho\, c_p \dot{V}_P\, \eta_{hex} \Delta T \qquad \text{S2.8f}$$

Then substituting into equation (2.8) and treating density and specific heat as constant across all three terms, we can rearrange to obtain an expression for the specific thermal energy input q.

$$\dot{Q} = \rho\, c_p \Delta T\left(\dot{V}_F - \dot{V}_B\, \eta_{hex} - \dot{V}_P\, \eta_{hex}\right) \qquad \text{S2.8g}$$

$$\dot{Q} = \rho\, c_p \dot{V}_F\, \Delta T(1 - \eta_{hex}) \qquad \text{S2.8h}$$

$$\dot{Q} = \rho\, c_p \frac{\dot{V}_P}{r} \Delta T(1 - \eta_{hex}) \qquad \text{S2.8i}$$

$$q = \frac{\dot{Q}}{\dot{V}_P} = \frac{1}{r} \rho\, c_p \Delta T(1 - \eta_{hex}) \qquad \text{S2.8}$$

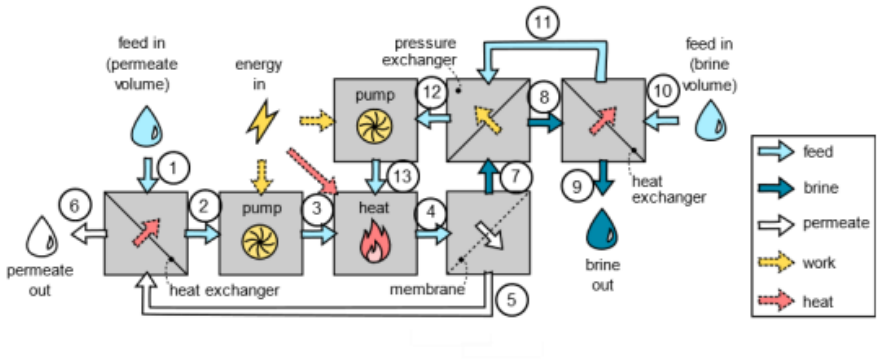

Position	Flow Rate	Pressure	Temperature
1	$\dot{V}_P$	0	T_F
2	$\dot{V}_P$	0	$T_F + \Delta T\ \eta_{hex}$
3	$\dot{V}_P$	Δp	$T_F + \Delta T\ \eta_{hex}$
4	$\dot{V}_F$	Δp	$T_F + \Delta T$
5	$\dot{V}_P$	0	$T_F + \Delta T$
6	$\dot{V}_P$	0	$T_F + \Delta T\ (1- \eta_{hex})$
7	$\dot{V}_B$	Δp	$T_F + \Delta T$
8	$\dot{V}_B$	$\Delta p\ (1- \eta_{pex})$	$T_F + \Delta T$
9	$\dot{V}_B$	$\Delta p\ (1- \eta_{pex})$	$T_F + \Delta T\ (1- \eta_{hex})$
10	$\dot{V}_B$	0	T_F
11	$\dot{V}_B$	0	$T_F + \Delta T\ \eta_{hex}$
12	$\dot{V}_B$	$\Delta p\ \eta_{pex}$	$T_F + \Delta T\ \eta_{hex}$
13	$\dot{V}_B$	Δp	$T_F + \Delta T\ \eta_{hex}$

Figure S2.1 Flow rate, pressure and temperature at different points of thermally enhanced RO system.

2.6.5 Supplementary Note 2.5: Membrane Permeability as a Function of Temperature

Adding heat to the RO process will increase the membrane's apparent permeability to salt [56], [65], [89], [90], [91], [92], [93], [94], [95], [96], [97]. Importantly, most of the observed increase in salt permeability will be due to changes in the fluid properties, rather than any thermally induced changes in the membrane structure itself [98], [99]. It has previously been suggested that salt permeability B is directly proportional to temperature T and inversely proportional to viscosity μ, as described in equation (S2.9a) [43]. Since salt diffusivity D is proportional to T / μ [100], [101], [102], the membrane

salt permeability can also be described as a function of salt diffusivity D, as described in equation (S2.9).

$$B = B_0 \frac{T}{T_0} \frac{\mu_0}{\mu} \quad \text{S2.9a}$$

$$D \propto \frac{T}{\mu} \quad \text{S2.9b}$$

$$\dot{Q} = \rho \, c_p \frac{\dot{V}_P}{r} \Delta T (1 - \eta_{hex}) \quad \text{S2.9}$$

Figure S2.2 shows a collection of salt permeability results at a range of temperatures, as collected from the literature. Equation (2.9) is also plotted and shows agreement with experimental data.

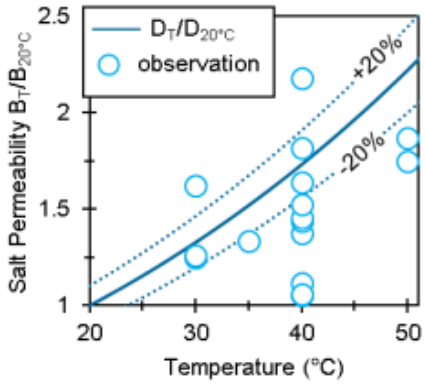

Figure S2.2 Membrane salt permeability as a function of temperature can be predicted from the proportional change in salt diffusivity as described in equation (2.11). This simple model for membrane salt permeability is compared against experimental data from the literature

CHAPTER THREE

THERMALLY DRIVEN REVERSE OSMOSIS: THERMODYNAMICS OF A NOVEL PROCESS THAT USES HEAT FOR DESALINATION AND WATER PURIFICATION

3.1 Introduction

Clean water is essential to life, however access to freshwater remains limited in many parts of the world [103], [104]. Moreover, demand is rapidly increasing due to population growth, increased per capita consumption, environmental pollution, and climate change. For these reasons, engineering solutions are needed to produce freshwater by desalinating salt water and treating wastewater for reuse [105], [106], [107].

Using heat to separate water and solutes is an ancient concept, and can be done as simply as by boiling water to collect condensate. In recent years, there has been renewed interest in developing thermally driven water separation technologies because of their compatibility with a number of sustainability metrics [108], [109], [110]. Namely, thermal energy can be plentiful and relatively cheap, and is available from renewable or residual sources such as solar radiation, ocean thermal gradients, geothermal energy, and industrial waste heat. A number of processes have been developed to make use of thermal energy, including multi-effect distillation, multi-stage flash distillation, membrane distillation, solar stills, and others [111], [112], [113]. While each have their own merits, all suffer from the fact that thermal separation is inherently energy intensive. This is because in all cases, separation is achieved by the phase change of water from liquid to vapor, which occurs preferentially relative to solutes and impurities in the feed. The heat of vaporization of seawater is approximately 667 kWh per m^3 of desalinated water [114].

Although some of this heat can be recovered during condensation, even highly efficient thermal systems consume on the order of 10-100 kWh/m^3 [111].

In contrast, the energy requirements for reverse osmosis (RO) are much lower. This is one of the reasons that RO has grown to dominate the desalination industry, with global capacity now approaching 100 million m^3/day [115]. The basic RO process uses an applied pressure to force clean water across a highly selective semi-permeable membrane that rejects solutes and other impurities. As such, RO avoids the energy intensive step of vaporization. At its thermodynamic limit, approximately 0.8 kWh of energy is needed to produce 1 m^3 of clean water permeate from seawater [116]. Commercial RO desalination plants consume on the order of 1-10 kWh/m^3 [117]. This is significantly less energy than used for thermal separation, but it should be noted that RO uses energy in the form of work, usually electricity. This is more costly than low-grade heat and therefore energy use remains one of the principal operating costs of RO.

Considering the respective advantages of both thermal separation (use of cheap, low-grade heat) and RO (inherent energy efficiency) raises the question of whether a process could be designed to take advantage of both. Several attempts have been made. The most common examples involve integration of a heat engine with RO, wherein heat is used to produce power which is then transferred to drive water permeate across a membrane. Most of the related literature considers the organic Rankine cycle for such a concept, as it is well suited for operation at low temperatures [118], [119], [120]. This can make use of a wide range of heat sources including solar radiation [121], [122], [123], [124], [125], geothermal energy [126], [127], and waste heat [128], [129]. This approach is conceptually simple and has several advantages as it combines two well-understood

technologies, namely the heat engine and RO. On the other hand, such systems have so far not found any practical applications because operating heat engines at low temperatures is inherently inefficient (which results in the need for large capital-intensive infrastructure), and because there is added cost and complexity to building a thermal power plant in addition to a desalination plant.

Most recently a simplified thermally driven reverse osmosis (TDRO) concept was proposed by Peter Godart at MIT, which he refers to as heat-driven RO [130], [131]. Figure 3.1 illustrates the basic process. It consists of a piston system filled with working fluid, connected to a load piston filled with RO feed solution, which is outfitted with a semipermeable membrane module. As heat is supplied to the working fluid, temperature and pressure increase at constant volume until the pressure that is mechanically transferred to the load exceeds the osmotic potential of the RO feed solution. At this point clean water is driven across the membrane as the working fluid expands. After reaching some target water recovery volume, the working fluid is cooled and returned to its initial volume, drawing feed water into the RO module to prepare for the next stroke. When the initial volume and pressure are at ambient conditions, then the cycle is completed passively and the work associated with the return stroke is zero. For semi-continuous operation, a number of such cylinders can be synchronized.

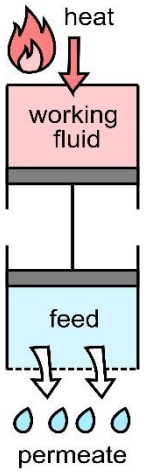

Figure 3.1 A simplified embodiment of the thermally driven reverse osmosis (TDRO) concept. A working fluid is heated from some thermal energy source (e.g. solar, geothermal, ocean thermal, etc.). Pressure of the working fluid increases and is applied to a volume of feed water (e.g. seawater, brackish water, wastewater, etc.). When pressure of the feed water exceeds its osmotic potential, the working fluid begins to expand, driving water to permeate through a semipermeable membrane, thereby producing clean water.

In his pioneering work introducing the concept, Godart [131] outlined the principals of operation and defined governing equations for the mass and energy balance of the process. Using thermodynamic analysis, he evaluated performance and reported a first law efficiency of 5.7 % and a gain output ratio of 49. Note, that first law efficiency is defined as the ratio of work output to heat input, and gain output ratio is the ratio of enthalpy of vaporization to heat input. While encouraging, these performance results lack important context. In one way, they overstate performance because these values are obtained at unrealistic recovery ratios of zero. In another way, they understate performance because Godart made no effort to optimize the size of the working piston. As we demonstrate further on, the size of the working piston relative to the size of the RO feed piston has a very important influence on the ratio of heat input to work output. With proper consideration, it is possible to achieve both better performance and more realistic recovery ratios.

Therefore, in this study, we revisit the thermodynamics of the novel TDRO concept to develop an expression for the heat of separation as a function of the piston sizing ratio. The effect of sizing ratio on performance metrics such as first law efficiency, second law efficiency, and the gain output ratio are considered. Together, these metrics provide insight into the performance tradeoffs that must be managed when sizing ratio is being set at the design stage. These metrics also provide a useful measure of how well the TDRO concept compares to the current state-of-the-art for desalination and water treatment, which includes other technologies such as reverse osmosis and membrane distillation. Finally, ways in which TDRO can contribute to a sustainable water future are outlined.

3.2 Theory

3.2.1 Reverse Osmosis and the Work of Separation

In reverse osmosis (RO), work is used to pressurize concentrated feed solution above its osmotic potential and drive clean water permeate across a selective membrane, thereby separating clean water from salts and other impurities in the source. Figure 3.2 shows a simplified and idealized RO system. To improve the energy efficiency of the process, a portion of the work supplied to the feed can be recovered from the super-concentrated waste brine and recycled back to a portion of the incoming feed via a pressure exchanger. Assuming perfect recovery at the exchanger, the work associated with RO W is then the integral of the pressure applied above atmosphere p over the change in feed volume V (equation 3.1) [132], [133].

$$W = \int p \, dV \tag{3.1}$$

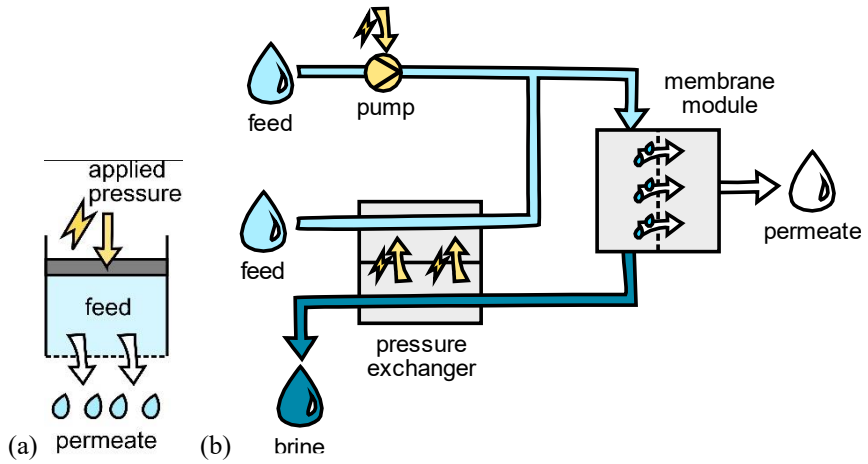

Figure 3.2 Schematic of (a) a simplified and idealized reverse osmosis (RO) batch process and (b) a more practical continuous RO system. In both cases, work is done to pressurize feed solution above its osmotic potential, and thereby drive clean water permeate across the membrane.

In order to drive water permeate across the membrane, it is necessary for the applied pressure to overcome the osmotic pressure of the feed. Various empirical relations and property tables have been proposed to describe osmotic pressure π, but it can be approximated by the Van't Hoff equation (equation 3.2a). Importantly, osmotic pressure increases throughout the RO process as more and more water permeate is recovered and the feed becomes increasingly concentrated. Taking a mass balance of the water and salt contained in the initial feed volume V_F and concentration c_F, and assuming that the membrane is perfectly selective, osmotic pressure can be written as a function of the permeate volume ΔV (equation 3.2b). For convenience, permeate volume can also be normalized over the feed volume and expressed as the recovery ratio $r = \Delta V / V_F$ (equation 3.2c).

$$\pi \approx i\, R\, T\, c \tag{3.2a}$$

$$\pi \approx i\, R\, T\, c_F \left(\frac{V_F}{V_F - \Delta V}\right) = \pi_F \left(\frac{V_F}{V_F - \Delta V}\right) \tag{3.2b}$$

$$\pi \approx i\,R\,T\,c_F\left(\frac{1}{1-r}\right) = \pi_F\left(\frac{1}{1-r}\right) \quad 3.2c$$

Where i is the number of salt ions, R is the gas constant, T is the absolute temperature, c_F is concentration, V_F is feed flow rate, ΔV is permeate water, r is recovery ratio, and π_F is the osmotic pressure of the initial feed solution.

Figure 3.3 shows the P-V diagram of RO where osmotic pressure is a function of permeate volume. In a standard RO process, constant pressure $p = C$ is applied to the feed. This is shown in Figure 3.3(a). In such a process, work as defined in equation (3.1) reduces simply to the product of the constant pressure and the permeate volume (equation 3.3a). This work is illustrated in Figure 3.3(a) by the yellow highlighted area that is the product of applied pressure and permeate volume. Also shown on Figure 3.3(a) is the equilibrium point that is established when osmotic pressure increases enough to equal the applied pressure. This equilibrium point can be determined analytically by solving equation (3.2) for the condition where $C = \pi$. Using this approach, work can be rewritten in terms of the permeate volume (equation 3.3b). For convenience, work can also be normalized per unit of permeate volume and expressed as the specific work $W/\Delta V$ (eq. 3.3c).

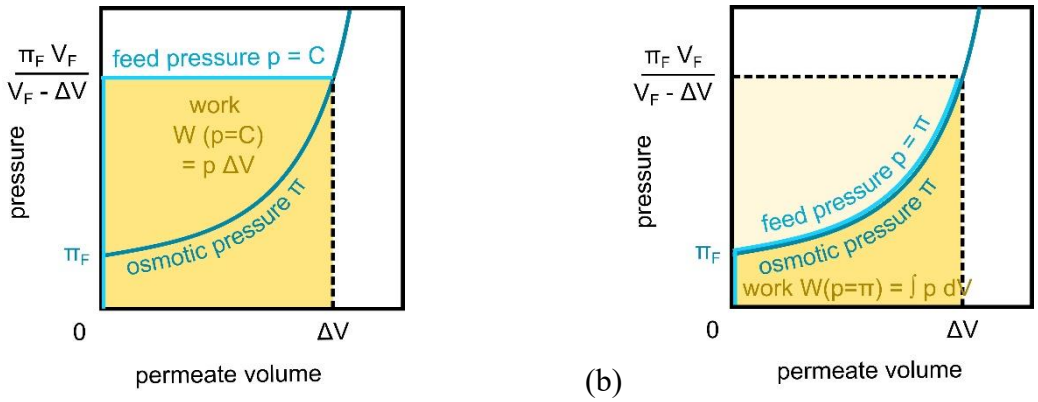

Figure 3.3 The variation of pressure with permeate volume for a) constant pressure and b) variable pressure scenarios.

$$W_{p=C} = \int_0^{\Delta V} p\, dV = C\, \Delta V \tag{3.3a}$$

$$W_{p=C} = \pi_F \left(\frac{V_F}{V_F - \Delta V}\right) \Delta V \tag{3.3b}$$

$$\frac{W_{p=C}}{\Delta V} = \pi_F \left(\frac{1}{1-r}\right) \tag{3.3c}$$

Alternatively, RO can be operated as a batch process, with a variable applied pressure. This can be done to save energy by maintaining applied pressure only slightly above the osmotic pressure. Of course, this does slow the rate of water permeate, since this rate will be proportional to the difference between applied and osmotic pressure. Taken to its thermodynamic limit, a perfectly reversible process is infinitely slow and is achieved when applied pressure is kept equal to the osmotic pressure. Figure 3.3(b) shows the reversible RO process, where applied pressure is equal to osmotic pressure. In such a process, work from equation (3.1) is then the integral of osmotic pressure over the permeate volume (equation 3.4a). This work is illustrated by the yellow highlighted area in Figure 3.3(b). A light-yellow area is also highlighted to contrast with work from the equivalent irreversible case. As shown, the yellow area and hence work is reduced. Using

the expression for osmotic pressure from equation (3.2), it is possible to solve the integral analytically and obtain a result for work as a function of the permeate volume (equation 3.4b). The specific work can also be written by normalizing per unit of permeate volume (equation 3.4c). A detailed derivation is included in Supplementary Note 3.1.

$$W_{p=\pi} = \int_0^{\Delta V} \pi \, d\Delta V = \int_0^{\Delta V} \pi_F \left(\frac{V_F}{V_F - \Delta V}\right) d\Delta V \tag{3.4a}$$

$$W_{p=\pi} = \pi_F \, V_F \; ln\left(\frac{V_F}{V_F - \Delta V}\right) \tag{3.4b}$$

$$\frac{W_{p=\pi}}{\Delta V} = \frac{\pi_F}{r} \; ln\left(\frac{1}{1-r}\right) \tag{3.4c}$$

To illustrate, consider RO desalination for a number of common feed sources such as seawater (c_F = 35 g/l), brackish water (c_F = 10 g/l), and produced water (c_F = 70 g/l). Figure 3.4 shows the specific work of RO for each of these across a range of recovery ratios. For example, at a recovery ratio r = 0, approximately 0.8 kWh of work is needed to recover 1 m^3 of clean water permeate from seawater. At more reasonable recovery ratios such as r = 0.5, the specific work is closer to 1.7 kWh/m^3 when using a constant pressure and 1.1 kWh/m^3 for a variable pressure reversible process.

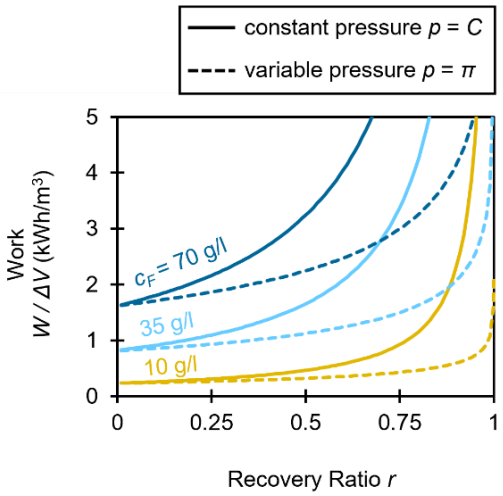

Figure 3.4 Work per unit volume of water permeate $W / \Delta V$ that is required to drive RO desalination from a variety of feed sources, including seawater (c_F = 35 g/l), brackish water (c_F = 10 g/l), and produced water (c_F = 70 g/l). Operating the RO process with a variable pressure that is equal to the osmotic pressure $p = \pi$ (i.e. reversible process) requires less work that operation with a constant applied pressure $p = C$ (i.e. irreversible process).

3.2.2 Thermally Driven Reverse Osmosis and the Heat of Separation

In a thermally driven reverse osmosis (TDRO) system, heat is used to pressurize a working fluid that expands against a piston set that is connected to a RO load (as described in Section 3.2.1), which drives water permeate across a semipermeable membrane. Figure 3.5 shows a simplified and idealized thermally driven RO system. For our purposes we will analyze a batch process, but the system could be practically designed for continuous operation with a series of synchronized pistons. Supplementary Note 3.2 provides additional schematics of the process and cycle.

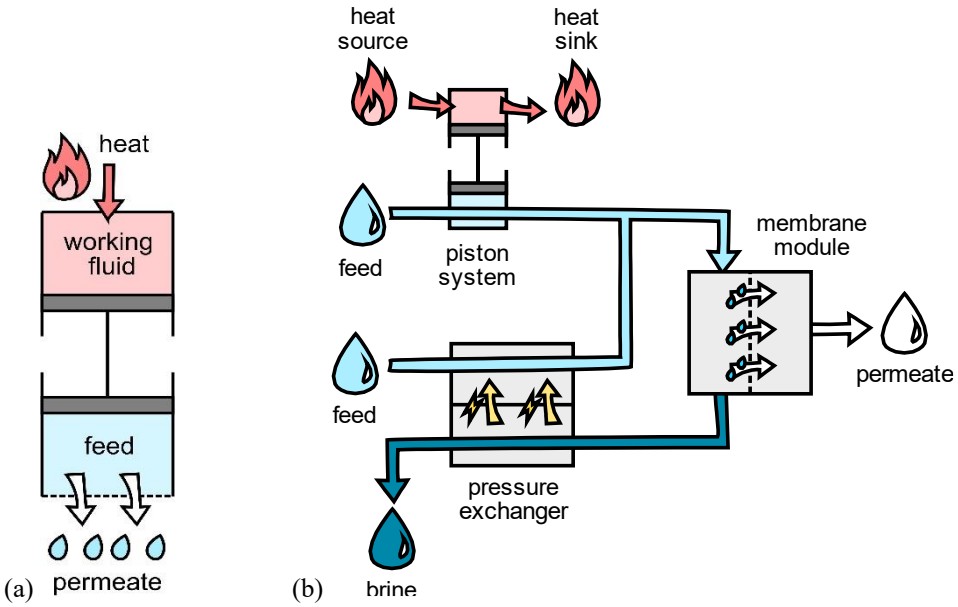

Figure 3.5 Schematic of (a) a simplified and idealized thermally driven reverse osmosis (RO) batch process, and (b) a more practical, continuous thermally driven RO system. In both cases, heat is used to expand a working fluid, thereby pressurizing solutions above its osmotic potential and driving clean water permeate across the membrane.

In this system, the heat required to thermally drive desalination Q is equal to the sum of the moving boundary work of the piston W together with the change of energy of the working fluid, which will be in the form of internal energy ΔU (equation 3.5).

$$Q = \Delta U + W \tag{3.5}$$

Because force and displacement will be common across the piston set, work done by the working fluid will be equal to work done on the RO feed fluid. Therefore, the term for work can be developed just as previously described in Section 3.3.1 For the case where RO is operated at a constant applied pressure $p = C$, the heat required to drive TDRO is defined in equation (3.6).

$$Q_{p=C} = \Delta U + \int_0^{\Delta V} C \, dV \tag{3.6a}$$

$$Q_{p=C} = \Delta U + \pi_F \left(\frac{V_F}{V_F - \Delta V}\right) \Delta V \quad 3.6b$$

$$\frac{Q_{p=C}}{\Delta V} = \frac{\Delta U}{\Delta V} + \pi_F \left(\frac{1}{1-r}\right) \quad 3.6c$$

And for the case where RO is operated in an ideal reversible process with a variable applied pressure $p = \pi$, the heat required to drive TDRO is defined in equation (3.7).

$$Q_{p=\pi} = \Delta U + \int_0^{\Delta V} \pi dV \quad 3.7a$$

$$Q_{p=\pi} = \Delta U + \pi_F V_F \ ln\left(\frac{V_F}{V_F - \Delta V}\right) \quad 3.7b$$

$$\frac{Q_{p=\pi}}{\Delta V} = \frac{\Delta U}{\Delta V} + \frac{\pi_F}{r} \ ln\left(\frac{1}{1-r}\right) \quad 3.7c$$

3.2.3 Design Considerations

Maintaining the working fluid as a two-phase saturated mixture has many advantages for the TDRO process [131]. Namely, it exploits an exponential relationship between pressure and temperature, allowing for large increases in pressure to be achieved with only modest increases in temperature [134]. This can facilitate the use of low-grade thermal energy sources, and can reduce heat loss, which will be proportional to temperature. Figure 3.6 shows the P-V diagram of TDRO when operated with a two-phase saturated working fluid. Figure 3.6(a) shows the process when a constant pressure is maintained against the feed $p = C$ (irreversible RO load), and Figure 3.6(b) shows the process when a variable pressure is maintained against the feed $p = \pi$ (reversible RO load). The yellow area on the figure shows work, which is equal to the RO load. Also, for the reversible load, a light-yellow area is included to contrast with the work of the equivalent irreversible load. As shown, the yellow area shifts slightly to the left in the

reversible case, since the initial operating pressure is lower, and therefore the specific volume of the saturated liquid is lower.

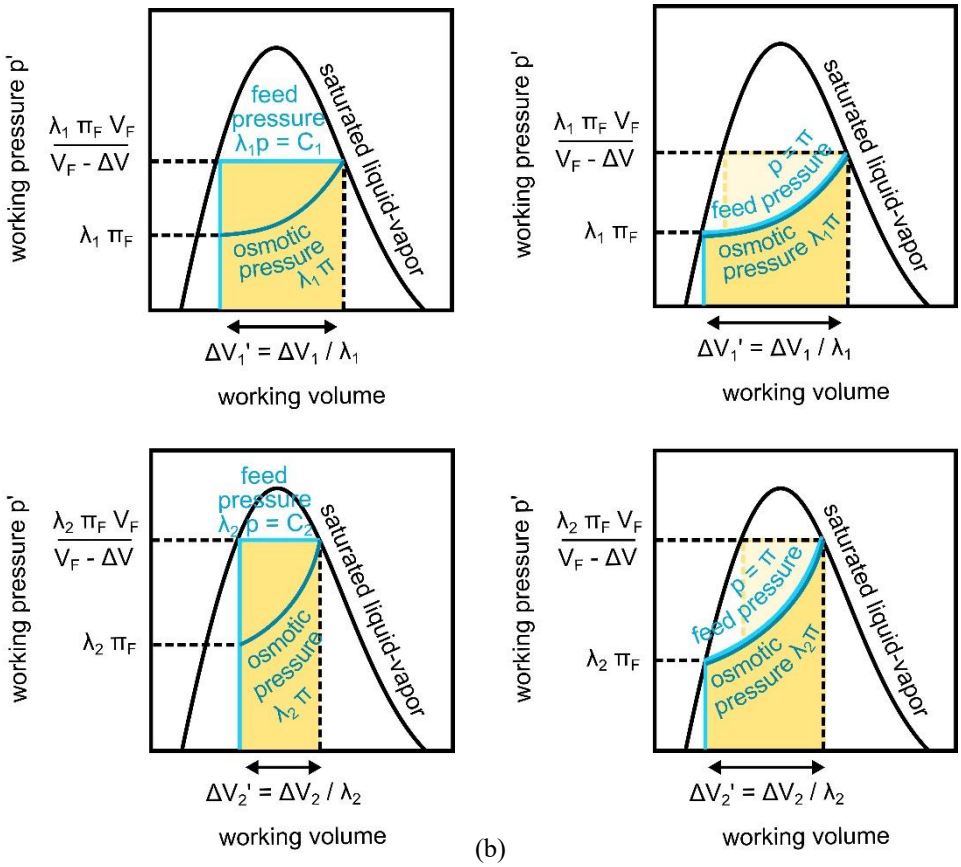

Figure 3.6 P-V diagram for thermally driven reverse osmosis using a saturated two-phase working fluid. Operation is compared for (a) maintaining a constant pressure against the feed p = C (irreversible RO load), and (b) for a reversible process with varying pressure against the feed such that p = π (reversible RO load). For both cases, operation with a small sizing ratio is compare to a large sizing ratio, where $\lambda_1 < \lambda_2$.

Several important observations can be made from Figure 3.6. First, for both cases (a) and (b), operation with a small sizing ratio is compared to operation with a large sizing ratio, $\lambda_1 < \lambda_2$. The sizing ratio is defined here as the area of the piston acting on the feed relative to the area of the piston acting on the working fluid, $\lambda = A / A'$. The ratio of this piston set can be selected at the design stage. Because force and displacement will be common across the piston set, the pressure and change in volume of the working fluid p'

and $\Delta V'$ can be related to the feed through the sizing ratio, where $\lambda = p' / p = \Delta V / \Delta V'$. Therefore, for a given feed pressure and permeate volume, the sizing ratio can be used to either allow the working fluid to operate at low pressure over a large volume, or to be more compact and operate at high pressure over a small volume. In either case, the sizing ratio will have no influence on work (because the product of pressure and change in volume for the working fluid and feed fluid are equal), but it can have a significant influence on the change in internal energy. Or in other words, while changing the sizing ratio does not change the area under the P-V curve (i.e. work), it does change the initial and final states (i.e. change in internal energy) and therefore the heat required.

Second, maintaining the working fluid in a two-phase saturated state, imposes limitations on the sizing ratio. As illustrated in Figure 3.6, at one extreme, if the sizing ratio is too large, working pressure will exceed the critical pressure p_{cr}. At the other extreme, if the sizing ratio is too small, the feed fluid will not return to atmospheric pressure p_{atm} unless a heat sink can provide cooling below ambient temperature T_{atm} (which we avoid for practical reasons). This is important, because such conditions are necessary for the system to return to its initial position passively, and close the cycle without requiring work. The resulting limits on the sizing ratio are provided in equation (3.8), where $p_{sat@\ Tatm}$ is the saturation pressure of the working fluid at ambient temperature. Figure 3.7 illustrates, the maximum and minimum sizing ratios for a variety of possible working fluids as a function of recovery ratio. For example, at a typical recovery ratio r = 0.5, the sizing ratio must be between $0.02 < \lambda < 3.72$ in order to maintain water in a two-phase saturated state.

$$\frac{p_{sat,g\,@\,T_{atm}}}{p_{atm}} + 1 = \lambda_{min} < \lambda < \lambda_{max} = p_{cr,g}\frac{(1-r)}{\pi_F} \qquad 3.8$$

Where p_{cr} and p_{sat} are written in terms of gage pressure. Although somewhat unconventional to expressed saturation and critical pressure with respect to gage, this is done for convenience, since osmotic pressure and hence the rest of the analysis is developed in terms of gage pressures.

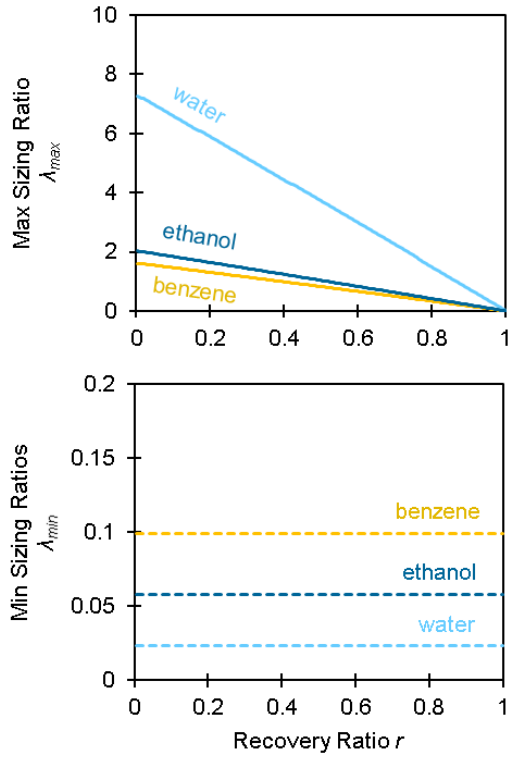

Figure 3.7 Maximum and minimum sizing ratios λ_{min} and λ_{max} for a variety of possible working fluids, as a function of the desired water recovery ratio r. These limits arise from the desire to maintain working fluid as a two-phase saturated mixture. The maximum is established because the working fluid pressure cannot exceed the critical point. The minimum is established by the temperature of the heat sink (which we take here as the ambient atmospheric temperature), because this is the minimum temperature of the working fluid, and the saturation pressure associated with this temperature must yield a feed pressure less than or equal to atmosphere in order for the feed piston to reset with a new batch of seawater.

Third, there is some sizing ratio that will minimize the change in internal energy, and thereby minimize the heat of desalination of the process. Equation (3.9b) shows the heat

of desalination written in terms of the sizing ratio, where u is the specific internal energy, and v is the specific volume. A superficial analysis of equation (3.9b) might suggest that to minimize heat of desalination, it is desirable to have the sizing ratio $\lambda \rightarrow \infty$, or at least approach the maximum limit for maintaining a two-phase working fluid $\lambda \rightarrow \lambda_{max}$. However, there is a tradeoff with this. As the sizing ratio increases, the change in specific volume of the working fluid $\Delta v'$ decreases, approaching zero when the sizing ratio reaches its limit. In addition, there will be a change in the specific internal energy. It is therefore necessary to carefully analyze the sizing ratio λ, the specific internal energy $\Delta u'$, and the specific volume $\Delta v'$ all together, in order to minimize their combined contribution to the heat of desalination.

$$\frac{Q}{\Delta V} = \frac{\Delta U'}{\Delta V} + \frac{W}{\Delta V} \tag{3.9a}$$

$$\frac{Q}{\Delta V} = \frac{1}{\lambda}\frac{\Delta u'}{\Delta v'} + \frac{W}{\Delta V} \tag{3.9b}$$

$$\frac{Q}{\Delta V} = \frac{p_2}{p_2{}'}\frac{(u_2{}' - u_1{}')}{(v_2{}' - v_1{}')} + \frac{W}{\Delta V} \tag{3.9c}$$

$$\frac{Q}{\Delta V} = K\,\frac{\pi_F}{1-r} + \frac{W}{\Delta V} \tag{3.9d}$$

To identify the sizing ratio that will minimize the internal energy gain of the working fluid, it is helpful to define the initial and final states of the working fluid. Equation (3.9c) shows the initial and final states denoted with subscripts 1 and 2, respectively. The associated properties are summarized in Table 3.1, where subscripts f and g denote saturated liquid and vapor, respectively. Finding the best sizing ratio is then a matter of analyzing the properties of the selected working fluid at its initial and final states to identify the minimum ($u_2' - u_1'$) / ($v_2' - v_1'$) / p_2'. For convenience we denote this term as

the dimensionless *K* ratio as shown in equation (3.9d). Figure 3.8 shows the *K* ratio as a function of sizing ratio λ for a range of different feed concentrations c_F and recovery ratios *r*. Results are shown for several possible working fluids in both a constant pressure irreversible process and a variable pressure reversible process. As shown, the selection of the working fluid and the sizing ratio λ can have a significant effect on the dimensionless *K* ratio, and can be used to minimize the change in internal energy of the TDRO process.

Table 3.1 Properties of the working fluid at its initial and final states as a function of the sizing ratio λ. Properties are shown for the case where thermo-driven RO is operated at constant pressure (irreversible) and where it is operated at variable pressure (reversible). Initial conditions refer to the ambient conditions at which the system starts and returns to, at the completion of the cycle. This is not to be confused with the condition at which the RO process begins, which would be $p' = \frac{\lambda \pi_F}{1-r}$ for the irreversible case and $p' = \lambda \pi_F$ for the reversible case.

	At constant pressure (irreversible)		At variable pressure (reversible)	
	Initial	Final	Initial	Final
Working pressure *p*'	$p'_1 = (\lambda - 1)\, p_{atm}$	$p'_2 = \frac{\lambda \pi_F}{1-r}$	$p'_1 = (\lambda - 1)\, p_{atm}$	$p'_2 = \frac{\lambda \pi_F}{1-r}$
Specific volume *v*'	$v'_1 = v'_{f\,@\,p'_2}$	$v'_2 = v'_{g\,@\,p'_2}$	$v'_1 = v'_{f\,@\,p' = \lambda \pi_F}$	$v'_2 = v'_{g\,@\,p'_2}$
Specific internal energy *u*'	$u'_1 = u'_{@\,p'_1 \text{ and } v'_1}$	$u'_2 = u'_{g\,@\,p'_2}$	$u'_1 = u'_{@\,p'_1 \text{ and } v'_1}$	$u'_2 = u'_{g\,@\,p'_2}$

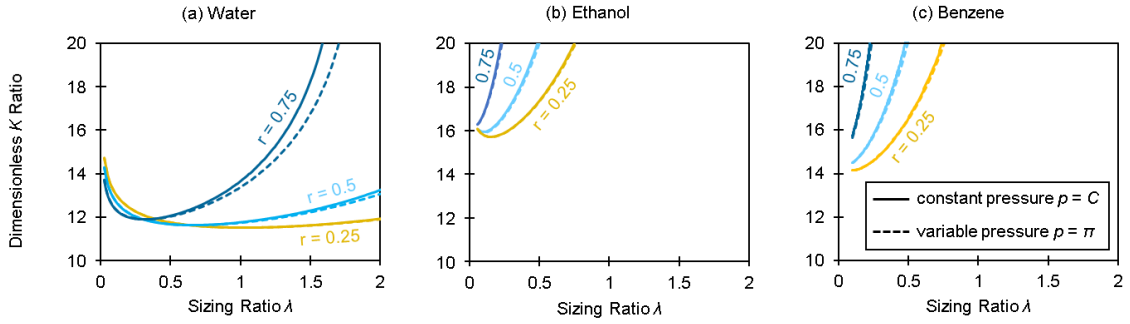

Figure 3.8 The dimensionless *K* ratio as a function of sizing ratio λ for a variety of possible working fluids including (a) water, (b) benzene, and (c) ethanol. The dimensionless *K* ratio is a measure of the change in internal energy of the working fluid, which is undesirable, as it adds to the heat of separation. Results are shown for desalination of seawater with feed concentration c_F = 35 g/l. Operation with a variable pressure $p = \pi$ (hatched line) is compared to operation with a constant pressure $p = C$ (solid line).

Combining equations (3.6) and (3.9), it is possible to reduce the expression for the heat of separation of thermo-driven RO to a simple function of the osmotic pressure of the feed π_F, the desired recovery ratio of the process r, and the dimensionless K ratio (which is a function of the sizing ratio λ as defined in equation (3.9) and in Table 3.1). The simplified expression is provided in equation (3.10a) for the case of an irreversible constant pressure process and (3.10b) for a reversible variable pressure process.

$$Q_{p=C} = \Delta U + \int_0^{\Delta V} C \, dV \tag{3.10a}$$

$$Q_{p=C} = \Delta U + \pi_F \left(\frac{V_F}{V_F - \Delta V}\right) \Delta V \tag{3.10b}$$

3.2.4 Efficiency and Performance

The performance of TDRO can be evaluated with several metrics. The first law efficiency η_I of the process will be the ratio of work done on the RO load W relative to the heat input to the working piston Q. This ratio can be reduced as described in equation (3.11b) for the case of an irreversible constant pressure process and (3.11c) for a reversible variable pressure process. This measure of performance is useful because it provides a direct comparison between thermo-driven RO and the alternative of simply using electric or mechanical work to directly power RO. Of note, equation (3.11) can be used to relate heat and work for both the case of a reversible RO load and an irreversible RO load. An alternative definition of the first law efficiency, relating heat only to the minimum reversible work, which is the useful RO load, is provided in Supplementary Note 3.3 along with accompanying results.

$$\eta_I = \frac{W}{Q} \tag{3.11a}$$

$$\eta_{I,p=C} = (K+1)^{-1} \tag{3.11b}$$

$$\eta_{I,p=\pi} = \left(\frac{K}{\frac{1-r}{r}\, ln\left(\frac{1}{1-r}\right)} + 1 \right)^{-1} \tag{3.11c}$$

The second law efficiency η_{II} is also a useful metric because it evaluates the performance with respect to the quality of the heat source, notably its temperature. This is defined as the ratio of first law efficiency η_I relative to the Carnot efficiency η_{Carnot}.

$$\eta_{II} = \frac{\eta_I}{\eta_{Carnot}} = \frac{\eta_I}{1 - T_{atm}/T_2'} \tag{3.12}$$

Where T_{atm} is the ambient temperature of the environment which acts as a heat sink, and T_2' is the final operating temperature of the working fluid, which is the temperature of the heat source.

Thermal desalination processes are also commonly evaluated in terms of their gain output ratio *GOR*, which is a ratio of the enthalpy of vaporization ΔH relative to the heat input Q. This is a useful metric because it provides a comparison between the thermo-driven RO process and the alternative of simply boiling water to separate clean water from less volatile salts and impurities.

$$GOR = \frac{\Delta H}{Q} \tag{3.13}$$

3.3 Results

3.3.1 Sizing the TDRO Working Piston to Minimize Energy Use

The size of the working piston relative to the size of the feed piston is an important design variable with several implications for TDRO. As defined earlier, the sizing ratio is the change in feed volume relative to the change in working volume $\lambda = \Delta V / \Delta V'$, which

is also inversely proportional to the pressure ratio of the two pistons $\lambda = p' / p$. The sizing ratio has an important influence on the energy requirements of TDRO. To illustrate, consider the case where saturated water is used as a working fluid to drive TDRO desalination as shown in Figure 3.9. As shown, there is clearly some sizing ratio that will minimize the specific heat input of desalination. For example, for seawater $c_F = 35$ g/l with a recovery ratio $r = 0.5$, the minimum heat is obtained when $\lambda = 0.63$. At this point, specific heat input $Q/\Delta V = 20.5$ kWh/m^3 for TDRO with an irreversible load and 20.0 kWh/m^3 with a reversible load. These are very close because even though operation at variable pressure does reduce the work involved, work contributes relatively little to the heat as compared to internal energy. This suggests that there is relatively little benefit to increasing pressure in a deliberate, reversible way, as it has little influence on the required heat input. This is somewhat ironic, as from a practical standpoint, TDRO is easy to control because operating pressure can be directly controlled via temperature, which can be easily controlled by adjusting heat input. Also, work is shown to be unaffected by the sizing ratio because the integral of pressure over the change in volume remains constant for a given load. On the other hand, the change in internal energy of the process is sensitive to the sizing ratio and is minimized when the ratio of internal energy, specific volume, and working pressure is minimized, as expressed earlier by the dimensionless ratio $K = (u_2' - u_1') / (v_2' - v_1') / p_2'$. For other examples, where recovery ratio and feed concentration increase, the minimum heat increases and the associated sizing ratio shifts to the left.

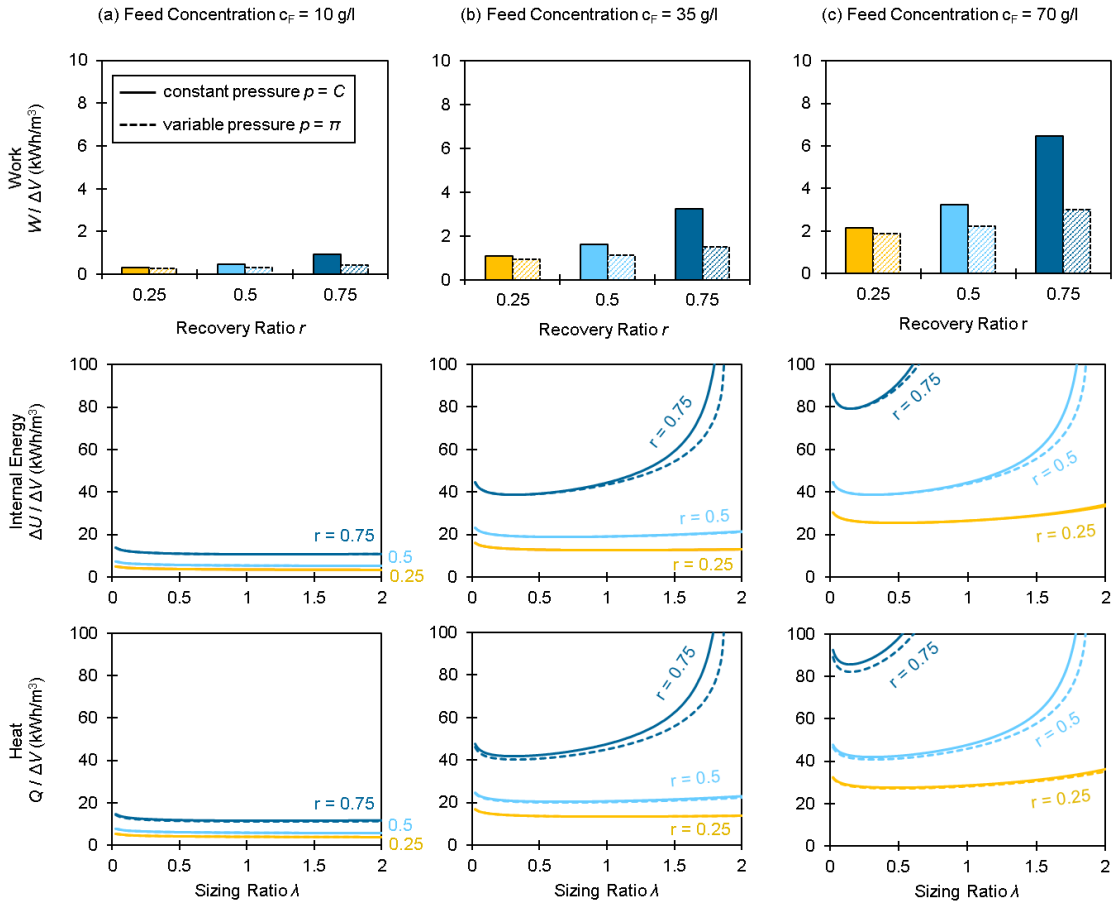

Figure 3.9 Work, internal energy, and heat required to drive TDRO as a function of the sizing ratio when saturated water is used as the working fluid. Results are shown for different recovery ratios r and different feed sources including (a) brackish water with concentration c_F = 10 g/l, (b) seawater at c_F = 35 g/l, and (c) produced water at c_F = 70 g/l. Results are compared for operation with constant applied pressure $p = C$ (i.e. irreversible process) and with a variable pressure that is equal to the osmotic pressure $p = \pi$ (i.e. reversible process).

Interestingly, even though the best sizing ratio varies with feed concentration and recovery ratio, the associated temperature and pressure of the working fluid remain constant. To illustrate, consider again the case where saturated water is used as a working fluid to drive TDRO desalination as shown in Figure 3.10. The figure for heat versus sizing ratio is repeated from Figure 3.9, but now also shown are the working pressure and working temperature that are associated with the sizing ratio. As shown, even though the

best sizing ratio shifts to the left as feed concentration and recovery ratio increase, the associated working pressure and temperature are constant. For example, even across a range of different feed concentrations and recovery ratios, the best working pressure and temperature are p' = 36.9 bar (gage) and T' = 247 °C respectively. With this in mind, we can denote the most efficient working pressure and temperature as p^* and T^*, and then the optimal sizing ratio can be written as a function of the recovery ratio and feed concentration, $\lambda^* = p^* (1 - r) / \pi_F$. The most efficient working pressure and temperature will be unique for any given working fluid, as described in the next section.

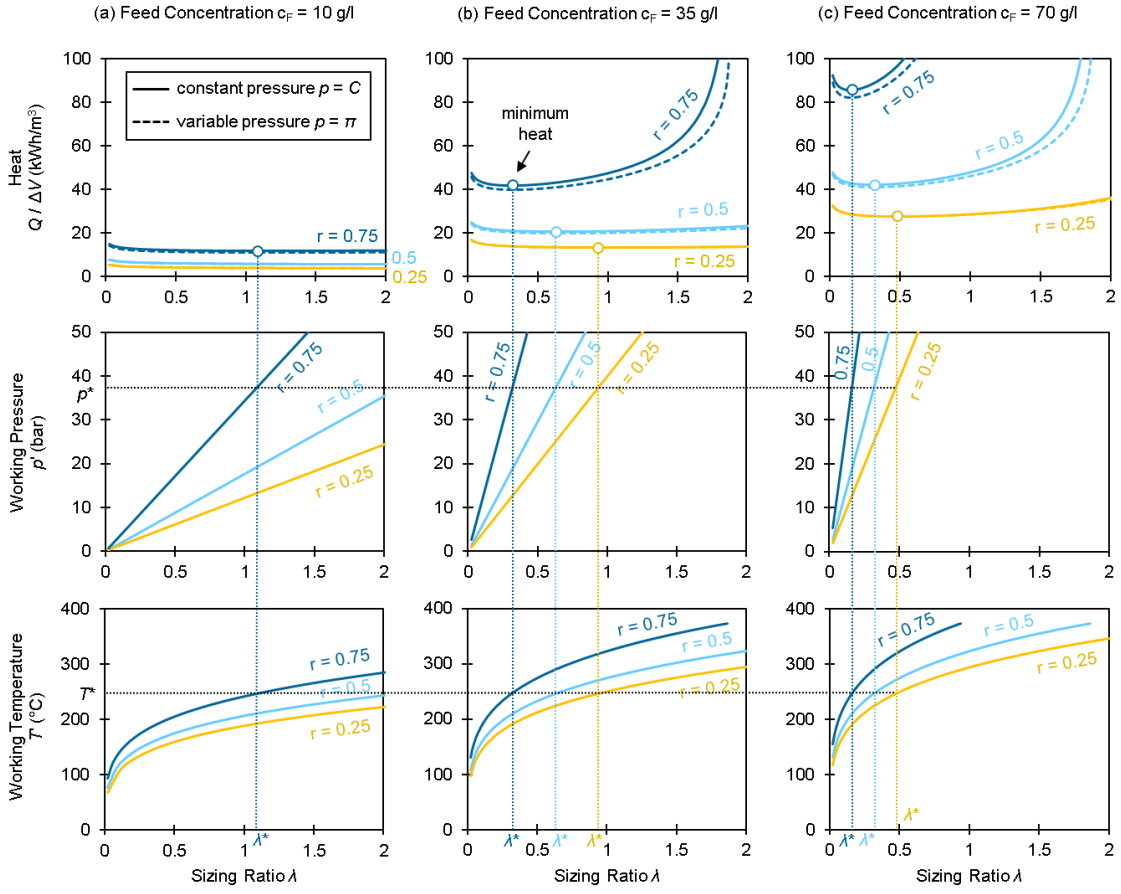

Figure 3.10 Heat of TDRO as a function of the sizing ratio, along with the associated pressure and temperature of the working fluid, which is taken here as saturated water. Results are shown for different recovery ratios r and different feed sources including (a) brackish water with concentration c_F = 10 g/l, (b) seawater at c_F = 35 g/l, and (c)

produced water at c_F = 70 g/l. Results are compared for operation with constant applied pressure $p = C$ (i.e. irreversible process) and with a variable pressure that is equal to the osmotic pressure $p = \pi$ (i.e. reversible process).

Therefore, the sizing ratio is an important design parameter as it can be used to minimize the amount of heat required to drive TDRO. It does this by ensuring that the working fluid is maintained at the most efficient operating pressure and temperature, given a certain source concentration and desired recovery ratio. Since it is unlikely that the sizing ratio will be able to change throughout the life of the device, it is important to carefully select a sizing ratio that will perform well across a range of anticipated conditions. For example, from Figure 3.10, a sizing ratio $\lambda \sim 0.5$ performs consistently well across the range of recovery ratios and feed concentrations shown and could reasonably be taken as a default value. However, in addition to the energy efficiency, the sizing ratio influences several other important tradeoffs in the process. For example, as shown in Figure 3.10 a smaller sizing ratio has the additional benefit of lowering the operating pressure and temperature of the working fluid. This can reduce heat loss and the mechanical load on the piston while also making use of lower quality heat sources. On the other hand, a smaller sizing ratio has the disadvantage of increasing the volume of the working fluid, requiring the working piston to be larger and/or cycle more quickly in order to produce water at a certain rate.

3.3.2 Selecting the Working Fluid to Minimize TDRO Energy Use, Temperature, and Pressure

In addition to the sizing ratio, selection of the working fluid also has an important impact on the performance of TDRO. Figure 3.11 shows the heat of TDRO for three different working fluids: water, ethanol, and benzene. The most efficient working

pressure and temperature for each of the fluids are p^* = 36.9 bar and T^* = 247 °C for water, 6.2 bar and 134 °C for ethanol, and 5.8 bar and 150 °C for benzene. The minimum specific heat input obtained with each of the fluids is $Q/\Delta V$ = 20.5 kWh/m^3 for water, 27.4 kWh/m^3 for ethanol, and 25.1 kWh/m^3 for benzene. Clearly, the minimum heat among the three is with saturated water as the working fluid. One could argue that the minimum heat for ethanol and benzene occurs at a lower working pressure and temperature (which is advantageous for reducing heat loss and mechanical loads on the device), but at comparably low pressures and temperatures water is still more energy efficient. For this reason, and because water is common and non-toxic, we recommend water as the preferred working fluid from among those considered.

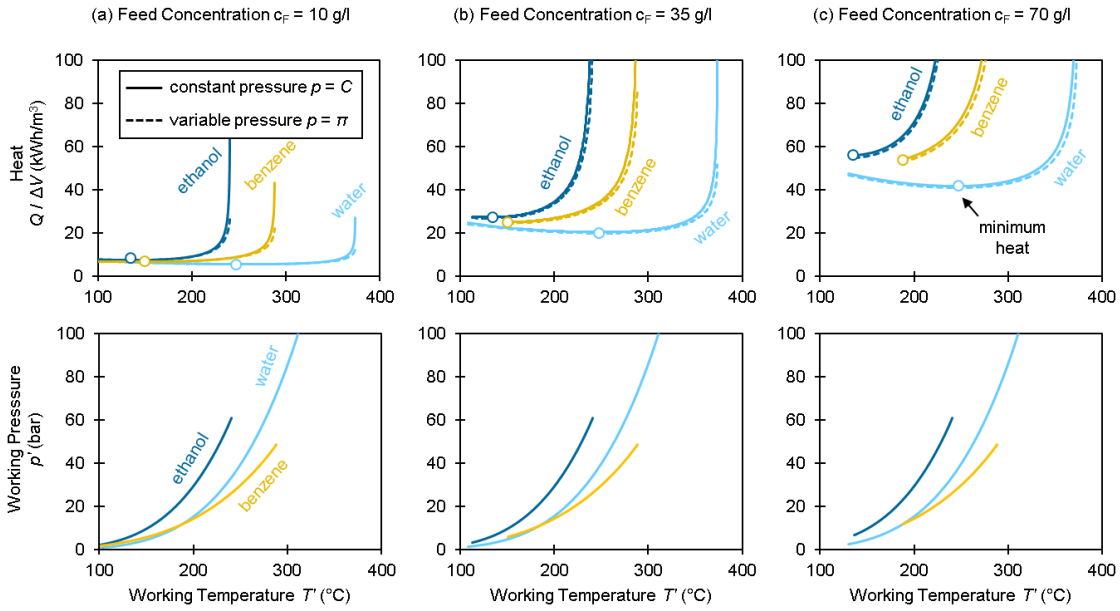

Figure 3.11 Heat of TDRO for a selection of different saturated working fluids including water, ethanol, and benzene at different working temperatures and pressures. Results are shown for recovery ratio r = 0.5 and for different feed sources including (a) brackish water with concentration c_F = 10 g/l, (b) seawater at c_F = 35 g/l, and (c) produced water at c_F = 70 g/l. Results are compared for operation with constant applied pressure $p = C$ (i.e. irreversible process) and with a variable pressure that is equal to the osmotic pressure $p = \pi$ (i.e. reversible process).

3.3.3 Comparing TDRO Performance to Other Desalination and Water Purification Systems

The performance of TDRO can be evaluated along several metrics in order to compare it with other desalination and water purification technologies. Figure 3.12 shows the performance of TDRO when water is selected as the working fluid. Performance is shown here as a function of the working fluid temperature, which can be controlled by the sizing ratio, as described in detail above. Clearly the energy required to drive TDRO is greater than for conventional RO. As an example, for desalination of seawater with c_F = 35 g/l and a recovery ratio r = 0.5, the minimum heat is obtained when $T' = T^* = 247$ °C and at this point, specific heat input $Q/\Delta V$ = 20.5 kWh/m^3 for TDRO with an irreversible load and 20.0 kWh/m^3 with a reversible load. By comparison the work associated with the RO load is only W = 1.6 kWh/m^3 for irreversible RO and 1.1 kWh/m^3 for reversible RO. This translates to a first law efficiency of η_I = 7.9% for the irreversible case, and 5.6% for the reversible case. Or in other words, at least 12× more energy is needed for TDRO than RO. The inherent energy efficiency of RO is not surprising. Importantly, for TDRO the energy required is in the form of heat, which is often cheap, plentiful, and available from renewable sources, while for RO, energy is required in the form of work, usually electricity. Therefore, low thermal efficiency does not necessarily rule out the role that thermal separation has in certain applications. It is important to consider TDRO performance with respect to other thermally driven technologies.

The efficiency with which TDRO uses heat can be expressed with the second law efficiency as shown in Figure 3.12. For the same case of seawater desalination with c_F = 35 g/l and recovery ratio r = 0.5, TDRO operated at the best working temperature of T' =

T^* = 247 °C, will achieve a second law efficiency of η_{II} = 18.1% for irreversible and 12.9% for reversible. Second law efficiency is shown to improve at lower working temperatures approaching 30% at 100 °C, mainly due to the drop in Carnot efficiency at such low temperatures. Fundamentally, the second law efficiency of TDRO is limited by the need to supply internal energy of the working fluid. As such, second law efficiency of TDRO will necessarily be less than unity. By comparison, most other thermal separation technologies heat feed solution directly and can, in theory, approach second law efficiency of 100 %. This is never realized in practice however, as such would require an infinite number of stages with infinitely large heat exchangers. For example, for seawater desalination with multi-effect distillation and multi-stage flash distillation, second law efficiencies from 5–10 % are more typical [135]. Alternatively, the concept of using an organic Rankine cycle, or some other heat engine, to convert heat to work for RO has been proposed throughout the literature and second law efficiencies from 6–40 % have been reported, but the higher values are for heat engine schemes with multigeneration systems, which can be complex and costly [136], [137], [138], [139], [140]. In contrast, the TDRO piston system is simple, compact, and can integrate effective thermal management with relative ease. This should enable high thermodynamic efficiencies to translate better into practice for TDRO, particularly at lower operating temperatures, although further analysis is needed to confirm. For example, at 100 °C, the second law efficiency of TDRO approaches 30%, demonstrating a promising technology for energy-efficient seawater desalination.

The efficiency with which TDRO uses heat can also be expressed in terms of the gain output ratio, also shown in Figure 3.12. For seawater desalination with c_F = 35 g/l and

recovery ratio $r = 0.5$, a maximum gain output ratio $GOR = 32.5$ is achieved for irreversible TDRO and $GOR = 33.3$ for reversible. This compares favorably with other thermal desalination technologies, where gain output ratios range from 5-10 for multi-stage flash distillation, and from 10-15 for multi-effect distillation for seawater desalination with steam around 100 °C [111], [135], [141], [142], [143], [144], [145]. This *GOR* range includes both experimental and modelling results, and reflects the practical economic limitation that these distillation processes encounter when increasing the number of stages to improve efficiency becomes cost prohibitive beyond a certain point. Of course, TDRO performance will also be affected by practical limitations but further analysis of TDRO heat transfer kinetics is needed to properly evaluate these. Encouragingly, even at lower working temperatures approaching 100 °C, which will favor efficient heat transfer kinetics, the gain output ratio of TDRO remains around $GOR \sim 28$ (for seawater desalination with $c_F = 35$ g/l and recovery ratio $r = 0.5$), which is greater than other thermal separation processes. Also of note, a maximum $GOR = 49$ for TDRO when recovery ratio $r = 0$, was reported in Godart's pioneering work [130,131], however his work did not consider the possibility of optimizing the sizing ratio to improve performance. Though not shown in Figure 3.12, our analysis indicates that for a recovery ratio of $r = 0$, the gain output ratio in fact exceeds $GOR = 66$ when the sizing ratio is optimized. Additional analysis of TDRO performance is provided in Supplementary Note 3.3, including plots for the maximum theoretical GOR, and for the first and second law efficiencies taken with respect to the minimum reversible RO load.

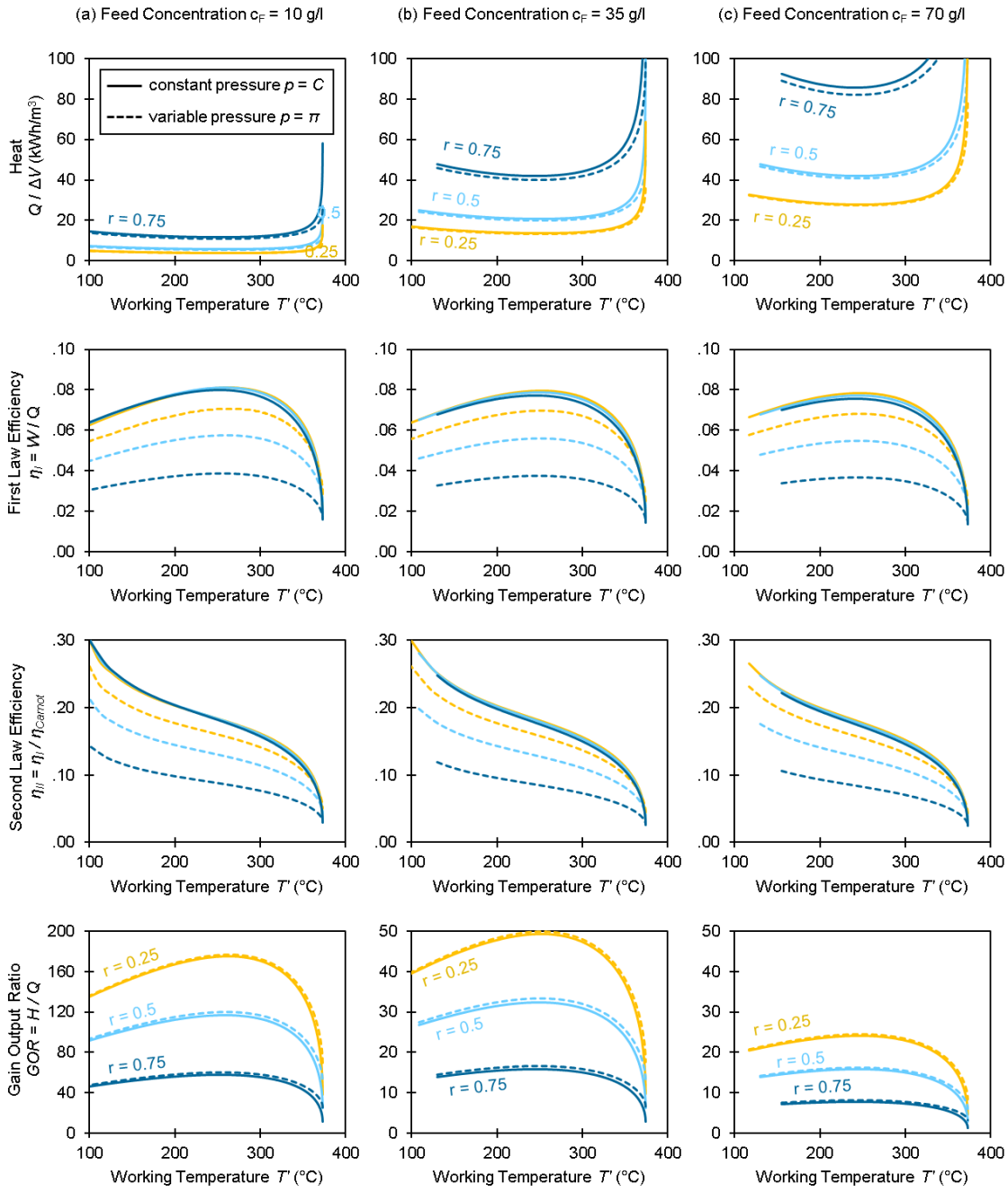

Figure 3.12 Performance of TDRO as a function of the working fluid temperature, which in this case is selected as saturated water. Results are shown for different recovery ratios r and different feed sources including (a) brackish water with concentration c_F = 10 g/l, (b) seawater at c_F = 35 g/l, and (c) produced water at c_F = 70 g/l. Results are compared for operation with constant applied pressure $p = C$ (i.e. irreversible process) and with a variable pressure that is equal to the osmotic pressure $p = \pi$ (i.e. reversible process).

3.4 Conclusion

In this study we analyze the thermodynamic limits of a novel thermal separation concept called thermally driven reverse osmosis (TDRO). The system consists of a piston set that uses the thermal expansion of a saturated working fluid to act on an impaired feed water source to drive clean water permeate across a RO membrane. The concept was first introduced by Godart in 2021 [130], [131] but several design omissions meant that the technology's potential was somewhat understated. In particular, the relative size of the working piston and feed piston was not optimized, and yet this has an important impact on the performance of TDRO. These gaps are thoroughly addressed in this study.

To establish the relations for the specific work and specific heat input of TDRO, we apply the first law of thermodynamics. Expressions for specific work are consistent with the RO literature [133]. Expressions for specific heat input are novel, and provide several important insights into the operation and performance of TDRO. Specific heat input is shown to be a function of the desired recovery ratio, the concentration of the feed source, and a dimensionless factor that we refer to as K. Notably, while the specific heat input does increase at higher and higher recovery ratios and feed concentrations, it can be minimized by adjusting the dimensionless K factor. This K factor describes the change in internal energy that is associated with heating the working fluid, and it is shown to be highly sensitive to the relative sizes of the working piston and feed piston. By carefully sizing the pistons, the change in the specific internal energy and hence the specific heat input of TDRO can be minimized. In addition, the dimensionless K factor (and hence the specific heat input) is affected by the choice of working fluid and its properties, and to a

lesser extent by operating at the RO load either a fixed applied pressure (irreversible) or a variable applied pressure (reversible).

By analyzing a number of cases, we show that water can serve as a good working fluid, achieving lower specific heat input than alternatives like benzene or ethanol, and allowing for operation at low grade temperatures. Moreover, water is common and non-toxic. Also, we show that it is preferable to operate the RO load at a fixed applied pressure, as opposed to gradually increasing pressure such as in a reversible process. Throughout the RO literature, the possibility of operating RO in a reversible way has been shown to yield significant theoretical savings, but in this case, the change in specific work makes only a small difference to the specific heat input, and therefore the added complexity of operating in a slow reversible manner is not justified. Finally, we show that a sizing ratio of approximately 0.5 is recommended as a rule of thumb (i.e. working piston area = 2× feed piston area). Although this sizing ratio could ideally be adjusted and optimized for all different feed concentrations and recovery ratios, such a recommended sizing ratio yields near optimal performance across a range of common conditions.

Applying these design recommendations to the case of seawater desalination with recovery of 50% feed, we conclude that a properly designed TDRO system can achieve specific heat input as low as 20 kWh/m^3, first law efficiency of 7.9%, second law efficiency of 18.1%, and a gain output ratio of 33. This performance is achieved at reasonable working pressure and temperature less than 40 bar and 250 °C. Lower pressure and temperature can also be accommodated with some minor sacrifices to performance. These performance metrics exceed the initial claims of Godart [130], [131],

and compare well against competing desalination and separation technologies, especially thermal systems such as multi-effect distillation, multi-stage flash distillation, membrane distillation.

These encouraging results suggest that further research and development is justified for TDRO. Several important questions should be considered in future study. For example, the piston sizing ratio will affect not only energy efficiency, as focused on here, but also other dynamics such as the operating pressure and temperature of the working fluid. These will have important implications for the mechanical loading placed on the piston, the possibility of using low temperature heat sources, thermal kinetics of the process, and the size and cost of the physical TDRO device. For example, a sizing ratio of less than 1, such as recommended here, will require the working piston to be either relatively large and/or to cycle more quickly in order to achieve a certain water production rate. Whether heat can be transferred to and from the working fluid at rates sufficient to support such cycling will depend on the desired working temperature, the temperature of the heat source, the heat exchanger systems, and other factors. The relationship between the temperatures of the working fluid, source, and sink, will also affect the process efficiency, as the difference between the operating temperature and the environment will determine the rates of heat loss. Such dynamics should be considered in future work with a thorough investigation of TDRO kinetics. In addition, TDRO will share some of the disadvantages of RO as compared to thermal distillation, such as lower selectivity, and difficulty handling highly concentrated feeds or achieving high recovery ratios. Therefore, while the thermodynamics of TDRO are promising, further analysis is

needed to determine whether TDRO can play an important role in contributing to a more sustainable water future for the world.

3.5 Supplementary Note

3.5.1 Supplementary Note 3.1: Specific Work of Reversible RO

In a reversible RO process, applied pressure is equal to the osmotic pressure and adjusted dynamically as water permeate is recovered and the feed volume becomes increasingly concentrated. The work associated with this process can therefore be obtained from equation (S3.1) by setting applied pressure equal to osmotic pressure $p = \pi$ as in equation (S3.2), and substituting the expression for osmotic pressure as in equation (S3.3).

$$W = \int p \, dV \tag{S3.1}$$

$$W_{p=\pi} = \int \pi \, dV \tag{S3.2}$$

$$W_{p=\pi} = \int_0^{\Delta V} \pi_F \left(\frac{V_F}{V_F - \Delta V}\right) d\Delta V \tag{S3.3}$$

Given than π_F (initial osmotic pressure of the feed solution) and V_F (initial volume of the feed solution) are constants, it can be shown by substitution (letting $x = V_F - \Delta V$ and $dx = -d\Delta V$) that the integral is of the form shown in equation (S3.4). This can be easily solved to obtain the result shown in equation (3.4b).

$$W_{p=\pi} = -\pi_F \, V_F \int_{x_1}^{x_2} \frac{dx}{x} \tag{S3.4}$$

$$W_{p=\pi} = -\pi_F \, V_F \, ln(x)|_{x_1}^{x_2} \tag{S3.5}$$

$$W_{p=\pi} = -\pi_F V_F \, ln(V_F - \Delta V)|_0^{\Delta V} \quad \text{S3.6}$$

$$W_{p=\pi} = -\pi_F V_F \, ln\left(\frac{V_F - \Delta V}{V_F}\right) \quad \text{S3.7}$$

$$W_{p=\pi} = \pi_F V_F \, ln\left(\frac{V_F}{V_F - \Delta V}\right) \quad \text{S3.4b}$$

Finally, the specific work can be written by normalizing per unit volume of recovered permeate to obtain equation (3.4c).

$$W = \int p \, dV \quad \text{S3.4c}$$

3.5.2 Supplementary Note 3.2: Additional Schematics for Thermally Driven Reverse Osmosis

Figures S3.1 and S3.2 illustrate the complete TDRO cycle. The cycle begins at stage 1, where the feed piston contains seawater (or some other impaired water source) at atmospheric pressure, and the working piston contains a working fluid at some temperature above or equal to ambient. From stage 1 to 2, heat is supplied to the working fluid, causing pressure to increase. Initially, there is no change in volume, and then, only once pressure exceeds the osmotic pressure of the feed solution, the working fluid begins to expand, moving the cycle from stage 2 to 3. As previously explained in detail, this expansion can be done either reversibly (with applied pressure only infinitesimally greater than the osmotic pressure) or irreversibly (with constant applied pressure well above osmotic pressure). Figure S3.2 illustrates the case for reversible expansion. Once equilibrium is established at the desired recovery ratio, the heat source is removed and the feed chamber is opened to atmosphere, releasing high pressure brine which is replaced with feed. Finally, from stage 4 to 1, the pistons are reset by removing heat from the working fluid, causing its volume to reduce and the feed piston to draw in fresh feed

water. One important condition to enable the completion of this cycle is that the initial pressure of working fluid must occur at some temperature above or equal to ambient temperature (which is ensured by the limits we have imposed on the sizing ratio).

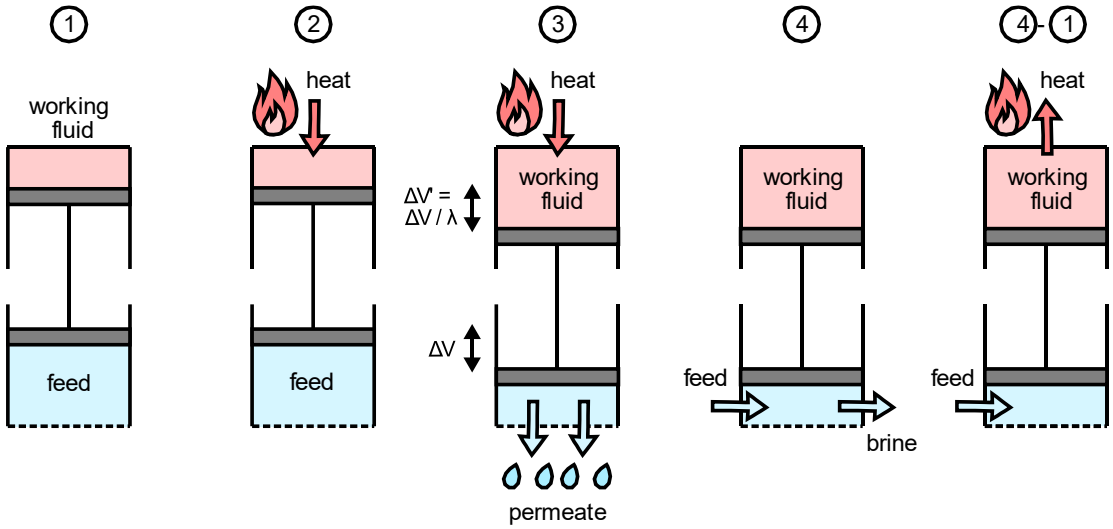

Figure S3.1 TDRO cycle.

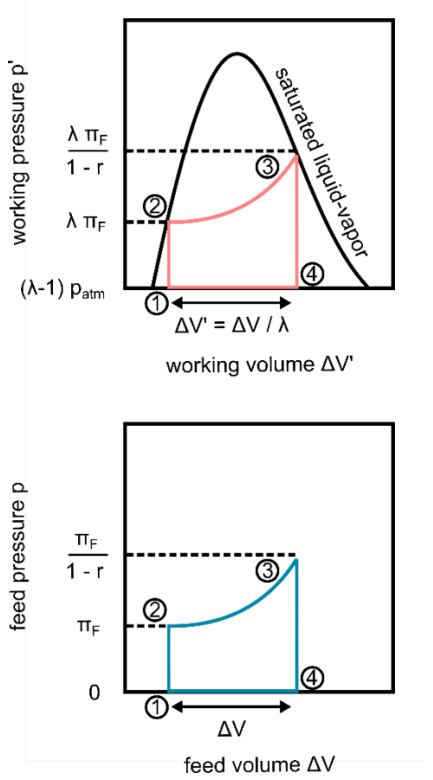

Figure S3.2 Pressure versus volume schematics for working fluid and feed solution throughout the TDRO cycle.

3.5.3 Supplementary Note 3.3: Additional Performance Results

An alternative method of defining the first and second law efficiencies involves selecting a different reference for work. The revised formulations are as follows:

$$W_{p=\pi} = -\pi_F \, V_F \int_{x_1}^{x_2} \frac{dx}{x} \tag{3.11}$$

$$W_{p=\pi} = -\pi_F \, V_F \, ln(x)|_{x_1}^{x_2} \tag{S3.11}$$

$$W_{p=\pi} = -\pi_F \, V_F \, ln(V_F - \Delta V)|_0^{\Delta V} \tag{3.12}$$

$$W_{p=\pi} = -\pi_F \, V_F \, ln\left(\frac{V_F - \Delta V}{V_F}\right) \tag{S3.12}$$

The implication here is that thermal energy input can be compared with respect to the useful work (which is the reversible RO load) rather than the actual work (the irreversible RO load). The advantage of such a definition is that the plots for first and second law efficiencies will now accurately reflect the fact that expanding the RO load in a reversible manner slightly lowers the heat as compared to irreversible expansion. This is illustrated in Figure S3.3, which shows that with these new definitions for efficiency, the first and second law efficiencies are better for the reversible RO load than for the irreversible one. In contrast, the plots shown previously in Figure 3.12 can be easy to misinterpret because they show better first and second law efficiencies for the irreversible RO load, but this is simply an artifact of the inflated work.

Another useful measure of TDRO performance is to compare *GOR* to the maximum theoretical *GOR* that could be obtained if the minimum reversible RO load were handled by a thermal process at Carnot efficiency. This maximum gain output ratio GOR_{max} is defined in equation (S3.13) and plotted in Figure S3.3. As shown, GOR_{max} scales with

temperature, as Carnot efficiency improves at higher temperatures. Also, GOR_{max} increases at lower feed concentrations and recovery ratios, as these have lower RO loads associated with them. Ultimately, the comparison of GOR to GOR_{max} provides another way of observing TDRO's second law efficiency.

$$GOR_{max} = \frac{\Delta H}{Q_{min}} = \frac{\Delta H}{W(p = \pi)/\eta_{Carnot}} \qquad \text{S3.13}$$

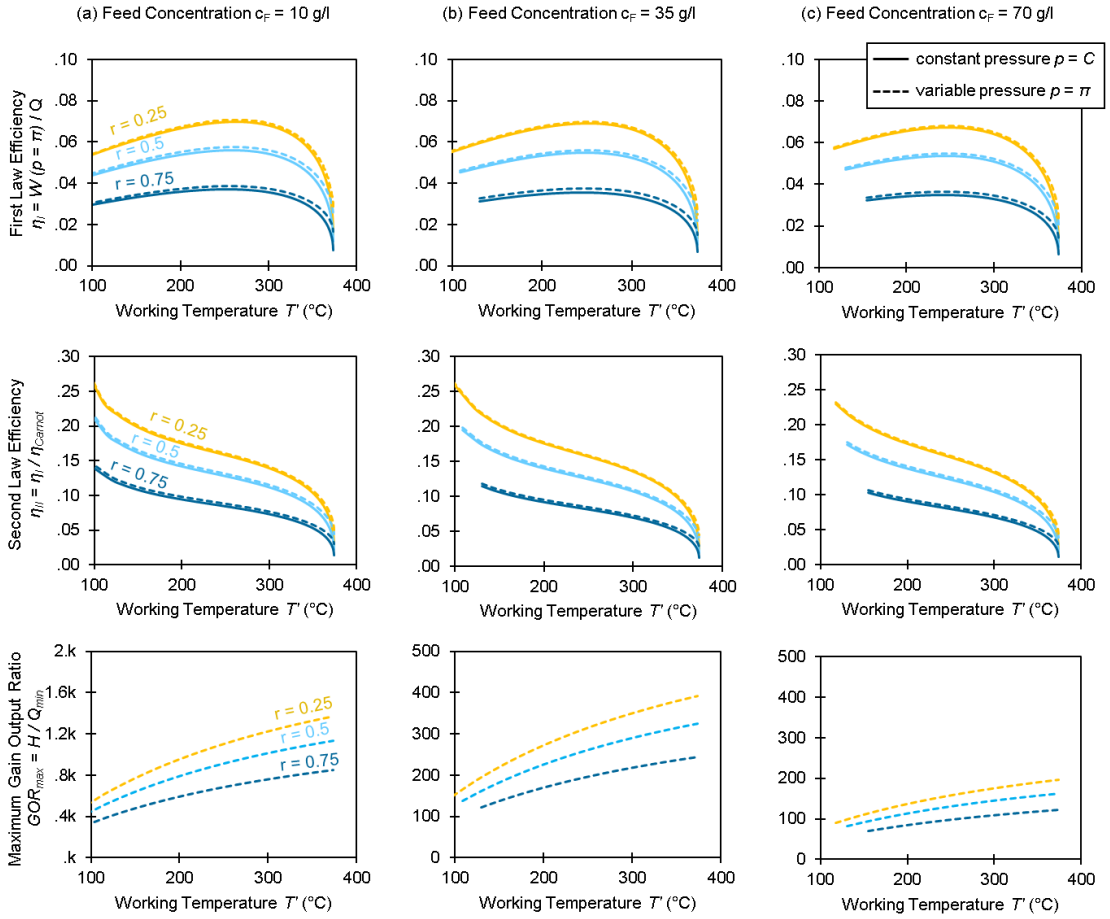

Figure S3.3 Performance of TDRO. First and second law efficiencies are evaluated with respect to the minimum work needed for a reversible RO load, as defined in equations (S3.11) and (S3.12). Maximum gain output ratio is defined in equation (S3.13).

CHAPTER FOUR

USING NATURAL OCEAN THERMAL GRADIENTS TO DRIVE MEMBRANE DISTILLATION: A RENEWABLE DESALINATION SOLUTION FOR REMOTE ISLAND COMMUNITIES

4.1 Introduction

Water management is an important and sensitive issue for island communities. Freshwater is often scarce, typically limited to rainfall or shallow freshwater lenses that form above denser seawater. Careful management is essential to prevent seawater intrusion, which can occur due to over-pumping or deep drilling and may render vital groundwater supplies brackish and unusable [146]. For these reasons, seawater desalination is increasingly considered a necessity in such locations [147], [148], [149], [150]. Desalination refers to any engineered process that separates clean water from salt and other impurities. This is often done by a process known as reverse osmosis (RO) but many alternatives also exist [151], [152]. While desalination technology is mature and engineering know-how is well developed, separating water from salt remains energy intensive and costly. These represent important hurdles for remote island communities that often suffer from a lack of adequate funding for infrastructure and that rely on expensive and polluting diesel fuel for electric power [153], [154].

In an effort to improve access to water for remote islands it is important to consider the availability of local and renewable resources that can be leveraged. One such resource for many islands is the vast stores of thermal energy in the surrounding ocean, and the large thermal gradients that form between warm surface water and the cool deep sea [155], [156]. Figure 4.1(a) shows a map of major US island populations, including

Hawaii, Puerto Rico, Guam, the Marshall Islands, American Samoa, and others. As shown, these island locations have high surface temperatures, reaching around 30 °C. At the same time, temperatures between 8 and 5 °C are accessible at depths ranging from 500 to 1000 meters. Figure 4.1(b) illustrates the thermocline at a sample location off the coast of American Samoa. The temperature profile from three stations within a radius of approximately two miles from American Samoa are plotted. As depicted, temperature decreases sharply with depths up to 500 m, followed by a more gradual decline beyond that depth.

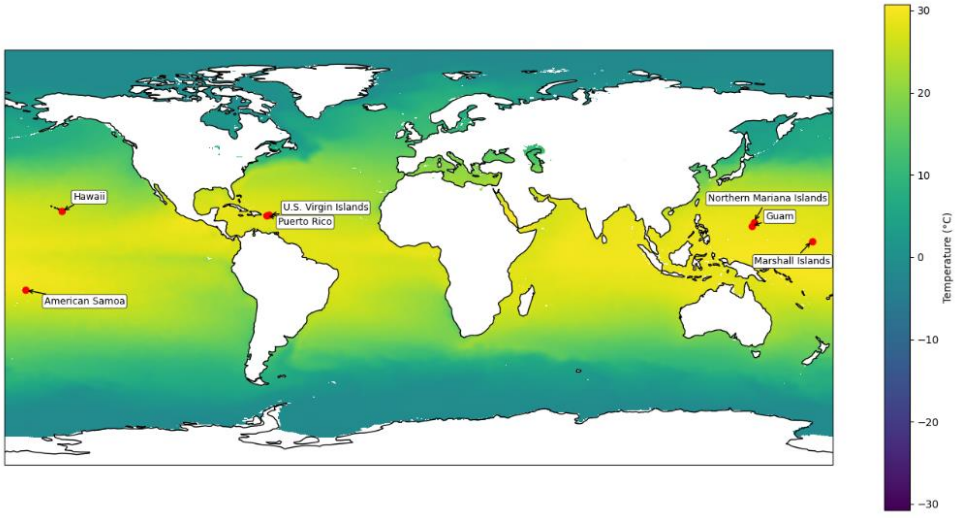

(a)

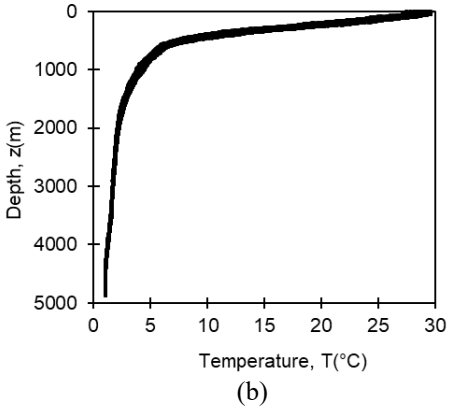

(b)

Figure 4.1 (a) Surface ocean temperatures around the world (b) Thermocline profile (American Samoa)[157]

For many years, the prospect of harnessing energy from ocean thermal gradients has attracted interest. In literature, the famous Captain Nemo in Jules Vernes' "Twenty Thousand Leagues Under the Seas" famously stated "by establishing a circuit between two wires immersed to different depths, I'd be able to obtain electricity through the diverging temperatures they experience" [158]. Apparently inspired by the idea [159], French scientist Jacques-Arsène d'Arsonval is credited with the first laboratory demonstration of electricity generation from ocean thermal gradients in 1881. Some years later in 1930, his student Georges Claude helped to build the first ocean thermal power plant in Cuba [159]. Since then other prototypes have been built in Hawaii, Japan, France, and other locations [160], [161], [162]. Until now, however, these efforts have been met with only limited success.

For the most part, the focus of these efforts has been on the production of electricity using various heat engine cycles [163], [164], [165], [166]. The challenge with this is that at such low temperature differences, heat engine efficiencies are low. This leads to systems that are oversized and capital intensive, and that must handle tremendous volumes of warm and cold seawater in order to achieve desired power capacities. Until now, the possibility of using ocean thermal gradients to produce water has received much less attention in the literature. Some open cycle heat engines do happen to produce some water as a by-product to electricity, but these open cycle heat engines are even less efficient than closed cycle systems. Electricity can of course be used to produce clean water, such as by RO, but if the primary goal of harnessing ocean thermal energy is to produce freshwater, it can be more efficient to consider the possibility of thermal gradients directly to drive desalination, without intermediate power generation.

For this reason, we propose the concept of ocean thermal membrane distillation (OTMD), which uses the natural temperature gradient between warm surface seawater and cold deep ocean water to drive desalination. Figure 4.2 illustrates the concept. At the heart of the system is a porous hydrophobic membrane across which warm seawater feed and cool distillate are brought into contact. The thermally induced vapor pressure difference between the two fluids drives vapor transfer from the seawater to condense on the distillate, thereby expanding the volume of clean freshwater. Heat received across the membrane is then transferred to a cold deep ocean coolant, and the distillate is then recirculated in a continuous operation.

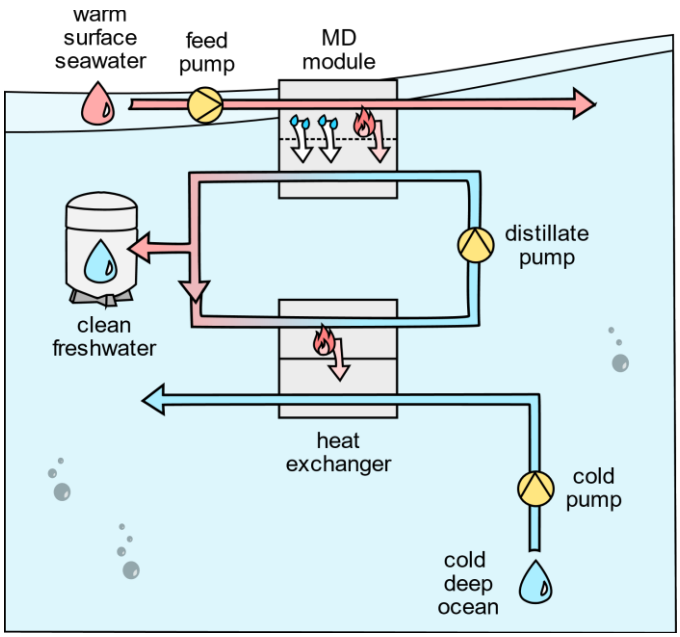

Figure 4.2 Ocean thermal membrane distillation (OTMD). Cold water from the deep sea is used to cool a circulating distillate fluid. The cool distillate draws water vapor out of a warm seawater source and across a membrane, thereby producing pure freshwater.

Membrane distillation (MD) itself is not a new technology and has an extensive body of literature. Many applications have been studied, such as seawater and brackish water

desalination, treatment of produced water from oil and gas [167], of wastewater from textiles [168], and others [169]. Also, integrations with many thermal sources has been considered, including solar [170], geothermal [171], waste heat [172] and a large number of MD configurations have been proposed.

The simplest configuration is known as direct contact MD, in which feed and distillate directly contact the membrane [51], [173], [174], but many alternatives exist, including configurations with an integrated air gap [175], [176], with an air gap under vacuum [177], [178], with a circulating sweep gas [179], [180], or with no membrane at all [181], [182]. Nevertheless, despite this extensive body of literature, until now the concept of OTMD has only been investigated by one other publication, namely by Baghbanzdeh et al [183]. In their work, they introduce the possibility of using ocean thermal gradients to drive MD and undertake a technoeconomic analysis of the concept, specifically for application to a region in Gulf of Oman close to the Strait of Hormuz, Iran.

Encouragingly, they conclude that the zero input thermal membrane distillation process can produce freshwater at a low cost of \$0.28/m³ with a specific energy consumption of just 0.45 kWh/m³. One important omission from this work, however, is analysis of the pump work that is required to access cold deep ocean water to serve as a heat sink. In fact, this is perhaps the most fundamental question about the technical merit of OTMD. Only if the pumping load is less than the alternative of simply powering RO can OTMD be justified. This is in contrast to other MD applications, where energy efficiency is evaluated in terms of thermal performance (such as the ratio of heating to water production). But in this case, since the heat source and sink are nearly infinite, the

critical measure of efficiency is how much work (pump power) is needed to bring hot and cold water to the OTMD system.

Therefore, the goal of this study is to evaluate the pump work requirements of OTMD and determine whether these are less than the work requirements of RO. In particular, we consider the case of using data from the thermocline near American Samoa. This chapter is organized as follows. First, we define the operating conditions of the OTMD system based on realistic ocean thermal gradients observed in U.S. Island locations, such as surface seawater at 30 °C and deep ocean water temperatures ranging from 5 to 20 °C. Second, we conduct experimental testing using a laboratory-scale direct contact membrane distillation (DCMD) setup to evaluate water flux and specific energy consumption under these conditions. Third, we develop theoretical models to estimate thermal and pumping loads for different deep seawater intake configurations and assess three design options for their mechanical and energy feasibility. Finally, we discuss the implications for remote island communities by applying the OTMD framework to a case study of Aunu'u Island in American Samoa, highlighting how this approach could support sustainable energy-water infrastructure development with lower energy demands compared to conventional reverse osmosis systems.

4.2 Theory

4.2.1 Water Production by OTMD

Equations (4.1a) and (4.1b) denote mass balances across the membrane distillation (MD) module. Equation (4.1a) shows the mass loss from the feed side, where $\Delta\dot{m}$ is the rate of mass transfer through the membrane, defined as the difference between the feed inlet and outlet mass flow rates. Similarly, Equation (4.1b) describes the mass gain on the

distillate side, where $\Delta\dot{m}$ is the increase in mass flow rate from the distillate inlet to outlet.

In addition, Equation (4.1c) describes the mechanism by which vapor transfer in MD is driven with vapor pressure difference between feed and distillate sides ($p_{H2O,F}$ - $p_{H2O,D}$) along with membrane mass transfer coefficient K and surface area *a*.

$$\Delta\dot{m} = \dot{m}_{F,in} - \dot{m}_{F,out} \quad 4.1a$$

$$\Delta\dot{m} = \dot{m}_{D,out} - \dot{m}_{D,in} \quad 4.1b$$

$$\Delta\dot{m} = a\,K\left(p_{H2O,F} - p_{H2O,D}\right) \quad 4.1c$$

The relationship between the vapor pressure $p_{H2O,}$ temperature T, and concentration c of the feed solution is described by Kohler equation (4.2), the Antoine equation (4.3), and the Van't Hoff equation (4). Equation (2) shows the vapor pressure of water in a saline solution:

$$p_{H2O} = p_o \exp\left(\frac{v}{R\,T}(p - \pi)\right) \quad 4.2$$

Here, p_o is the vapor pressure of pure water, v is the molar volume of water, R is universal gas constant, T is absolute temperature, p is applied pressure and π is the osmotic pressure of the solution. This equation shows how vapor pressure is affected by both applied pressure and solute concentration. When p=0 (gauge pressure) and π=0 (pure water), the exponential term becomes 1, so p_{H2O}= p_o.

Equation (4.3) shows the vapor pressure of pure water p_o as a function of temperature using the Antoine equation:

$$p_o = \exp\left(A_o - \frac{B_o}{C_o + T}\right) \quad 4.3$$

This empirical equation shows the exponential increase in vapor pressure with temperature and is widely used for calculating vapor pressure of a pure substance like water. A_0, B_0, and C_0 are constants which can be found in [184].

The osmotic pressure of a saline solution can be calculated using Van't Hoff equation:

$$\pi = i\,R\,T\,c \tag{4.4}$$

Where i is Van't Hoff factor, R is the gas constant, T is temperature and c are the concertation of the solution.

As shown in Figure 4.3(a) vapor pressure increases exponentially with temperature for both the feed and distillate streams. This trend is essential for membrane distillation, as the vapor pressure difference across the membrane drives water transport. Figure 4.3(b) indicates the ocean temperature profile with depth, where there is a steep thermal gradient in the upper layers and a stable cold temperature (~4°C) at depths around 1000 meters, which provides a reliable low-temperature source for OTMD. Figure 4.3(c) shows the water flux as a function of distillate temperature for different membrane permeability coefficients (K), indicating that higher distillate temperatures reduce the vapor pressure difference across the membrane, thereby lowering flux, while higher permeability membranes significantly enhance water production under the same conditions.

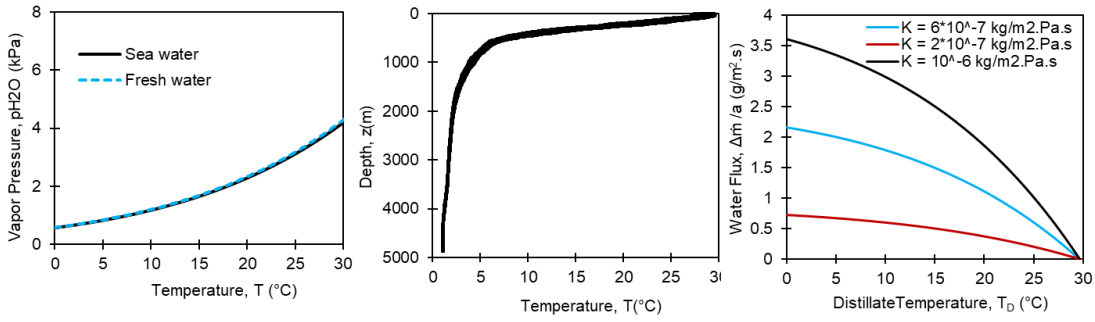

(a) (b) (c)

Figure 4.3 (a) Vapor pressure of seawater (c = 35 g/l) and freshwater (c = 0g/l) as a function of temperature. (b) a sample thermocline off the coast of American Samoa [185]. (c) Vapor flux as a function of distillate temperature assuming a feed temperature of T_F = 30 °C and various mass transfer coefficients [186], that are representative of common membrane vapor permeabilities.

Of course, the actual vapor pressure difference across the membrane is lower than the difference between the bulk feed and distillate streams due to effects such as temperature polarization, concentration polarization, axial variations along the membrane length, and heat transfer to the surroundings. These phenomena can be accounted for using finite element transport models; however, this lies beyond the scope of the present study.

4.2.2 Cooling Load of OTMD

To drive the OTMD system, it is necessary to maintain a temperature difference between the warm feed, which flows through the MD unit, and the recirculated cool distillate. As these streams come into contact, the cool distillate absorbs heat. This heat must then be removed by transferring it to cold deep seawater. The thermal load to be extracted by the deep seawater can be determined by performing an energy balance across both the MD unit and the heat exchanger. To help with this analysis, Figure 4.4 shows the mass and energy balance of the OTMD system.

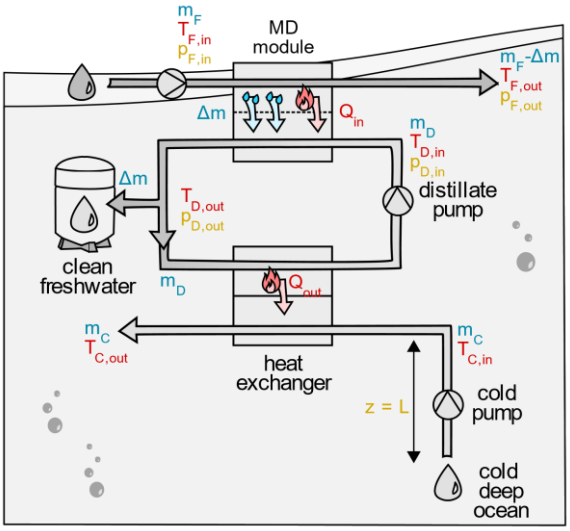

Figure 4.4 Schematic overview of the energy and mass transfer processes in the OTMD system

Equation (4.5a) describes the energy balance of incoming feed through the membrane module. As shown, the change in energy will be a function of the input thermal energy $\dot{Q}_{in}$ together with the mass transfer $\Delta\dot{m}$ and its associated enthalpy $\dot{H}$.

$$\Delta\dot{E}_F = \dot{E}_{F,in} - \dot{E}_{F,out} \tag{4.5a}$$

$$\Delta\dot{E}_F = \dot{m}_F\, e_{F,in} - (\dot{m}_F - \Delta\dot{m})\, e_{F,out} \tag{4.5b}$$

$$\Delta\dot{E}_F = \dot{m}_F\, h_{F,in} - (\dot{m}_F - \Delta\dot{m})\, h_{F,out} \tag{4.5c}$$

$$\Delta\dot{E}_F = \dot{Q}_{in} + \dot{H} \tag{4.5d}$$

$$\Delta\dot{E}_F = \dot{Q}_{in} + \int_0^{\Delta\dot{m}} h\, d\dot{m} \tag{4.5e}$$

$$\Delta\dot{E}_F \approx \dot{Q}_{in} + h_{F,out}\, \Delta\dot{m} \tag{4.5f}$$

$$\dot{m}_F\, h_{F,in} - (\dot{m}_F - \Delta\dot{m})\, h_{F,out} \approx \dot{Q}_{in} + h_{F,out}\, \Delta\dot{m} \tag{4.5g}$$

$$\dot{Q}_{in} \approx \dot{m}_F\, h_{F,in} - \dot{m}_F\, h_{F,out} \tag{4.5h}$$

$$\dot{Q}_{in} \approx \dot{m}_F\, cp\, (T_{F,in} - T_{F,out}) \tag{4.5i}$$

Similar to the feed side, the energy balance on the distillate side is described by equation (4.6) which is the energy balance of incoming distillate through the membrane module. As shown, the change in energy will be a function of the input thermal energy $\dot{Q}_{in}$ together with the mass transfer $\Delta\dot{m}$ and its associated enthalpy $\dot{H}$.

$$\Delta\dot{E}_D = \dot{E}_{D,out} - \dot{E}_{D,in} \quad 4.6a$$

$$\Delta\dot{E}_D = (\dot{m}_D + \Delta\dot{m})\, e_{D,out} - \dot{m}_D\, e_{D,in} \quad 4.6b$$

$$\Delta\dot{E}_D = (\dot{m}_D + \Delta\dot{m})\, h_{D,out} - \dot{m}_D\, h_{D,in} \quad 4.6c$$

$$\Delta\dot{E}_D = \dot{Q}_{in} + \dot{H} \quad 4.6d$$

$$\Delta\dot{E}_D = \dot{Q}_{in} + \int_0^{\Delta\dot{m}} h\, d\dot{m} \quad 4.6e$$

$$\Delta\dot{E}_D \approx \dot{Q}_{in} + h_{D,out}\, \Delta\dot{m} \quad 4.6f$$

$$(\dot{m}_D + \Delta\dot{m})\, h_{D,out} - \dot{m}_D\, h_{D,in} \approx \dot{Q}_{in} + h_{D,out}\, \Delta\dot{m} \quad 4.6g$$

$$\dot{Q}_{in} \approx \dot{m}_D\, h_{D,out} - \dot{m}_D\, h_{D,in} \quad 4.6h$$

$$\dot{Q}_{in} \approx \dot{m}_D\, cp\, (T_{D,out} - T_{D,in}) \quad 4.6i$$

The energy balance for the distillate stream passing through the heat exchanger is described by equation (4.7). As shown, the energy gained by distillate is equivalent to the heat transferred into this stream which is shown by $\dot{Q}_{in}$.

$$\Delta\dot{E}_D = \dot{E}_{D,out} - \dot{E}_{D,in} \quad 4.7a$$

$$\Delta\dot{E}_D = \dot{m}_D\, e_{D,out} - \dot{m}_D\, e_{D,in} \quad 4.7b$$

$$\Delta\dot{E}_D = \dot{m}_D\, h_{D,out} - \dot{m}_D\, h_{D,in} \quad 4.7c$$

$$\Delta\dot{E}_D = \dot{Q}_{out} \quad 4.7d$$

$$\dot{Q}_{out} = \dot{m}_D\, h_{D,out} - \dot{m}_D\, h_{D,in} \quad (4.7e)$$

$$\dot{Q}_{out} = \dot{m}_D\, cp\, (T_{D,out} - T_{D,in}) \quad (4.7f)$$

As shown in equation (4.8), a similar approach can be considered for the cold deep ocean water, where the inlet stream of the cold deep ocean receives the $\dot{Q}_{out}$ from distillate stream and cool it down.

$$\Delta\dot{E}_C = \dot{E}_{C,out} - \dot{E}_{C,in} \quad (4.8a)$$

$$\Delta\dot{E}_C = \dot{m}_C\, e_{C,out} - \dot{m}_C\, e_{C,in} \quad (4.8b)$$

$$\Delta\dot{E}_C = \dot{m}_C\, h_{C,out} - \dot{m}_C\, h_{C,in} \quad (4.8c)$$

$$\Delta\dot{E}_C = \dot{Q}_{out} \quad (4.8d)$$

$$\dot{Q}_{out} = \dot{m}_C\, cp\, (T_{C,out} - T_{C,in}) \quad (4.8e)$$

Therefore, we can conclude that the heating load for OTMD can be determined using the energy balance of the distillate stream, the feed stream, or the cold water stream.

$$\dot{Q}_{load} = \dot{Q}_{in} = \dot{Q}_{out} \quad (4.9a)$$

$$\dot{Q}_{load} = \dot{m}_F\, cp\, (T_{F,in} - T_{F,out}) \quad (4.9b)$$

$$\dot{Q}_{load} = \dot{m}_D\, cp\, (T_{D,out} - T_{D,in}) \quad (4.9c)$$

$$\dot{Q}_{load} = \dot{m}_C\, cp\, (T_{C,out} - T_{C,in}) \quad (4.9d)$$

This cooling load should be minimized not because of any intrinsic goal to minimize thermal energy, because in this case thermal energy is readily available from an abundant ocean source, but because more thermal load means more cold water must be pumped from the deep ocean to remove the thermal load. In other words, the pumping load is directly a function of the cooling load.

To show this further, let us consider also the energy balance of the heat exchanger written in terms of effectiveness and the maximum heat transfer as in equation (4.10). In the case where the cold deep ocean flow rate is greater than the distillate circulation rate $\dot{m}_C > \dot{m}_D$, the maximum heat transfer will be limited by the distillate circulation rate, yielding equation (4.11). On the other hand, when cold deep ocean flow is less than the distillate circulation $\dot{m}_C < \dot{m}_D$, the maximum heat transfer will be limited by the cold deep ocean flwor ate, yielding equation (4.12).

$$\dot{Q}_{load} = \varepsilon \, \dot{Q}_{max} \tag{4.10}$$

$$\dot{Q}_{load} = \varepsilon \, \dot{m}_D \, cp \left(T_{D,out} - T_{C,in}\right) \text{ when } \dot{m}_C > \dot{m}_D \tag{4.11a}$$

$$\dot{Q}_{load} = \varepsilon \, \dot{m}_C \, cp \left(T_{D,out} - T_{C,in}\right) \text{ when } \dot{m}_C < \dot{m}_D \tag{4.12a}$$

Then combining with equations (4.9c) we get equations (4.11c) and (4.12c). This shows how deep we must go to get cold deep ocean water. We must get a certain $T_{C,in}$ in order to handle the thermal load of the system. These expressions for cold temperatures are helpful because they will directly determine the pumping load as they will specify how deep water must be pumped from and the necessary flow rate, either $\dot{m}_C = \dot{m}_D$ for equation (4.11c) or $\dot{m}_C$ for equation (4.12c).

$$T_{C,in} = T_{D,out} - \frac{\dot{Q}_{load}}{\varepsilon \, \dot{m}_D \, cp} \text{ when } \dot{m}_C > \dot{m}_D \tag{4.11b}$$

$$T_{C,in} = \left[T_{D,in} + \frac{\dot{Q}_{load}}{\dot{m}_D \, cp}\right] - \frac{\dot{Q}_{load}}{\varepsilon \, \dot{m}_D \, cp} \text{ when } \dot{m}_C > \dot{m}_D \tag{4.9c+4.11b}$$

$$T_{C,in} = T_{D,in} - \frac{\dot{Q}_{load}}{\dot{m}_D \, cp}\left(\frac{1}{\varepsilon} - 1\right) \text{ when } \dot{m}_C > \dot{m}_D \tag{4.11c}$$

$$T_{C,in} = T_{D,out} - \frac{\dot{Q}_{load}}{\varepsilon\, \dot{m}_C\, cp} \text{ when } \dot{m}_C < \dot{m}_D \quad 4.12b$$

$$T_{C,in} = \left[T_{D,in} + \frac{\dot{Q}_{load}}{\dot{m}_D\, cp}\right] - \frac{\dot{Q}_{load}}{\varepsilon\, \dot{m}_C\, cp} \text{ when } \dot{m}_C < \dot{m}_D \quad 4.9c+4.12b$$

$$T_{C,in} = T_{D,in} - \frac{\dot{Q}_{load}}{\dot{m}_C\, cp}\left(\frac{1}{\varepsilon} - 1\right) \text{ when } \dot{m}_C < \dot{m}_D \quad 4.12c$$

4.2.3 Pumping Load of OTMD

The pump load for OTMD includes the work required to drive the feed pump, the distillate pump, and the cold water pump, as shown in equation (4.13):

$$\dot{W}_{load} = \dot{W}_F + \dot{W}_D + \dot{W}_C \quad 4.13$$

The load for the feed pump is a function of the feed flow rate and the pressure increase across the pump. This change in pressure will account for major losses through the piping, minor losses through various fittings, and the pressure drop through the MD unit. In this study, we limit our consideration to simply the pressure drop through the MD unit as described in equation (4.14), which assumes incompressible and isentropic flow.

$$\dot{W}_F = \dot{m}_F\, v\, (p_{F,in} - p_{F,out}) \quad 4.14$$

Where v is the specific volume.

The load for the distillate pump is a function of the distillate flow rate and the pressure increase across the pump. This change in pressure will account for major losses through the piping, minor losses through various fittings, the pressure drop through the heat exchanger unit, and the pressure drop through the MD unit. In this study, we limit our consideration to simply the pressure drop through the MD unit as described in equation (4.15), which assumes incompressible and isentropic flow.

$$\dot{W}_D = \dot{m}_D \, v \left(p_{D,in} - p_{D,out} \right) \quad 4.15$$

The load for the cold water pump is a function of the cold water flow rate and the pressure increase across the pump. This change in pressure will account for major losses through the piping, minor losses through various fittings, the pressure drop through the heat exchanger unit, and the pressure drop through the MD unit. In this study, we limit our consideration to simply the major losses through the piping and the head associated with the depth of pumping as described in equation (4.16).

$$\dot{W}_C = \dot{m}_C \left(g \, z + f \frac{L}{d} \frac{u^2}{2} \right) \quad 4.16$$

Where g is gravitational acceleration, z is elevation height, f is the friction factor which can be obtained from the Moody chart or other similar reference or in the case of laminar flow (such as is the case in this analysis) it can be simply obtained from f=64/Re. L is pipe length, u is average velocity, and d is internal pipe diameter. We assume in this study that the pipe length is approximately equal to the cold water depth, $z = L$ (i.e. neglecting any lateral runs of pipe).

From equation (4.16) we can see that the pumping load for cold deep ocean water is quite case specific and will depend on a number of design variables. By analysis we can see that at least three design variables must be defined. (1) Either the pipe diameter d or flow velocity u must be selected. Then, given a certain cold water flow rate $\dot{m}_C$, the other can easily be obtained from the relation $\dot{m}_C = u \, A \, \rho = u \, \pi \, d^2/(4 \, v)$. (2) Either the cold water flow rate $\dot{m}_C$ or the cold water depth z must be selected. Then, given a certain thermal load $\dot{Q}_{load}$, the other can be obtained from equations (4.11c) or (4.12c) and a

relation for depth z versus cold water temperature $T_{C,in}$. (3) The heat exchanger effectiveness ε.

4.3 Materials and Methods

4.3.1 Laboratory Test bench

A laboratory scale MD test bench was designed and built to evaluate the performance of the system in low temperature of the distillate side. Figure 4.5 shows a picture and schematic of the test bench. The bench consists of a 4-port acrylic membrane module for direct contact MD (CF042A, Sterlitech, Kent WA). Feed and distillate are supplied to the module by two variable frequency drive pumps. Pump speed (and hence circulation rates of the feed and distillate) are controlled by input signals provided by inline mass flow sensors (KD100A-SCF-S0A-KA-2×and KF-F200A-SCF-S0A-KA-2×, Alicat Scientific, Tucson AZ). A third mass flow sensor (KD100A-SCF-S0A-KA-2×, Alicat Scientific, Tucson AZ) is installed at the distillate exit of the membrane. In addition, two mass scales (CS 200, OHAUS (Parsippany, NJ)) were used for making NaCl solution also calculating the water flux with continually measuring the feed side mass. The temperature of the feed and distillate is controlled by circulating feed through a coil that is submerged in a thermostatically regulated bath. Temperature sensors are located at each of the four membrane ports to allow for energy balance analysis. Pressure loss in channels along both sides of the membrane are measured by differential pressure sensors (PS-30PSID-D/5P, Alicat Scientific, Tucson AZ). Table 4.1 provides a list of all instrumentations with their specifications.

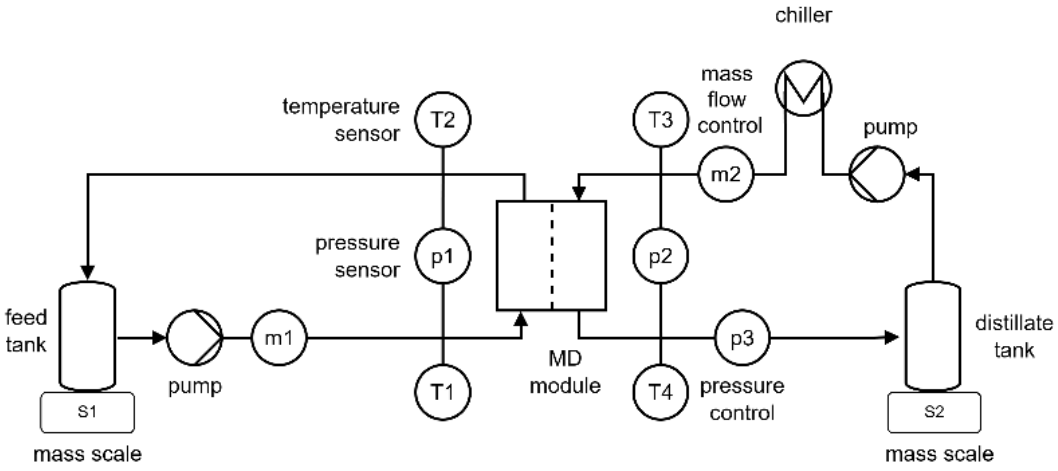

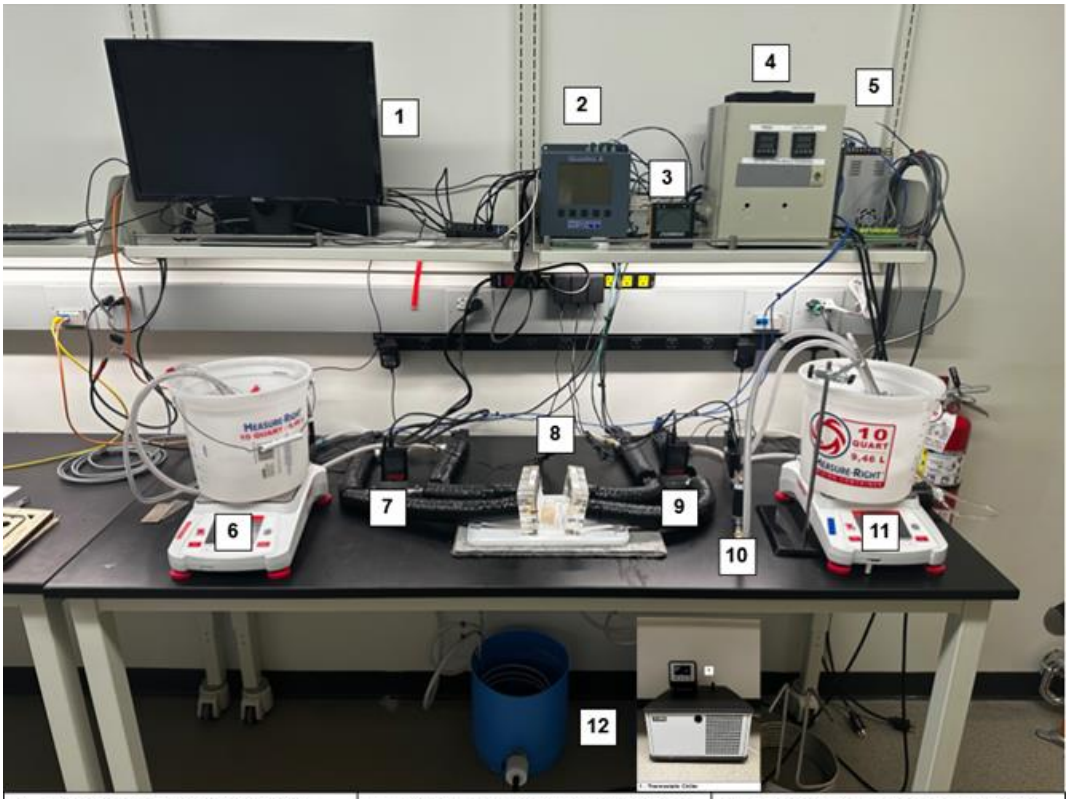

1 - Data Acquisition Computer	5 - DC Power Supply & Distribution	9 - Differential Pressure Sensor
2 - Data Acquisition System	6 - Feed Mass Balance*	10 - Permeate Mass flow Meter
3 - Conductivity Transmitter	7 - Differential Pressure Sensor	11 - Permeate Mass Balance*
4 - PID Temperature Controller	8 - Membrane Module	12 - Heat Exchange Baths

Figure 4.5 Schematic (top) and photo (bottom) of the laboratory bench MD test apparatus. The system includes flat sheet membrane housing with two channels supplied by feed and distillate circulation loops. The bench is instrumented with mass flow, temperature, and pressure sensors to allow for mass and energy balance analysis.

Table 4.1 Sensor and instrument specifications. Instrument numbers correspond to locations indicated on Figure 4.5.

Instrument	Supplier	Model #	Full Scale ± Uncertainty	Instrument Location
Feed mass flow controller	Alicat Scientific (Tucson, AZ)	KD100A-SCF-S0A-KA-2X	1 kg/h ± greater of 0.2 % full scale or 0.6 % reading	m1
Distillate mass flow controller	Alicat Scientific (Tucson, AZ)	KF-F200A-SCF-S0A-KA-2X	10 kg/h ± greater of 0.2 % full scale or 0.6 % reading	m2
Mass flow meter	Alicat Scientific (Tucson, AZ)	KD100A-SCF-S0A-KA-2X	1 kg/h ± 0.2 % full scale or 0.6 % reading	m3
Differential pressure sensor	Alicat Scientific (Tucson, AZ)	PS-30PSID-D/5P	1 bar ± 0.25 % full scale	p1, p2
Applied pressure controller	Alicat Scientific (Tucson, AZ)	PCS-100PSIG-D-PCA17/5P	21 bar ± 0.25 % full scale	p3
Temperature sensor	Noshok (Berea, OH)	800-200-1-1-8-8-040-6 RTD	93.33 ± 0.465 °C	T1, T2, T3, T4
Mass scale	OHAUS (Parsippany, NJ)	CS 200	200 ± 0.1g	S1, S2

4.3.2 Membrane Specifications

A commercial polytetrafluoroethylene (PTFE) membrane (Unlaminated CF042, Sterlitech, Auburn, WA) was selected for this study. The flat-sheet membrane had an effective surface area of 42 cm² (107 mm length × 39 mm width) and was installed in the transparent acrylic module. To achieve the desired flow velocities and ensure membrane support, shims were placed in both the feed and draw channels, which reduce the effective depth to 0.801 mm. Additionally, a 31-mil diamond-shaped spacer was placed in the feed channel to increase flow turbulence and prevent channel blockages. The module design allows for easy visualization and access, which facilitates cleaning and experimental monitoring. A summary of the membrane and module parameters is provided in Table 4.2.

Table 4.2 Membrane and module parameters.

Membrane properties	
Supplier	Sterlitech (Auburn, WA)
Material	polytetrafluoroethylene
Pore Size	0.45 µm
Thickness	21 – 51 µm
Water entry pressure	> 3.1 bar (45 psi)
Module properties	
Configuration	flat sheet
Dimensions	107 mm × 39 mm
Area	42 cm^2
Channel depth	0.801 mm
Feed channel spacer	31-mil diamond-shaped

4.3.3 Test Conditions

Performance of the proposed OTMD system was evaluated for seawater desalination. To approximate seawater, feed solution was prepared by dissolving sodium chloride (NaCl, >99% purity, Fisher Scientific, Hampton, NH) in deionized (DI) water at a concentration of 35 g/l. Deionized water was used to provide an initial volume of distillate solution that could be circulated, to which water flux across the membrane was added. The feed temperature was maintained at 30 °C, while the distillate temperature was varied between 12, 14, and 16 °C. Although ocean thermoclines can reach temperatures as low as 5 °C, the chiller capacity used in this study was not able to cool below 12°C. Throughout the experiments, the circulation flow rates were set to 5000 g/h on the feed side and 1000 g/h on the distillate side. These values were selected based on preliminary tests that ensured stable operation without membrane wetting or flow instability. Temperature and flow rate were continuously monitored and recorded using calibrated sensors and data acquisition software. A summary of test conditions is provided in Table 4.3.

Table 4.3. Operating conditions used in system experiment

Test conditions	
Flow configuration	counter flow
Feed concentration	35.00 ± 0.04 g/l NaCl
Distillate concentration	DI water
Feed temperature	30 °C
Distillate temperature	12, 14, 16, 18 °C
Feed circulation rate	5018.5 ± 30.1
Distillate circulation rate	1001.80 ± 6.01

4.3.4 Data Analysis

The distillation rate is determined using a mass balance approach, which shows the change in mass of either the feed or distillate reservoir over a given time interval. This method provides a direct measurement of the net water transferred across the membrane during the distillation process. In this study, the mass balance was taken on the feed side. The mass balance equations is as follow:

$$\Delta \dot{m} = \frac{m_F(t) - m_F(t + \Delta t)}{\Delta t} \tag{4.17}$$

The thermal load required for distillation is estimated to be using energy balance principles and then normalized per unit of water produced. In this study, the energy balance was taken on the distillate side:

$$\frac{\dot{Q}_{load}}{\Delta \dot{m}} = \frac{\dot{m}_D}{\Delta \dot{m}}\, cp\, \left(T_{D,out} - T_{D,in}\right) \tag{4.9c}$$

The pumping loads for the feed, distillate, and cold water streams are calculated based on pressure or elevation head losses and then normalized per unit of water permeate. For the feed and distillate streams, the work is determined using the pressure difference across the module, while for the cold water stream, it includes both gravitational and frictional losses in the intake pipe, which is estimated based on design parameters explain in section 4.3.

$$\frac{\dot{W}_F}{\Delta\dot{m}} = \frac{\dot{m}_F}{\Delta\dot{m}}\, v\left(p_{F,in} - p_{F,out}\right) \tag{4.14}$$

$$\frac{\dot{W}_D}{\Delta\dot{m}} = \frac{\dot{m}_D}{\Delta\dot{m}}\, v\left(p_{D,in} - p_{D,out}\right) \tag{4.15}$$

$$\frac{\dot{W}_C}{\Delta\dot{m}} = \frac{\dot{m}_C}{\Delta\dot{m}}\left(g\, z + f\,\frac{L}{d}\,\frac{u^2}{2}\right) \tag{4.16b}$$

4.3.5 Design Parameters

From equation (4.16) we can see that the pumping load for cold deep ocean water is quite case specific and will depend on a number of design variables. By analysis it can be shown that at least 3 design variables must be defined to solve. (i) Either the pipe diameter d or flow velocity u must be selected. Then, given a certain cold water flow rate m_C, the other can easily be obtained from the relation $\dot{m}_C = u\,\pi\, d^2/4\, v$. In this study, we consider several possible flow velocities including u = 0.01, 0.05, and 0.1 m/s. (ii) Either the cold water flow rate $\dot{m}_C$ or the cold water temperature $T_{C,in}$ must be selected. Then, given a certain thermal load $\dot{Q}_{load}$, the other can be obtained from equations (4.11c) or (4.12c). In this study, we consider several possible cold water flow rates including $\dot{m}_C$ = $0.5\dot{m}_D$, $0.75\dot{m}_D$, $1\dot{m}_D$. (iii) The heat exchanger effectiveness ε. In this study, we consider several cases for the heat exchanger including ε = 0.5, 0.75, 1.

Table 4.4 Cold water design parameters

Cold water design parameters	
Flow velocity u	0.01, 0.05, 0.1, m/s
Heat exchanger effectiveness ε	0.5, 0.75, 1
Cold water flow rate $\dot{m}_C$	0.5, 0.75, 1 × $\dot{m}_D$

Finally, in addition to the design parameters, determining the cold water pump load depends on the relationship between cold water temperature $T_{C,in}$ and the cold water depth

z. This can be defined by referring to datasets for the thermocline at the island location. Figure 4.6 shows the temperature profile of the thermocline at a sample location off the coast of American Samoa. The temperature profile within a radius of approximately two miles from American Samoa is plotted. As depicted, temperature decreases sharply with depths up to 500 m, followed by a more gradual decline beyond that depth.

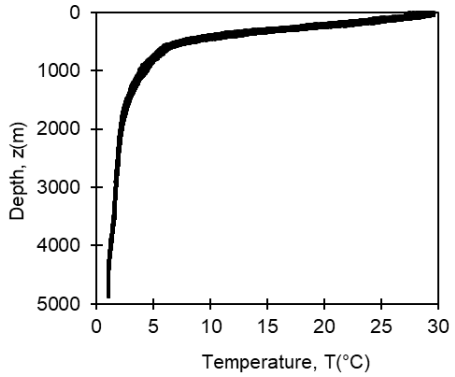

Figure 4.6 Temperature profiles with depth from three stations located within approximately two miles of American Samoa.

4.4 Results

To evaluate the performance of the ocean thermal membrane distillation system, we first present experimental results obtained from a laboratory-scale bench setup. These tests assess the impact of distillate temperature on system performance metrics such as water flux, thermal load, and pumping energy requirements. Following this, a case study based on the thermocline conditions of Aunuʻu Island in American Samoa is analyzed to examine real world applicability.

4.4.1 Laboratory Bench Performance

Figure 4.7 shows the performance of the ocean thermal membrane distillation system under varying distillate temperatures. As can be seen in Figure 4.7(a) the water flux increases with decreasing distillate temperature. This trend is because of the fact that with

decreasing the distillate temperature, the temperature difference of both feed and distillate side increases and subsequently the vapor pressure difference increases and leads to enhancing flux. On the other hand, in Figure 4.7(b), it is seen that the specific cooling load has a decreasing trend with decreasing distillate temperature. This shows that with decreasing distillate temperature the rate of enhancement of water flux is more than increasing the load, that's why a decreasing trend in specific colling load could be observed.

A similar trend is observed for the specific pumping load of both the feed and distillate pumps. The flow rates remain constant and the pumping energy consumption is nearly unchanged. As Figures 4.7(c) and (d) show, the specific pumping load decreases with decreasing the distillate temperature. This is primarily due to the increase in water flux, which appears in the denominator of the specific pumping load equation. Overall, decreasing the distillate temperature demonstrates a desirable effect on system performance by enhancing water flux while at the same time reducing the specific energy requirements for both cooling and pumping.

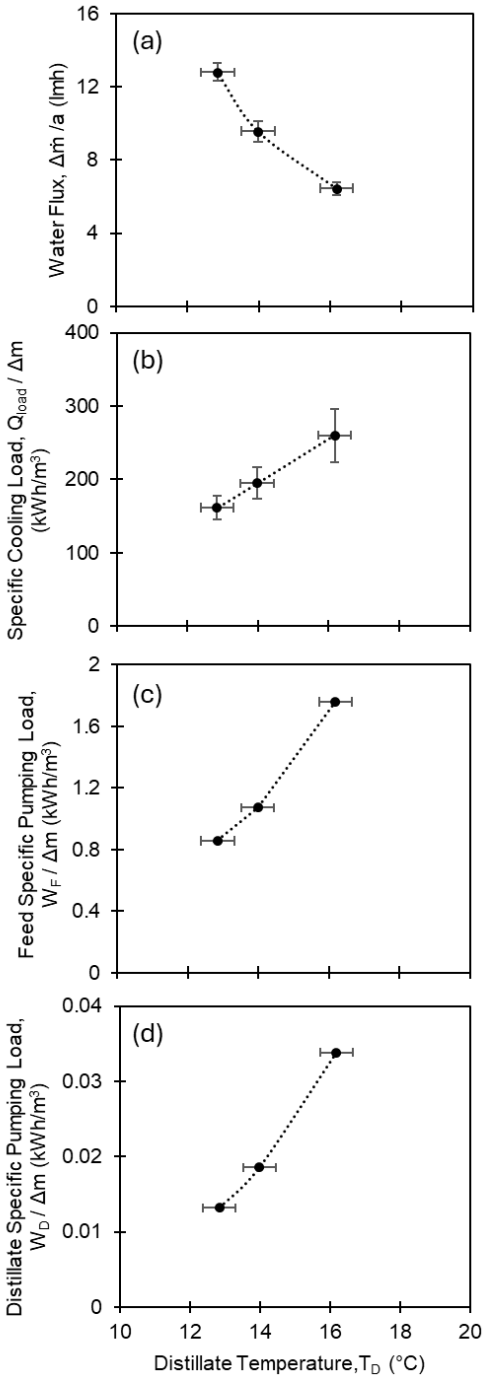

Figure 4.7 Performance and energy metrics of the ocean thermal memebrane distillation system under varying distillate temperatures. (a) Water flux as a function of distillate stream temperature, showing a decreasing trend with increasing temperature. (b) Specific cooling load versus distillate temperature, indicating that lower distillate temperatures require higher cooling energy per unit of water produced. (c) and (d) Feed and distillate side specific pumping load decreases with decreasing distillate temperature, showing the effect of increasing water flux.

4.4.2 Case Study of OTMD Applied to Aunu'u Island, American Samoa

To evaluate the applicability of the OTMD system in remote islands, a case study is conducted for Aunu'u Island in American Samoa, where ocean thermal gradients are promising for using in thermal desalination. In this section, system performance is analyzed under specific conditions, considering realistic temperature profiles and resource availability.

Figure 4.8 shows the variation of water flux, specific cooling load, feed specific pumping load, and distillate specific pumping load with cold water temperature across different heat exchanger effectiveness (ε = 0.5, 0.75 and 1) and cold water flow rates ($\dot{m}_C$ = 0.5, 0.75 and 1×$\dot{m}_D$). A consistent trend is observed across all figures. Decreasing the cold water temperature leads to an increase in water flux, driven by enhanced cooling of the distillate stream in the MD system. This improvement in flux subsequently results in lower specific pumping and cooling loads. Additionally, for a given water flux, increasing the cold water flow rate enables operation at a higher cold water temperature. This suggests that a target flux can be achieved either by reducing the intake water temperature or by increasing the cold water flow rate, providing flexibility in system design based on the availability of cold water resources.

Another important observation is that at very low cold water flow rates, meeting the required cooling load necessitates the use of extremely low cold water temperatures. For example, this required temperature can drop to approximately -2 °C, which falls outside the typical available thermocline temperature range.

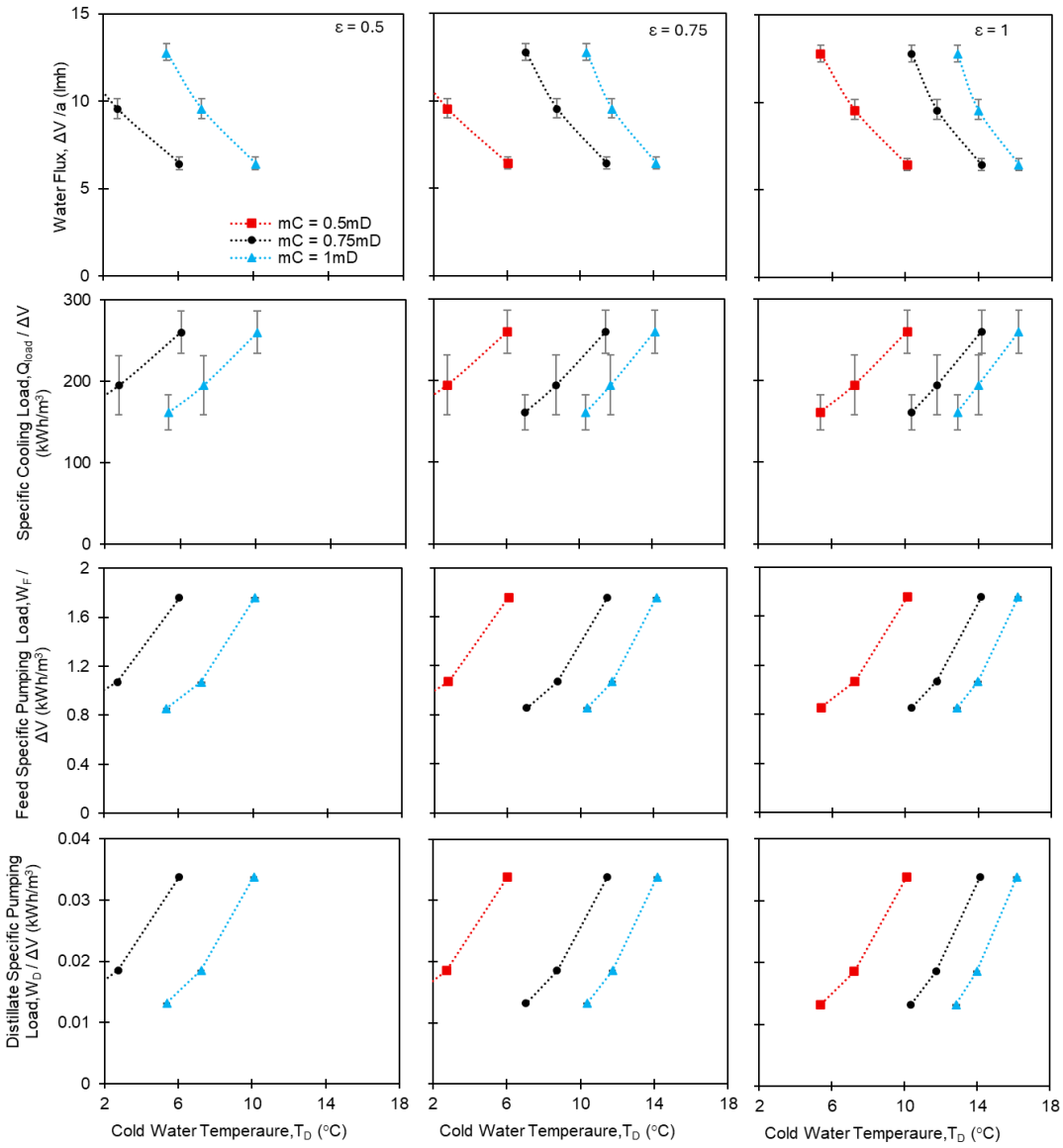

Figure 4.8 Variation of water flux, specific cooling load, feed specific pumping load, and distillate specific pumping load for different cold water temperatures and different range of heat exchanger effectiveness and cold water flow rates.

Figure 4.9 shows the relationship between the specific pumping load of the cold water stream and the cold water temperature for different stream velocities of 0.01, 0.05 and 0.1 m/s. Logically, lowering the cold water temperature increases the required pumping load, since colder water must be drawn from larger ocean depths. However, this colder water also enhances the driving temperature gradient, resulting in higher water flux.

Consequently, when calculating the specific pumping load (energy per unit of water produced), the value increases as cold water temperature decreases. Again here it can be seen for the very low flow rates of the cold water and for low effectivness values the cold temperature falls outside the typical available thermocline temperature range. Overall, it can be concluded that the cooling load extracted from the heat sink is a function of three key parameters of cold water flow rate, cold water temperature, and the effectiveness of the heat exchanger.

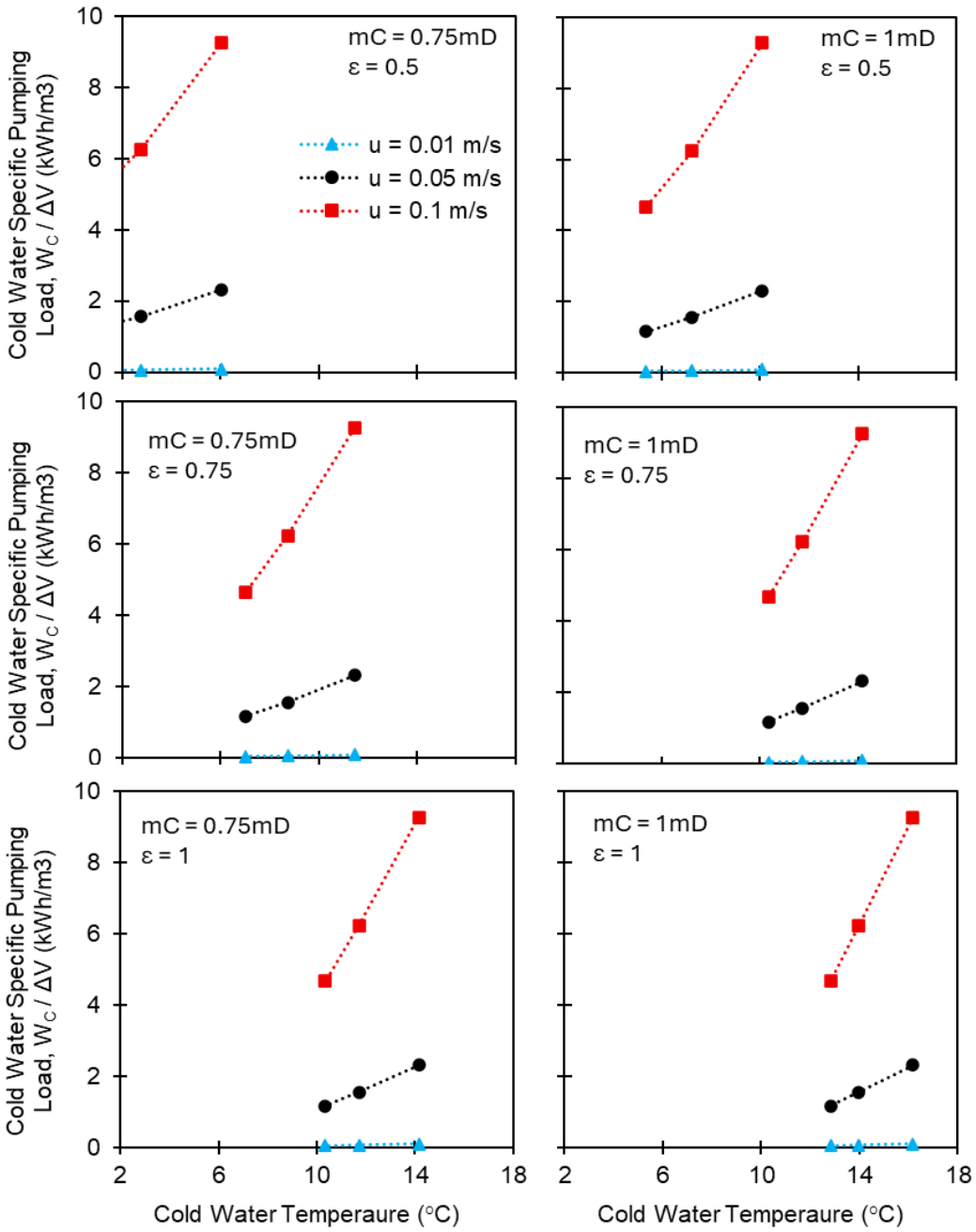

Figure 4.9 Cold water specific pumping load as a function of cold water temperature, shown across different ranges of flow rates, velocities heat exchanger effectiveness values

Figure 4.10 presents the total specific pumping load of the OTMD system, which includes the combined specific pumping loads of the feed and distillate streams within the membrane distillation module, as well as the cold ocean water intake. As previously

discussed, the total specific pumping load serves as a meaningful metric to assess the overall energy requirements of the system and to compare its performance with alternative desalination technologies.

The figure illustrates the variation in total specific pumping load across different cold water intake velocities, cold water flow rates, and heat exchanger effectiveness values. As expected, higher intake velocities lead to increased pumping loads due to greater frictional losses along the cold water transport path.

For reference, the gray shaded region in each figure indicates the typical range of specific energy consumption for conventional reverse osmosis (RO) systems, reported in the literature to be approximately 2.5–4 kWh/m³. Notably, under several conditions, particularly at intake velocities of 0.01 and 0.05 m/s, the total specific pumping load of the OTMD system falls within or even below this RO benchmark. This demonstrates that, under optimized conditions, OTMD can achieve comparable or even superior energy efficiency relative to conventional RO desalination. As previously discussed, in cases with low cold water flow rates and low heat exchanger effectiveness, such as when mC = 0.5mD and $\varepsilon = 0.5$.

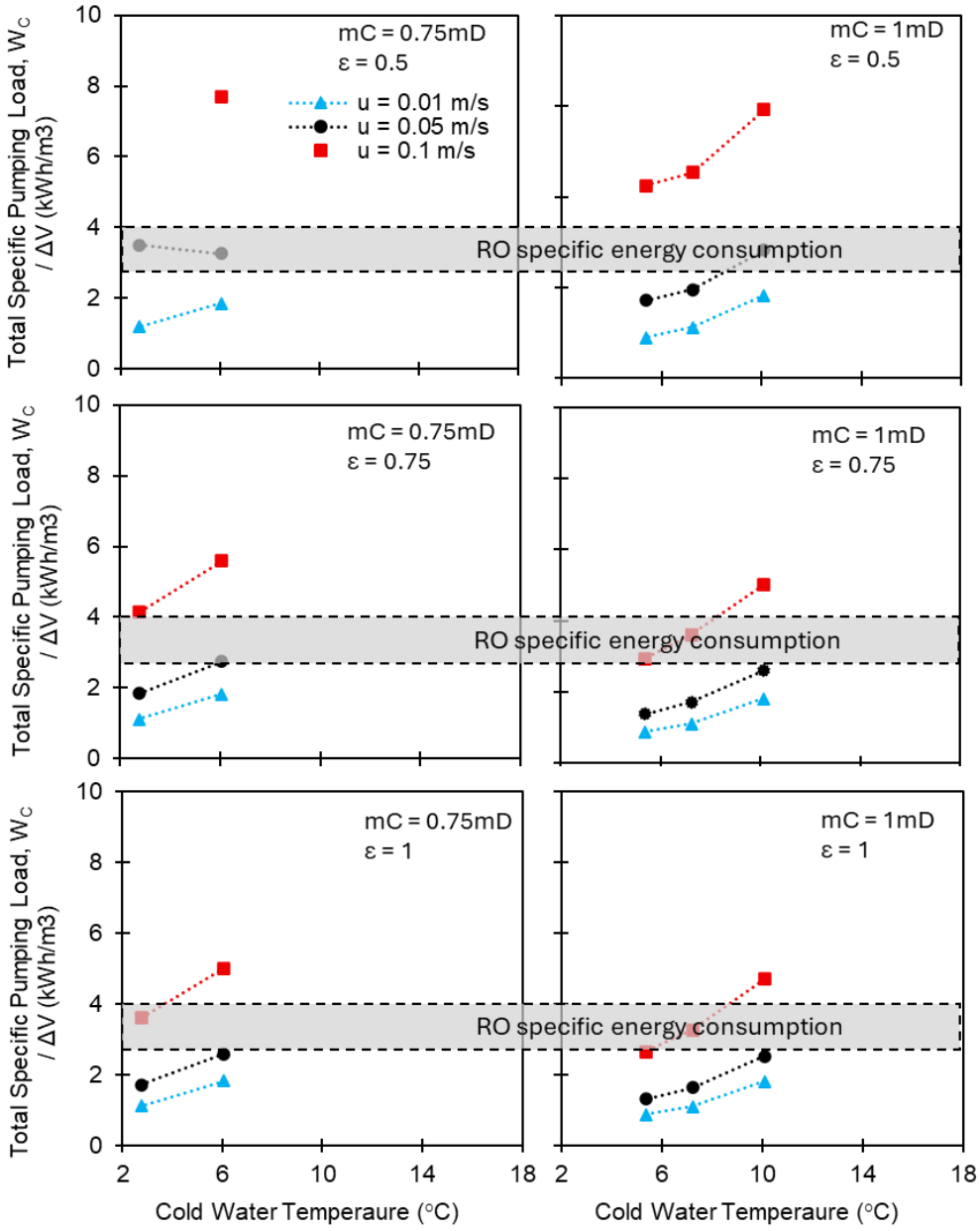

Figure 4.10 Total specific pumping load as a function of cold water temperature, shown across different ranges of cold water flow rates, cold water velocities and heat exchanger effectiveness values

4.5 Conclusion

The case study conducted for Aunu'u Island in American Samoa demonstrated the potential applicability of the OTMD system in remote islands where ocean thermal gradients are accessible. The results revealed the critical influence of cold water

temperature, flow rate, and heat exchanger effectiveness on system performance. Lowering the cold water temperature significantly improved water flux and reduced specific energy loads, however, this came with practical limitations, as extremely low intake temperatures are not feasible in real world operations. The analysis showed that increasing the cold water flow rate or improving heat exchanger effectiveness can compensate for higher intake temperatures, offering flexibility in system design based on local resource availability. Importantly, the total specific pumping load of the OTMD system under several configurations, particularly with cold water velocities of 0.01 and 0.05 m/s, fell within or below the energy consumption range of conventional reverse osmosis systems. These findings underscore the viability of OTMD as a low-energy desalination solution for island communities, provided that system components are properly optimized to balance thermal recovery and hydraulic efficiency.

CHAPTER FIVE

MINIMIZING THE THERMAL ENERGY USE OF MEMBRANE DISTILLATION WITH REAL-TIME OPERATING CONTROLS

5.1 Introduction

Clean water is essential to life, and yet millions of people around the world lack access to this fundamental resource [187], [188]. As global population and water consumption continue to rise, projections show that about two-thirds of people throughout the world will suffer from water stress by the year 2030 [189]. Desalination and water reuse will play a pivotal role in addressing this challenge [190], [191], [192].

Desalination is the process of separating water from salt, and thereby can produce freshwater for drinking, sanitation, and irrigation from seawater, brackish water, and various industrial or natural brines. Desalination is of course a natural part of the earth's hydrological cycle [193], [194], but engineered systems can achieve the same in a controlled and accelerated way to meet human demand. Traditionally, desalination was done by evaporation [195] but in the last half century, reverse osmosis (RO) has become the preferred method [195]. More recently, membrane distillation (MD) has emerged as an alternative desalination process with many advantages [196].

Figure 5.1 illustrates the operation of a membrane distillation (MD) system. As shown, seawater (or some other impaired water source) is heated and circulated through the system as feed. Clean distilled water is kept cool and is circulated through the system as distillate. At the interface of these two fluids is a porous hydrophobic membrane, across which a vapor pressure difference between the hot feed and cool distillate induces

vaporization of the feed, flux across the membrane, and then condensation at the surface of the distillate. The simple design shown here, brings feed and distillate directly in contact with the selective membrane, and is referred to as direct-contact MD [51], [173], [174]. But in an effort to improve transport dynamics, a variety of other MD designs and configurations have also been proposed, including the integration of an air gap with the membrane [175], [176], an air gap with a circulating sweep gas [179], [180], air gaps with a gas that is under vacuum [177], [178], or more recently the absence of any membrane altogether [181], [182]. Figure 5.1 also shows that heat exchangers are used to reduce the amount of heat that is supplied to the feed from the external source, by recovering heat from the feed and distillate as they exit the membrane module.

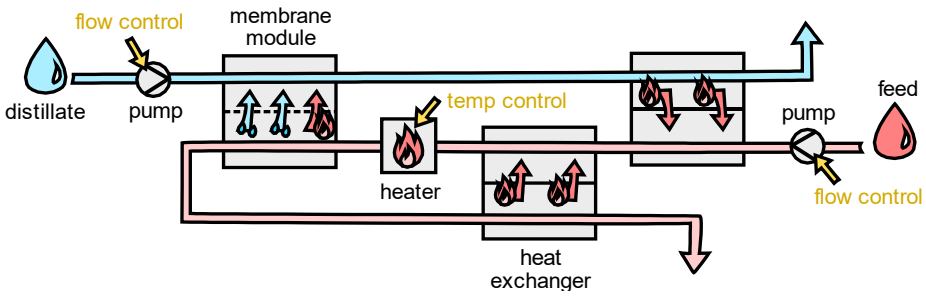

Figure 5.1 In membrane distillation (MD) a vapor pressure difference between warm seawater feed and cool freshwater distillate drives vapor transfer across a porous hydrophobic membrane. To reduce the thermal energy load, heat can be recovered from the brine and distillate as it exits the membrane module.

MD offer several advantages over other desalination technologies. First, since vapor pressure is highly sensitive to temperature and only slightly sensitive to salt concentration, MD is capable of desalinating very concentrated feed sources at modest temperatures. This enables water recovery from highly concentrated feed sources like brines, produced water from oil and gas [167], brines, wastewater from textiles [168], and

others [169]. Also, it enables a high percentage of feed volume to be recovered as distillate, which is important to reducing brine volumes and mitigating their associated environmental impacts [197], [198]. In comparison, RO requires energy intensive and prohibitively large applied pressures to desalinate high concentration feed and to achieve high recovery ratios [199]. Second, MD is a thermally driven process, making it possible to integrate various low-grade heat sources including renewables and waste heat [200]. Third, MD is capable of producing very high-quality water [201] as long as care is taken to avoid membrane wetting, in which membrane channels are filled with water, creating a bridge for salt and other impurities to permeate to the distillate [202].

Despite all of these advantages, there are several challenges that remain for MD, particularly in terms of energy consumption. Like other thermal desalination processes, much of the energy required for MD is associated with the enthalpy of vaporization of water, which is approximately 667 kWh/m^3 at standard atmospheric pressure. This energy is necessarily removed from the feed. Energy is also lost via heat transfer from the warm feed to the cool distillate across the thin membrane interface, and to the environment surrounding the MD system [203]. The energy efficiency of MD is then largely a matter of how effectively this energy can be recovered, typically via heat exchangers, and recycled back to the incoming feed to reduce the need for heat input. Energy performance is often expressed as the ratio of enthalpy of vaporization compared to the heat input, which is known as the gain output ratio $\mathrm{GOR} = \mathrm{H_{fg}}/\mathrm{Q}$. It is also often expressed as the ratio of heat input relative to the volume of water produced, $\mathrm{Q}/\Delta\mathrm{V}$, known as the specific heat input. For direct contact MD, specific heat input from 600 to 1600 kWh/m^3 has been reported throughout the literature, which is equivalent to gain output ratios between 0.42

and 1.11. Configurations that integrate air gaps with the membrane are more efficient, with specific heat inputs of less than 300 kWh/m^3 reported in the literature [204], [205], [206]. In addition to heat, MD also requires a certain amount of work (i.e. electricity) to run the feed and distillate circulation pumps, which typically consume somewhere from 0.6 to 1.8 kWh/m^3 [207], [208], [209]. This energy is much less than the heat input, but still worth considering. For reference, the work input for RO desalination typically ranges from 2.5-7 kWh/m^3 [207], [208], [209].

The energy efficiency of MD is sensitive to system operating conditions. Although not drawn to scale, Figure 5.2 illustrates the effect of key operating conditions on energy use and performance. As shown, increasing circulation rates of feed and distillate improve the rate of clean water production [210]. This is because higher flow rates cause mixing, reduce temperature polarization, and promote more uniform temperatures over the whole membrane surface [211], [212]. However, these benefits are accompanied by (1) more rapid heat loss across the membrane and therefore higher heating loads [213], [214], and (2) increased hydraulic pressure loss due to friction and therefore higher pump loads [215]. Beyond a certain point the increased distillation rate is offset by the need for more heat and work input, and the resulting specific heat input and specific work will increase. A similar tradeoff is also observed in response to different feed temperatures. Heating the feed has the beneficial effect of driving more rapid distillation, but also the negative effect of more rapid heat loss [214], [216], [217]. These trends suggest that, due to the monotonic increase in flow rates, temperatures, and water flux, there must be a point at which the MD system reaches its minimum specific energy consumption. Improving the energy efficiency of MD is therefore largely a matter of balancing the rate of water

distillation against the rate of heat transfer from the hot feed to the cold distillate. This can be done with careful control of operating conditions.

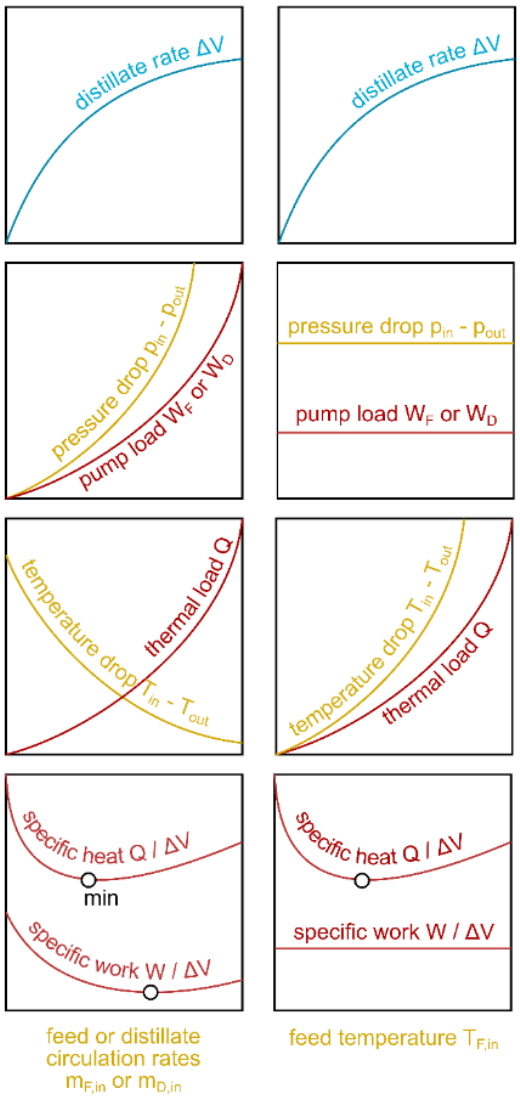

Figure 5.2 Specific work and heat input (work and heat per unit volume of distillate output) can be minimized at some particular feed circulation rate, distillate circulation rate, and feed temperature.

Considering then the importance of the operating conditions, the question is how to optimize them and identify the conditions that reduce energy use. At the design stage various methods can be employed, such as lab testing, prototyping, and numerical modelling [216], [217]. Ultimately however, field conditions may differ significantly

from design conditions and may vary over time due to weather, climate, wear and tear on equipment, and other factors. Therefore, it is useful to consider methods of identifying the best MD operating conditions in the field in real-time.

To date, much of the literature related to real-time control of desalination plants has been related to RO. For example, Zhu et al. [218] developed and experimentally validated an optimization-based control system for RO that minimized specific energy consumption while maintaining desired water output. By integrating a nonlinear system model with real-time feedback and optimization, the control strategy successfully tracked energy-efficient operating points. Another example, Ali [219] developed an online control system for a wind-driven RO desalination including water storage tanks for regulating water production due to wind energy variation, disturbances, and operational limitations. The control system regulated the feed pressure and the number of working RO units in order to enhance overall performance. A third example, Zhang et al. [220] reported a real-time optimization method for seawater desalination to reduce costs under varying freshwater demand. Using a rolling forecasting model and a nonlinear programming approach, they demonstrated improved cost-efficiency while avoiding water level violations.

Similar studies for the real-time control of MD operating conditions are more rare. One of the few studies investigating real-time control of MD was conducted by Gil et al. [221] who proposed an adaptive dynamic optimization approach with online feedback that learns current operating conditions and responds to changes in real-time. This strategy was validated through a simulation using real data from the Plataforma Solar de Almería, demonstrating up to a 6.7% reduction in thermal energy consumption compared

to non-optimal methods. Notably, this study was limited to only simulation of the real-time control of the MD system. To date, there has not been any attempt to implement real-time controls for an experimental MD system, as far as the authors are aware. This study addresses this important gap in literature.

In this study, we experimentally demonstrate a real-time feedback control system that is used to track the lower specific heat input of MD by adjusting operating conditions. To begin, we define the theoretical work and heat input loads for MD assuming ideal heat recovery. Then we describe a simple control strategy known as perturb-and-observe, which is developed here to iteratively adjust feed circulation, distillate circulation, and feed temperature such that over time the MD system approaches the point of minimum specific heat input. A laboratory test bench with a direct contact MD unit was assembled and is described with all its relevant specifications. The system's dynamic response to a series of step changes is provided. Finally, MD performance is evaluated in response to the proposed real-time controls, and the effect on specific heat input is demonstrated. This work represents the first experimental demonstration of a minimum energy tracker for MD and as such can contribute to efforts to make desalination and water reuse more energy efficient.

5.2 Theory

5.2.1 MD Energy Use and Performance

The performance of MD can be evaluated with several metrics. Of particular importance is the ratio of energy use relative to the amount of clean water produced by the process ΔV. This ratio is known as the specific energy, and since MD uses both heat

Q and work W, we can distinguish between the specific heat input q and specific work w as shown in equations (5.1) and (5.2).

$$q = \frac{Q}{\Delta V} \tag{5.1}$$

$$w = \frac{W}{\Delta V} \tag{5.2}$$

The rate at which clean water is produced by MD can be obtained from the mass balance on either the feed or distillate sides, as expressed in equation (5.3).

$$\Delta \dot{V} = \nu \left(\dot{m}_{F,in} - \dot{m}_{F,out} \right) \tag{5.3a}$$

$$\Delta \dot{V} = \nu \left(\dot{m}_{D,out} - \dot{m}_{D,in} \right) \tag{5.3b}$$

Where ν is the specific volume, and $\dot{m}_F$ and $\dot{m}_D$ are the feed and distillate circulation rates at the MD inlets and outlets.

The heating load of MD can be reduced to simply the heat transfer through the membrane, if the system is assumed to be perfectly insulated with no losses to the environment, and if it is assumed that ideal heat exchangers can recover all of the heat available in the brine and distillate. This can be calculated from the energy balance between the MD inlet and outlet at either the feed side or distillate side, as shown in equation (5.4) [222], [223]. A detailed derivation is provided in Supplementary Note 5.1.

$$\dot{Q} = \dot{m}_F \, cp \left(T_{F,in} - T_{F,out} \right) \tag{5.4a}$$

$$\dot{Q} = \dot{m}_D \, cp \left(T_{D,out} - T_{D,in} \right) \tag{5.4b}$$

Where cp is the specific heat capacity, and T_F and T_D are the feed and distillate temperatures at the MD inlets and outlets.

Work input for MD will be a function of the pump load, including both the feed and distillate pumps, which can be determined as a function of the pressure drop caused by friction throughout the system and assuming incompressible and isentropic flow.

$$\dot{W} = \dot{W}_F + \dot{W}_D \tag{5.5}$$

$$\dot{W}_F = \dot{m}_F \, v \left(p_{F,in} - p_{F,out}\right) \tag{5.6}$$

$$\dot{W}_D = \dot{m}_D \, v \left(p_{D,in} - p_{D,out}\right) \tag{5.7}$$

Where p_F and $p_D$are the feed and distillate pressures at the MD inlets and outlets.

Figure 5.3 provides an illustration of all the terms used in the mass and energy balance equations (5.3) - (5.7) and where they can be observed in the MD system.

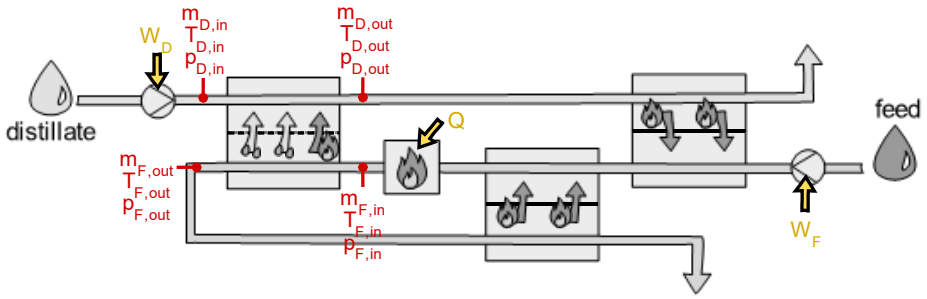

Figure 5.3 Schematic showing all parameters used in the mass and energy balance equations (5.3)-(5.7) and their corresponding measurement locations within the membrane distillation system.

The performance of MD can also be evaluated in terms of the gain output ratio GOR, which is a ratio of the enthalpy of vaporization H_{fg} relative to the heat input Q. This metric is commonly used for thermal desalination because it provides a useful comparison between the process and the alternative of simply boiling water to separate water from less volatile salts and impurities.

$$\mathrm{GOR} = \frac{H_{fg}}{Q} \tag{5.8}$$

5.2.2 Tracking the Minimum Specific Energy point

To reduce the specific energy use of MD, it is necessary to carefully balance the operating conditions. To do this, a method for adjusting operating conditions in real-time is needed to ensure peak MD performance. There are a variety of algorithms have been proposed for this including fuzzy logic, multi-level perceptron, grey wolf optimization and other complex methods [224], [225], [226], [227]. One relatively simple control strategy is known as perturb-and-observe. This algorithm is a broadly used heuristic optimization method that iteratively perturbs a parameter and observes the subsequent system response to determine the optimal operating point. This method initially was developed for maximum power point tracking in photovoltaic systems [33] and has since been used in a variety of applications [228], [229], [230].

Figure 5.4 provides an illustration of the perturb-and-observe algorithm in action, and Figure 5.5 describes the algorithm's logic. As shown, the basic operation involves applying small perturbations of magnitude $\delta\dot{m}_F$ to the feed circulation rate, $\delta\dot{m}_D$ to the distillate circulation rate, and δT_F to the feed temperature, at time intervals of δt. The result of the step change on some objective metric is then observed. In this study, we select the specific heat input as the metric of interest. Therefore, if the specific heat input is seen to decrease, the same small perturbation is repeated. If on the other hand, the response is an increase in specific heat input, then the opposite perturbation is applied. In this way, step by step, the system slowly approaches the lower specific heat input. In the MD system, since there are three operating conditions to control, perturbations are applied to each of them individually in turn. Each parameter is adjusted to a period of time τ, allowing for a certain number of steps $n = \tau/\delta t$ to be applied, before the

parameter is held constant, while the next parameter is adjusted, and so on. In this process, both the perturbation size and time interval can influence the time required to approach the best operating point, as well as the accuracy of the steady state operation relative to the true minimum energy point. This sensitivity is often considered a limitation to the perturb-and-observe algorithm.

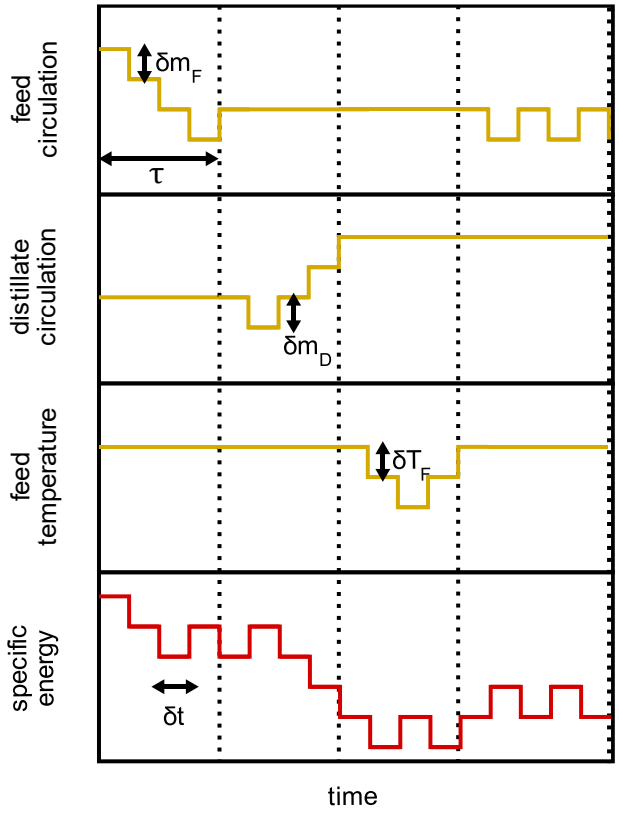

Figure 5.4 Illustration of the perturb-and-observe algorithm applied to tracking the lower specific energy input of an MD system, by controlling the feed circulation rate, distillate circulation rate, and feed temperature.

Control of feed temperature $T_{F,in}$

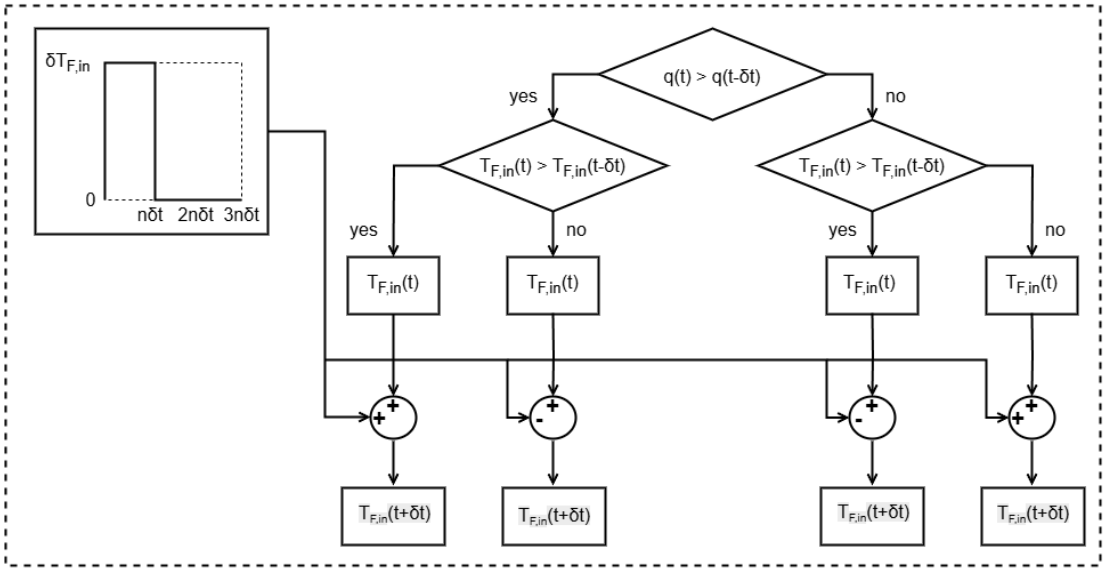

Control of feed flow rate $m_{F,in}$

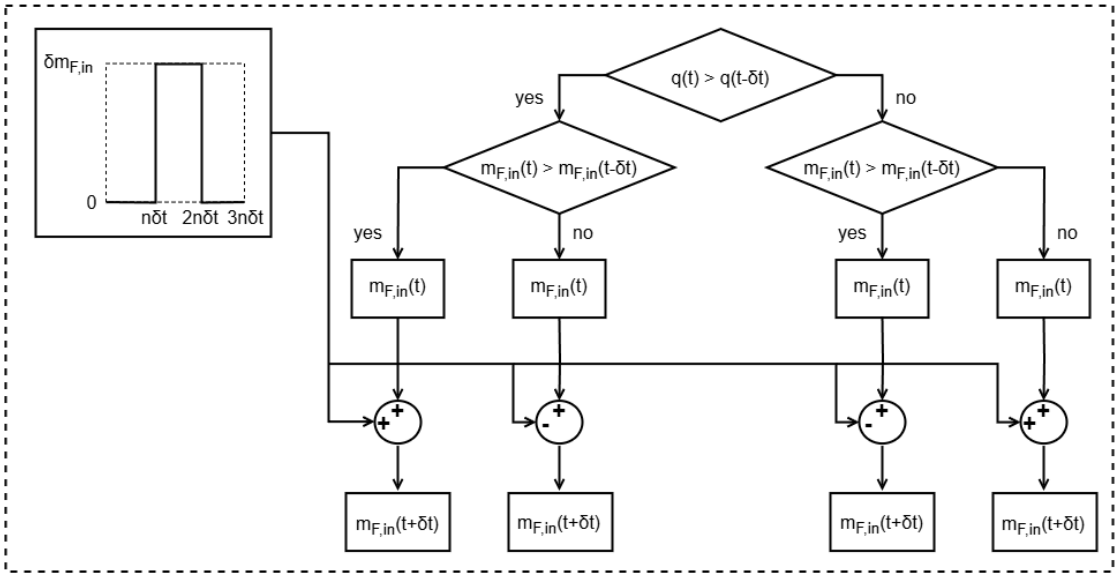

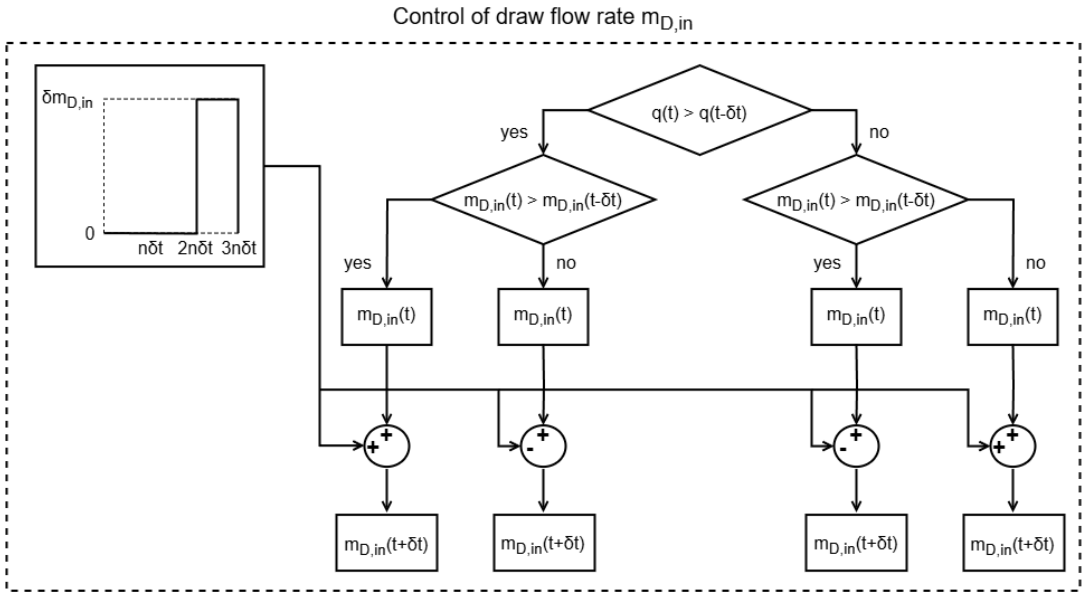

Figure 5.5 Logic of the perturb-and-observe algorithm. Perturbations of magnitude $\delta\dot{m}_F$, $\delta\dot{m}_D$, and δT_F are applied to the feed circulation, distillate circulation, and feed temperature, at time intervals of δt, to identify conditions that minimize specific heat input q.

5.3 Materials and Methods

5.3.1 Laboratory Test Bench

A laboratory scale MD test bench was designed and built to evaluate the performance of the proposed control system. Figure 5.6 shows a picture and schematic of the test bench. The bench consists of a 4-port acrylic membrane module for direct contact MD (CF042A, Sterlitech, Kent WA). Feed and distillate are supplied to the module by two variable frequency drive pumps. Pump speed (and hence circulation rates of the feed and distillate) are controlled by input signals provided by inline mass flow sensors (KD100A-SCF-S0A-KA-2×and KF-F200A-SCF-S0A-KA-2×, Alicat Scientific, Tucson AZ). A third mass flow sensor (KD100A-SCF-S0A-KA-2×, Alicat Scientific, Tucson AZ) is installed at the distillate exit of the membrane in order to complete the mass balance and allow calculation of distillation rates. Temperature of the feed is controlled by circulating feed through a coil that is submerged in a thermostatically regulated bath. Temperature

sensors are located at each of the four membrane ports to allow for energy balance analysis. Pressure loss in channels along both sides of the membrane are measured by differential pressure sensors (PS-30PSID-D/5P, Alicat Scientific, Tucson AZ). Table 5.1 provides a list of all instrumentation with their specifications.

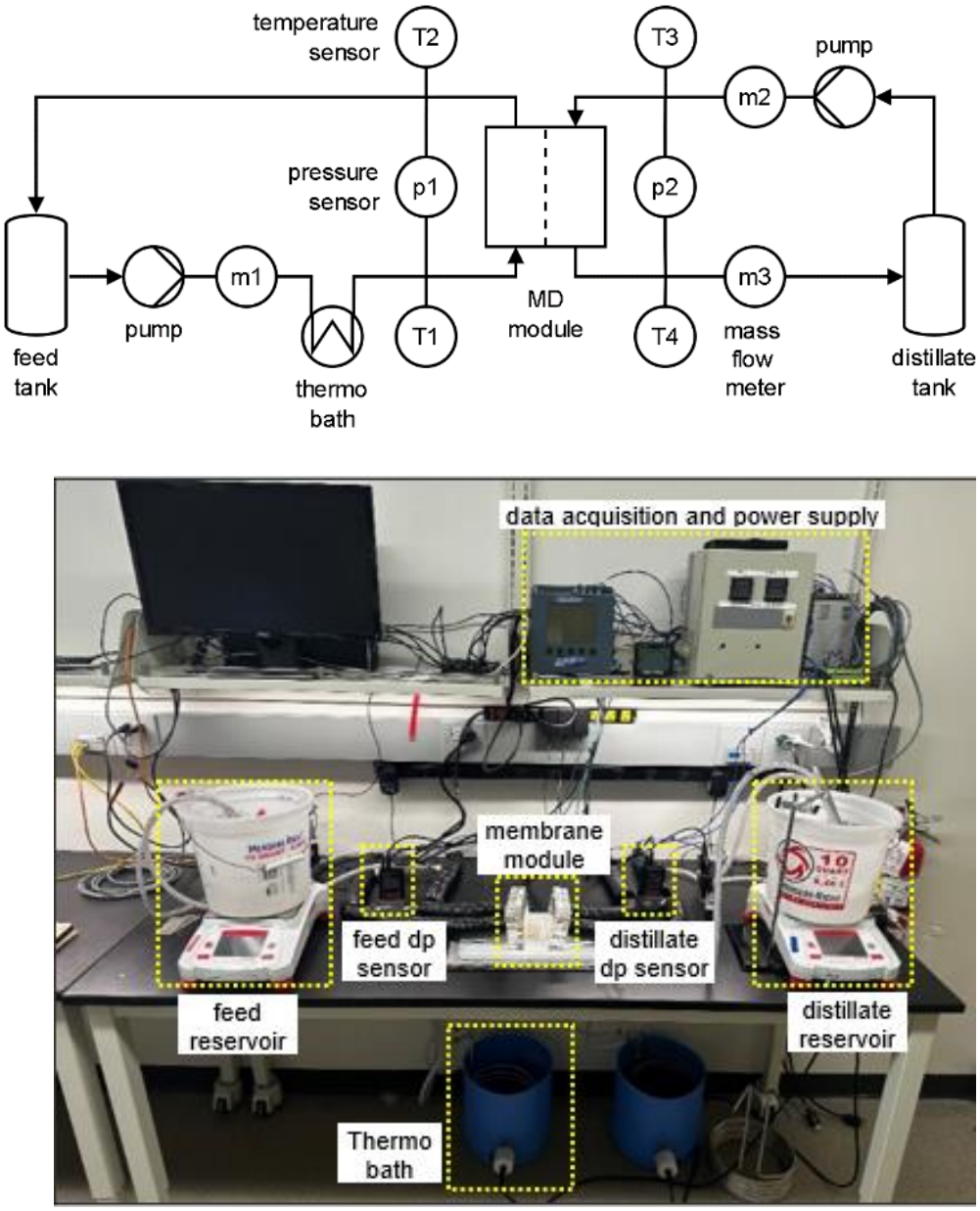

Figure 5.6 Schematic (top) and photo (bottom) of the laboratory bench MD test apparatus. The system includes flat sheet membrane housing with two channels supplied by feed and distillate circulation loops. The bench is instrumented with mass flow, temperature, and pressure sensors to allow for mass and energy balance analysis.

Table 5.1 Sensor and instrument specifications. Instrument numbers correspond to locations indicated on Figure 5.5.

Instrument	Supplier	Model #	Full Scale ± Uncertainty	Instrument Location
Feed mass flow controller	Alicat Scientific (Tucson, AZ)	KD100A-SCF-S0A-KA-2X	1 kg/h ± greater of 0.2 % full scale or 0.6 % reading	m1
Distillate mass flow controller	Alicat Scientific (Tucson, AZ)	KF-F200A-SCF-S0A-KA-2X	10 kg/h ± greater of 0.2 % full scale or 0.6 % reading	m2
Mass flow meter	Alicat Scientific (Tucson, AZ)	KD100A-SCF-S0A-KA-2X	1 kg/h ± 0.2 % full scale or 0.6 % reading	m3
Differential pressure sensor	Alicat Scientific (Tucson, AZ)	PS-30PSID-D/5P	1 bar ± 0.25 % full scale	p1, p2
Applied pressure controller	Alicat Scientific (Tucson, AZ)	PCS-100PSIG-D-PCA17/5P	21 bar ± 0.25 % full scale	p3
Temperature sensor	Noshok (Berea, OH)	800-200-1-1-8-8-040-6 RTD	93.33 ± 0.465 °C	T1, T2, T3, T4
Mass scale	OHAUS (Parsippany, NJ)	CS 200	200 ± 0.1g	S1, S2

5.3.2 Membrane Specifications

A commercial polytetrafluoroethylene (PTFE) membrane (Unlaminated CF042, Sterlitech, Auburn, WA) was selected for this study. The flat-sheet membrane had an effective surface area of 42 cm² (107 mm length × 39 mm width) and was installed in the transparent acrylic module. To achieve the desired flow velocities and ensure membrane support, shims were placed in both the feed and draw channels, which reduce the effective depth to 0.801 mm. Additionally, a 31-mil diamond-shaped spacer was placed in the feed channel to increase flow turbulence and prevent channel blockages. The module design allows for easy visualization and access, which facilitates cleaning and experimental monitoring. A summary of the membrane and module parameters is provided in Table 5.2.

Table 5.2 Membrane and module parameters.

Membrane properties	
Supplier	Sterlitech (Auburn, WA)
Material	polytetrafluoroethylene
Pore Size	0.45 μm
Thickness	21 – 51 μm
Water entry pressure	> 3.1 bar (45 psi)
Module properties	
Configuration	flat sheet
Dimensions	107 mm × 39 mm
Area	42 cm^2
Channel depth	0.801 mm
Feed channel spacer	31-mil diamond-shaped

5.3.3 Perturb-And-Observe Implementation

The proposed perturb-and-observe control system was implemented manually with the help of a commercial software package (FlowVision v2, Alicat Scientific, Tuscon AZ). This software was used to collect data from flow, pressure, and temperature sensors, and to calculate distillation rates, heat transfer rates, and specific heat and work inputs. Notably, the instantaneous result for specific heat input was smoothed using a moving average in order to filter noise and clearly distinguish the steady state response of the MD system. Then, using the perturb-and-observe logic, control signals to the mass flow and temperature controllers were updated. For the safety of the laboratory equipment, constraints were placed on the logic to prevent the feed circulation rate, distillate circulation rate, and feed temperature from exceeding 100 ml/min, 16 ml/min, and 60 °C, respectively, even when specific heat input could have been further reduced by exceeding these limits. The PID settings for the feed flow controller, distillate flow controller, and feed temperature controller were set to 10–2–0.

Supplementary Note 5.2 provides a schematic of how input signals from the sensors were processed to determine output signals to the controllers. Supplementary Note 5.3 provides a set of raw data along with sample calculations to show how equations (5.1)-

(5.8) were used in analysis and to show the propagation of experimental uncertainty. Table 5.3 lists the perturbations sizes and initials conditions that were used.

Table 5.3. Perturb-and-observe parameters.

Initial operating conditions	
Feed circulation rate $\dot{m}_F$	2500 g/h
Distillate circulation rate $\dot{m}_D$	600 g/h
Feed temperature T_F	30 °C
Perturbation size	
Step interval δt	900 s
Time per variable τ	3600 s
Steps per variable n	4
Feed circulation rate $\delta\dot{m}_F$	500 g/h
Distillate circulation rate $\delta\dot{m}_D$	100 g/h
Feed temperature δT_F	5 °C

5.3.4 Test Conditions

Performance of the proposed perturb-and-observe controller was evaluated for seawater desalination in a direct contact MD system. To approximate seawater, feed solution was prepared by dissolving sodium chloride (NaCl, >99% purity, Fisher Scientific, Hampton, NH) in deionized (DI) water at a concentration of 35 g/l. Deionized water was used to provide an initial volume of distillate solution that could be circulated, to which water flux across the membrane was added. Distillate was kept at ambient room temperature. A summary of test conditions is provided in Table 5.4.

Table 5.4 Experimental test conditions.

Test conditions	
Flow configuration	counter flow
Feed concentration	35.00 ± 0.04 g/l NaCl
Distillate concentration	DI water
Distillate temperature	20.0± 0.8 °C

5.4 Results

5.4.1 Control of MD Operating Conditions

Reducing the specific heat input of MD can be achieved with the coordinated adjustment of key operating conditions including the feed circulation rate, the distillate circulation rate, and the feed temperature. Circulation rates can be regulated with variable speed pumps controlled by mass flow controllers, and feed temperature can be managed by adjusting the rate of heat input with thermostatically controlled PID feedback. Figure 5.7 shows the response of the three operating conditions to step commands sent from their respective controllers. As shown, for both the feed and distillate circulation rates, the observed experimental values quickly and closely follow the command signals, with no observable transient period and only minor variations that remain within the bounds of measurement uncertainty. For the feed temperature however, the observed values lag significantly behind the step command. Only after ~ 10 minutes do actual conditions converge to the command. This is primarily due to large thermal capacitance of the feed volume, the power rating of the heat source, and the need for further PID tuning. Encouragingly, once reaching steady state, the feed temperature remains constant with only minor deviations within the range of experimental uncertainty.

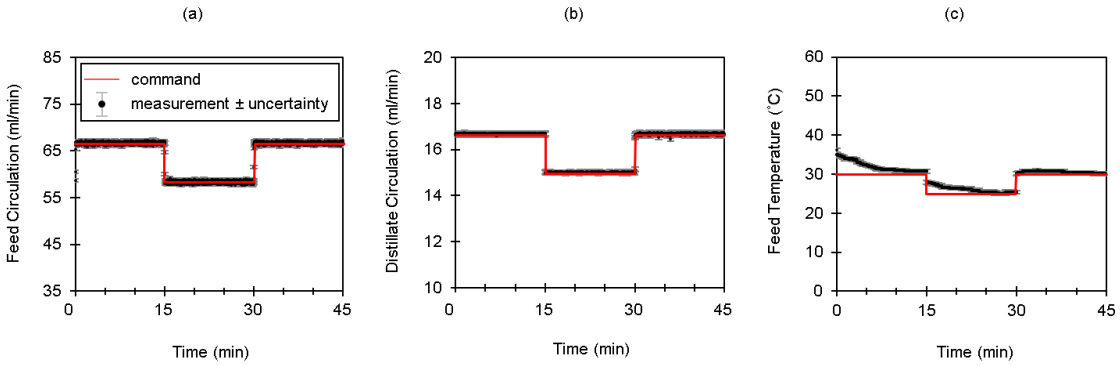

Figure 5.7 MD operating conditions in response to a series of step commands applied to their respective controllers. (a) Feed circulation is controlled by a mass flow controlled. (b) Distillate circulation is controlled by a mass flow controller. (c) Feed temperature is controlled by a thermally regulated bath.

5.4.2 Step Response of MD System

Adjusting the operating conditions of the MD system has an influence on both the rate of water flux across the porous hydrophobic membrane, as well as the rate of heat flux from hot feed to cool distillate. Usually, an increase in one is accompanied by an increase in the other, so reducing specific heat input is then a matter of ensuring that water flux increases by more than heat flux (or conversely, ensuring that heat flux decreases by more than water flux). To illustrate the effect that operating conditions have on the MD process, Figure 5.7 shows the response of key performance metrics to step changes in the operating conditions. Results are shown for key metrics such as water flux, heat flux, and specific heat input, which are obtained by analysis. Raw sensor data used in this analysis is provided in Supplementary Note 5.3.

First, Figure 5.8(a) shows the response to a change in feed circulation rate. As the feed flow is increased, both water flux and heat flux increase. This is expected, because higher circulation rates reduce the thickness of salt and temperature boundary layers and also reduce residence time, producing a more uniform temperature along the length of the

membrane from inlet to outlet. In this case, the increase in heat flux is more significant than the increase in water flux, and so the specific heat input is shown to increase. Therefore, such a step change would not be beneficial to energy efficiency.

Second, in Figure 5.8(b) we show the response of the MD system to a change in the distillate circulation rate. As the distillate flow is reduced both water flux and heat flux drop. This is expected for the same reason that higher circulation rates promoted higher flux, as explained above. In this case, the drop in water flux is more significant that then drop in heat flux and so we observe again an undesirable increase in the specific heat input.

Third, Figure 5.8(c) shows the response to a change in feed temperature. This response is somewhat obscured by the transients in the feed temperature and by noise in the MD sensor data. To assist in observing the macro trend of the response, we plot the average specific heat input, which is the cumulative average of the specific heat input starting from the instant when the step command is applied. In Figure 5.8(c) we see a very clear drop in the average specific heat input, indicating that drop in heat flux is greater than the drop in water flux. Such a beneficial step change would then be repeated by the controller.

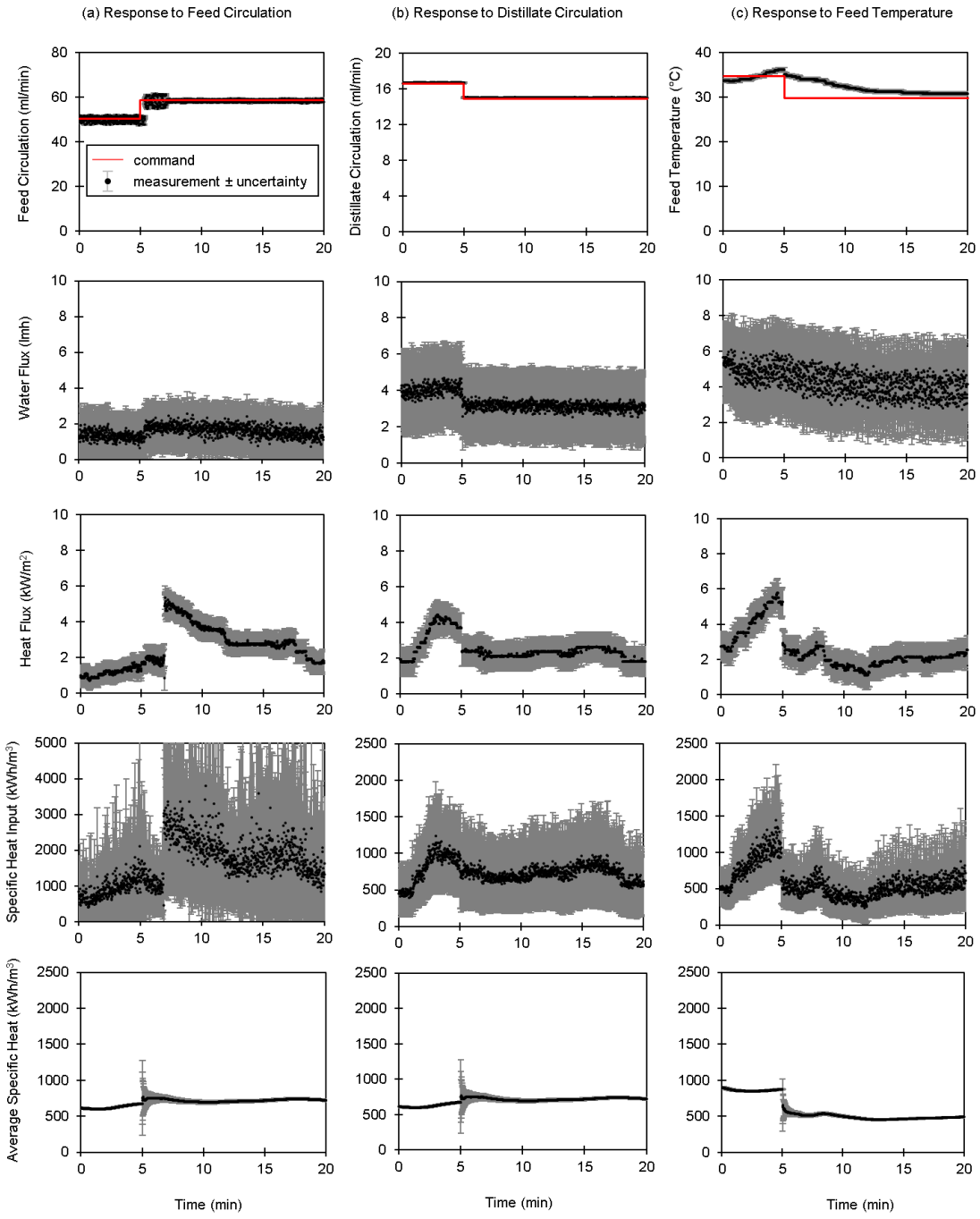

Figure 5.8 Real-time measurements of water flux, heat flux, specific heat input and average specific heat input in response to change in (a) feed flow rate, (b) distillate flow rate, and (c) feed temperature. Raw sensor data associated with these results is reported in Supplementary Note 5.4.

The average specific heat input signal is also helpful for implementation of the proposed feedback control algorithm, which involves the comparison of specific heat

input under new operating conditions to specific heat input under previous conditions. For such an algorithm to work reliably, it is necessary to have a signal that is stable and from which it is possible to interpret the effect of the operating conditions on performance so as to properly command the next step. The average signal for specific heat input also provides a simple metric against which to evaluate the time to reach steady state. Using this metric, a total of 37 tests were conducted with step changes to each of the three operating conditions, and the response was observed to determine how long it took for the change in average specific heat input to drop below 5 %. Figure 5.9 presents the results of this analysis showing the evaluation of steady-state times for the three operating parameters including feed flow rate, distillate flow rate, and feed temperature. Over 60% of the cases reached steady state within 10 minutes, and after 14 minutes, nearly 100% of the cases reached steady state (except for a small number of cases related to step changes in the distillate circulation rate). From this, we conclude that 15 minutes is an appropriate time interval at which to apply step commands in the proposed real-time tracker.

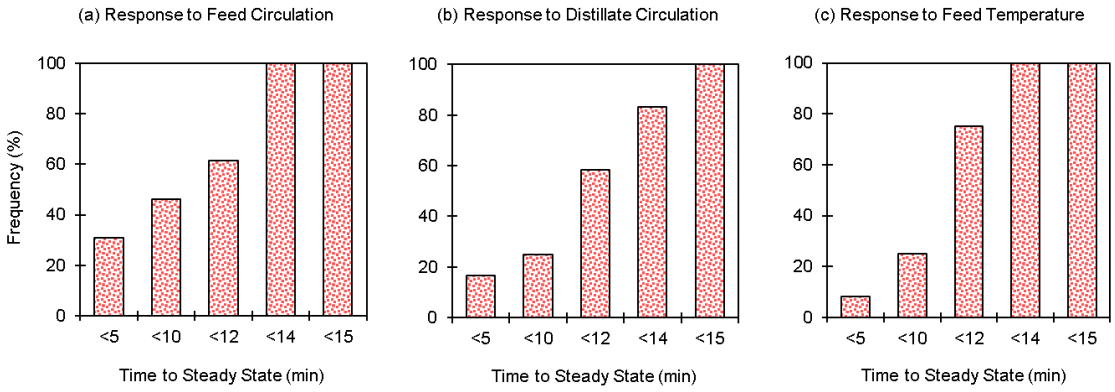

Figure 5.9 Time for average specific heat input to reach steady state (≤ 5% of the value at 15 mins) in response to step changes in (a) feed circulation rate, (b) distillate circulation rate, and (c) feed temperature.

5.4.3 Tracking Minimum Specific Heat Input in Real-Time

Figure 5.10 shows the successful implementation of the proposed real-time minimum energy tracker. Feed circulation rate, distillate circulation rate, and feed temperature are each varied in turn and a gradual decrease in specific heat input is observed over time. After a total of 23 step changes over 345 minutes (15 minute intervals per step), the specific heat input reached as low as 274 ± 9.69 kWh/m^3. This is an impressive 7× lower than the initial specific heat input. Also, this is significantly lower than the typical energy results reported in the literature, which commonly ranges from 600 to 1600 kWh/m^3 for direct contact MD [231], [232], [233], [234], [235]. Of course, these results from the literature are obtained with a variety of different membranes, each with different vapor permeability and thermal conductivity, with different module geometries, and different laboratory bench arrangements, making such energy comparisons somewhat difficult. But this variability only further emphasizes the value of this study, as the proposed control strategy can be widely applied to all kinds of different MD apparatus to reduce energy use relative to their baseline results. In this study, the lowest specific heat input is achieved when feed circulation, distillate circulation, and feed temperature reach 75.33 ± 0.45 mL/min, 16.5 ± 0.1 mL/min, and 30.011 ± 0.465 °C. Other MD apparatus will have their own unique combination of operating conditions that will approach minimum heat input. We also note that under these conditions, when specific heat input is lowest, the gain output ratio is maximized and reaches 2.6.

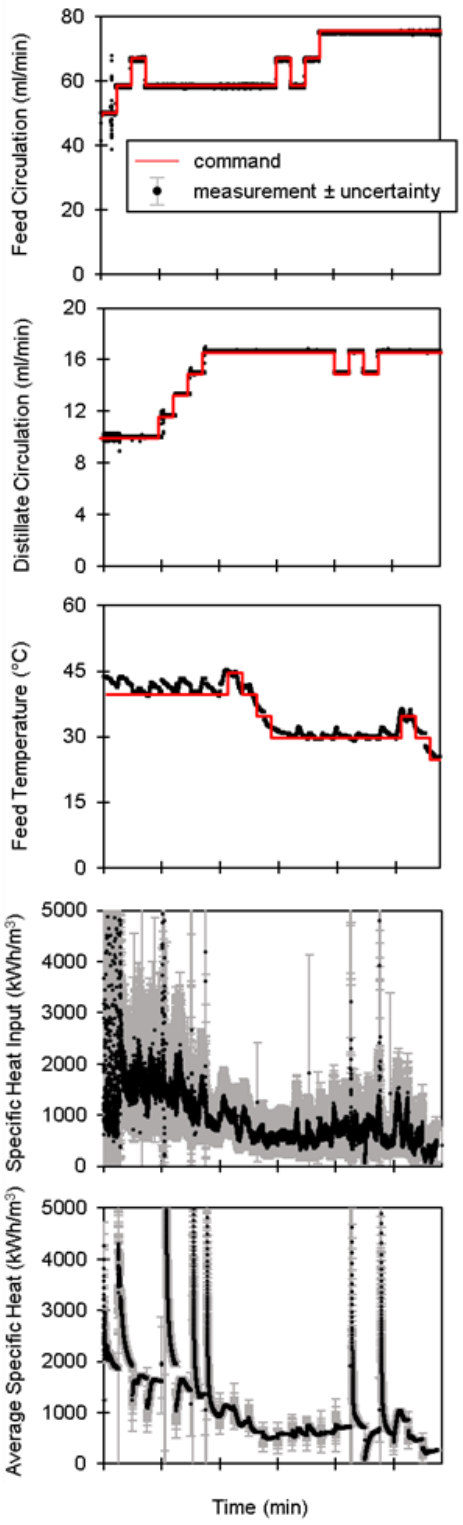

Figure 5.10 Demonstration of real-time MD controller finding the feed circulation rate, distillate circulation rate, and feed temperature that yield the lower specific heat input. Raw sensor data associated with these results is reported in Supplementary Note 5.5.

Figure 5.10 also shows short but very pronounced spikes at the start of most step changes, mainly when flow rates are adjusted. Changing the feed or distillate flow introduces transient disturbances that affect heat flux and water flux calculations. These fluctuations are more pronounced on the distillate side but gradually settle over time. Despite these transient spikes, the overall trend indicates a steady move toward lower specific energy consumption.

5.4.4 Effect on Specific Pump Work

While the focus of this paper is on the reduction of heat input per unit of water produced, it is interesting to consider the effect that this has on work. Work input is of course also a function of operating conditions, especially the circulation rates, which require pump work to increase. Figure 5.11 shows specific work throughout the previously discussed 345-minute test period. As shown, the response of specific work to changes in operating conditions does not follow the response of specific heat input, i.e. when one goes up or down, the other doesn't necessarily follow. Overall, we note a gradual increase in specific work, from an initial value of 0.0807 ± 0.0546 kWh/m3 to a final value of 0.2049 ± 0.1474 kWh/m3. Along the way, at time ~ 120 minutes, the lowest specific work of 0.0524 ± 0.0227 kWh/ m3 is encountered and passed by.

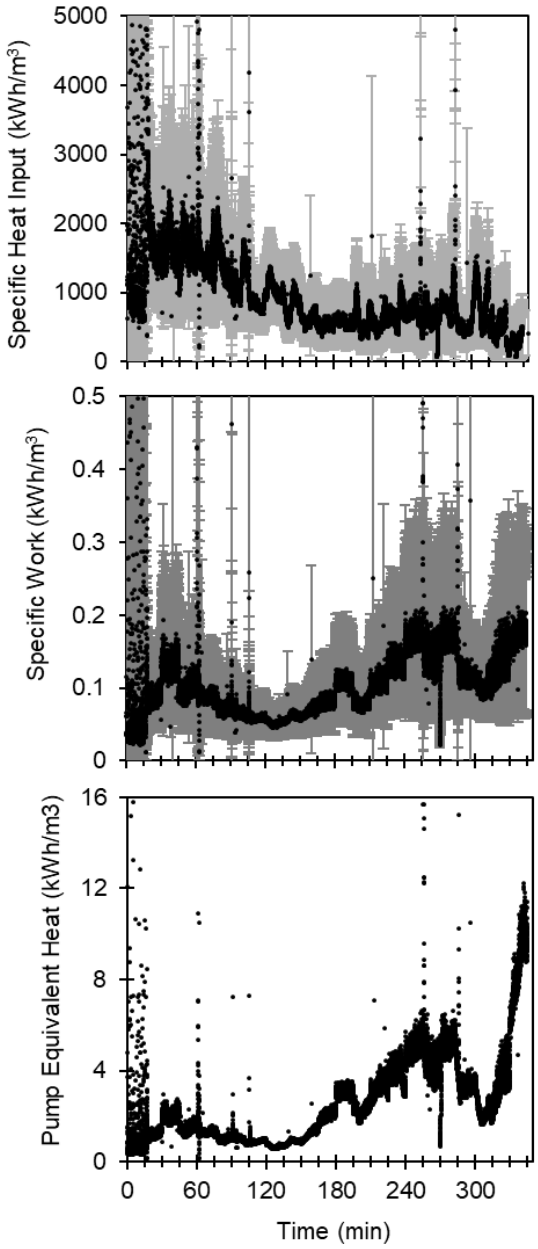

Figure 5.11 Changes in the specific work that is used for pumping as MD conditions are adjusted in real-time to reduce specific heat input. The thermal value of work is defined as work times the Carnot efficiency. Raw sensor data associated with these results is reported in Supplementary Note 5.5.

We might assume that such an increase in work input is small and even insignificant compared to the savings in heat input, which are several orders of magnitude greater. But technically, heat and work each have their own unique value (both thermodynamically

and economically) and the two cannot be directly compared. This is especially true when comparing work to low-grade heat, such as used in this study since feed temperature never exceeds 50 °C and eventually settles to 30 °C. In an effort to compare work and heat, we use the Carnot efficiency η_{Carnot} to define the thermal value of work $Q_{equivalent} = W / \eta_{Carnot} = W / (1 - T_D/T_F)$, where T_D and T_F are the distillate and feed temperatures respectively. Figure 11 includes a plot of the thermal value of the work that is associated with the pump work. As shown, the thermal equivalent of work mostly follows the plot for specific work, but it scales up as feed temperature is reduced. For example, at the final stage, when specific heat input is lowest and the feed temperature settles to ~30 °C, the work input has an equivalent thermal value of 12 kWh/m^3. This represents ~ 4% of the value of the heat input, which is 274 kWh/m^3 at its lowest point. The value of work input is therefore small, but perhaps not altogether insignificant, and in some cases might be quite important.

Future work might consider this and other related dynamics by considering alternative criteria for real-time tracking. For example, instead of tracking the lowest thermal energy point, it might be preferable to combine thermal energy input together with the thermal equivalent of pump work, and minimize these together. Other criteria such as cost, exergy, emissions, or some combination of these could also be minimized in real-time.

5.5 Conclusion

In the current study we experimentally demonstrated the concept of tracking minimum specific energy consumption of a membrane distillation system. The main operating parameters of an MD system including feed circulation rate, distillate circulation rate and

feed temperature were monitored, controlled and adjusted using a perturb and absorb control algorithm to approach the minimum specific heat input. It was shown that changing operating parameters, such as increasing feed temperature, involves inherent trade-offs. On the one hand, it improves the water flux, but on the other hand, at the same time it increases the thermal input required by the system. The relative significance of these advantages and disadvantages varies with other system conditions, such as the feed and distillate flow rates. A similar trend exists for adjusting flow rates; changing feed and distillate circulation rates can enhance water flux but may also increase the required energy of system due to increased pumping power and thermal energy input. Considering these trade-offs are aligned with our studies objective, identifying the conditions that reduce specific energy consumption. Through the conducted experiments, the system approached a minimum specific energy consumption of approximately 274 ± 9.69 kWh/m^3 after two full cycles of operating parameter adjustment which shows 80% reduction compared to the initial specific energy consumption. This value is also significantly lower than values typically reported in the literature for the specific heat input of MD systems. The optimal operating conditions corresponding to this point were a feed flow rate of approximately 75.33 ± 0.45 mL/min, a distillate flow rate of 16.5 ± 0.1 mL/min, and a feed temperature of around 30.011 ± 0.465 °C. This significant reduction of specific heat input shows the importance of adjusting operating variables in obtaining energy efficient systems.

5.6 Supplementary Note

5.6.1 Supplementary Note 5.1: Energy Balance of Direct Contact Membrane Distillation

The energy requirement for membrane distillation depends largely on the degree to which heat is recovered from brine and distillate and recycled back to the incoming feed. Below, we derive the energy requirements for a system configuration shown in Figure S5.1. In this case two heat exchangers are used to recover heat from the feed and distillate. All analysis assumes the system is perfectly insulated with no losses to the outside environment.

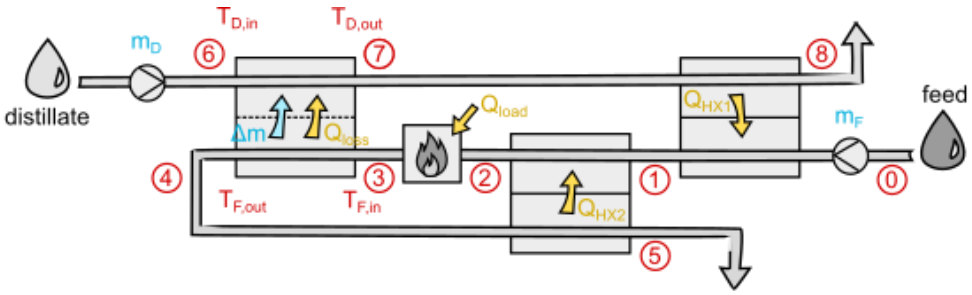

Figure S5.1 Schematic of the membrane distillation (MD) system including two heat exchangers for energy recovery from both the distillate and feed streams

Equation (S5.1) describes the energy balance of incoming feed through the first heat exchanger, where subscripts 0 and 1 show the inlet and outlet. As shown, the change in energy will be a function of the heat transfer $\dot{Q}_{HX1}$, and the result will be a change in the solution's enthalpy h.

$$\dot{E}_1 - \dot{E}_0 = \dot{m}_1 h_1 - \dot{m}_0 h_0 \quad \text{S5.1a}$$

$$\dot{E}_1 - \dot{E}_0 = \dot{Q}_{HX1} \quad \text{S5.1b}$$

$$\dot{Q}_{HX1} = \dot{m}_F (h_1 - h_0) \quad \text{S5.1c}$$

Equation (S5.2) describes the energy balance of incoming feed through the second heat exchanger, where subscripts 1 and 2 denote the inlet and outlet. As shown, the

change in energy will be a function of the heat transfer $\dot{Q}_{HX2}$, and the result will be a change in the solution's enthalpy h.

$$\dot{E}_2 - \dot{E}_1 = \dot{m}_2\, h_2 - \dot{m}_1\, h_1 \quad \text{S5.2a}$$

$$\dot{E}_2 - \dot{E}_1 = \dot{Q}_{HX2} \quad \text{S5.2b}$$

$$\dot{Q}_{HX2} = \dot{m}_F\, (h_2 - h_1) \quad \text{S5.2c}$$

Equation (S5.3) describes the energy balance of feed (also referred to as brine) through the heater, where subscripts 2 and 3 denote the inlet and outlet. As shown, the change in energy will be a function of the heat input $\dot{Q}_{load}$, and the result will be a change in the solution's enthalpy h.

$$\dot{E}_3 - \dot{E}_2 = \dot{m}_3\, h_3 - \dot{m}_2\, h_2 \quad \text{S5.3a}$$

$$\dot{E}_3 - \dot{E}_2 = \dot{Q}_{load} \quad \text{S5.3b}$$

$$\dot{Q}_{load} = \dot{m}_F\, (h_3 - h_2) \quad \text{S5.3c}$$

Equation (S5.4) describes the energy balance of feed through the MD unit, where subscripts 3 and 4 denote the inlet and outlet. As shown, the change in energy will be a function of the heat loss across the membrane $\dot{Q}_{loss}$ together with the mass transfer $\Delta\dot{m}$ and its associated enthalpy $\dot{H}$. Although temperature and hence specific enthalpy will change from inlet to outlet, the total enthalpy can be approximated by assuming that the average specific enthalpy $\bar{h} \approx h_3$.

$$\dot{E}_4 - \dot{E}_3 = \dot{m}_4\, h_4 - \dot{m}_3\, h_3 \quad \text{S5.4a}$$

$$\dot{E}_4 - \dot{E}_3 = -\dot{Q}_{loss} - \dot{H} \quad \text{S5.4b}$$

$$\dot{E}_4 - \dot{E}_3 = -\dot{Q}_{loss} - \int_0^{\Delta\dot{m}} h \, d\dot{m} \quad \text{S5.4c}$$

$$\dot{E}_4 - \dot{E}_3 \approx -\dot{Q}_{loss} - \Delta\dot{m} \, h_4 \quad \text{S5.4d}$$

$$Q_{loss} \approx (\dot{m}_F - \Delta\dot{m}) \, (h_3 - h_4) \quad \text{S5.4e}$$

Equation (S5.5) describes the energy balance of outgoing feed through the second heat exchanger, where subscripts 4 and 5 denote the inlet and outlet. As shown, the change in energy will be a function of the heat transfer $\dot{Q}_{HX2}$, and the result will be a change in the solution's enthalpy h.

$$\dot{E}_5 - \dot{E}_4 = \dot{m}_5 \, h_5 - \dot{m}_4 \, h_4 \quad \text{S5.5a}$$

$$\dot{E}_5 - \dot{E}_4 = -\dot{Q}_{HX2} \quad \text{S5.5b}$$

$$\dot{Q}_{HX2} = (\dot{m}_F - \Delta\dot{m}) \, (h_4 - h_5) \quad \text{S5.5c}$$

Equation (S5.6) describes the energy balance of distillate through the MD unit, where subscripts 6 and 7 denote the inlet and outlet. As shown, the change in energy will be a function of the heat received across the membrane $\dot{Q}_{loss}$ together with the mass transfer $\Delta\dot{m}$ and its associated enthalpy $\dot{H}$.

$$\dot{E}_7 - \dot{E}_6 = \dot{m}_7 \, h_7 - \dot{m}_6 \, h_6 \quad \text{S5.6a}$$

$$\dot{E}_7 - \dot{E}_6 = \dot{Q}_{loss} + \dot{H} \quad \text{S5.6b}$$

$$\dot{E}_7 - \dot{E}_6 = \dot{Q}_{loss} + \int_0^{\Delta\dot{m}} h \, d\dot{m} \quad \text{S5.6c}$$

$$\dot{E}_7 - \dot{E}_6 \approx \dot{Q}_{loss} + \Delta\dot{m} \, h_3 \quad \text{S5.6d}$$

$$\dot{Q}_{loss} \approx (\dot{m}_D + \Delta\dot{m}) \, h_7 - \dot{m}_D \, h_6 - \Delta\dot{m} \, h_3 \quad \text{S5.6e}$$

Equation (S5.7) describes the energy balance of outgoing distillate through the first heat exchanger, where subscripts 7 and 8 denote the inlet and outlet. As shown, the change in energy will be a function of the heat transfer $\dot{Q}_{HX1}$, and the result will be a change in the solution's enthalpy h.

$$\dot{E}_8 - \dot{E}_7 = \dot{m}_8\, h_8 - \dot{m}_7\, h_7 \qquad \text{S5.7a}$$

$$\dot{E}_8 - \dot{E}_7 = -\dot{Q}_{HX1} \qquad \text{S5.7b}$$

$$\dot{Q}_{HX1} = (\dot{m}_D + \Delta\dot{m})(h_7 - h_8) \qquad \text{S5.7c}$$

In addition, the energy balance for heat exchangers 1 and 2 can be described in terms of effectiveness ε and the maximum heat transfer possible between the hot and cold fluids $\dot{Q}_{max}$, as shown in equations (S5.8)-(S5.10). In heat exchanger 1, the maximum heat transfer will be limited by the fluid that has a lesser flow rate between either $\dot{m}_D + \Delta\dot{m}$ or $\dot{m}_F$. In our case, the distillate has a lower flow rate and therefore a lower thermal capacitance. In heat exchanger 2, the maximum heat transfer will be limited by the hot brine because it has lower mass $\dot{m}_F - \Delta\dot{m} < \dot{m}_F$. Finally, treating the liquid desiccant as incompressible and the specific heat capacity cp as constant, we can express the change in temperature T as a change in enthalpy h.

$$\dot{Q}_{HX} = \varepsilon\, \dot{Q}_{max} \qquad \text{S5.8}$$

$$\dot{Q}_{HX1} = \varepsilon_1\, (\dot{m}_D + \Delta\dot{m})\, cp\, (T_7 - T_0) \qquad \text{S5.9a}$$

$$\dot{Q}_{HX1} = \varepsilon_1\, (\dot{m}_D + \Delta\dot{m})\, (h_7 - h_0) \qquad \text{S5.9b}$$

$$\dot{Q}_{HX2} = \varepsilon_2\, (\dot{m}_F - \Delta\dot{m})\, cp\, (T_4 - T_1) \qquad \text{S5.10a}$$

$$\dot{Q}_{HX2} = \varepsilon_2\, (\dot{m}_F - \Delta\dot{m})\, (h_4 - h_1) \qquad \text{S5.10b}$$

Finally, combining equations (S5.1), (S5.2), (S5.3), (S5.9), and (S5.10) the heating load can be expressed as a function of properties at the inlet and outlet of the MD unit as shown in equation (S5.11).

$$\dot{Q}_{load} = \dot{m}_F\, h_3 - \dot{m}_F\, h_2 \qquad \text{S5.3}$$

$$\dot{Q}_{load} = \dot{m}_F\, h_3 - \left[\dot{m}_F\, h_1 + \dot{Q}_{HX2}\right] \qquad \text{S5.2+S5.3}$$

$$\dot{Q}_{load} = \dot{m}_F\, h_3 - \left[\dot{m}_F\, h_0 + \dot{Q}_{HX1}\right] - \dot{Q}_{HX2} \qquad \text{S5.1+S5.2+S5.3}$$

$$\dot{Q}_{load} = \dot{m}_F\, h_3 - \dot{m}_F\, h_0 - [\varepsilon_1\, (\dot{m}_D + \Delta\dot{m})\, (h_7 - h_0)] - [\varepsilon_2\, (\dot{m}_F - \Delta\dot{m})\, (h_4 - h_1)] \qquad \text{S5.1+S5.2+S5.3+S5.9+S5.10}$$

$$\dot{Q}_{load} = \dot{m}_F\, h_3 - \dot{m}_F\, h_0 - \varepsilon_1\, (\dot{m}_D + \Delta\dot{m})\, h_7 + \varepsilon_1\, (\dot{m}_D + \Delta\dot{m})\, h_0 - \varepsilon_2\, (\dot{m}_F - \Delta\dot{m})\, h_4 + \varepsilon_2\, (\dot{m}_F - \Delta\dot{m})\, \left[h_0 + \frac{Q_{HX1}}{\dot{m}_F}\right] \qquad \text{S5.1+S5.2+S5.3+S5.9+S5.10}$$

$$\dot{Q}_{load} = \dot{m}_F\, h_3 - \dot{m}_F\, h_0 - \varepsilon_1\, (\dot{m}_D + \Delta\dot{m})\, h_7 + \varepsilon_1\, (\dot{m}_D + \Delta\dot{m})\, h_0 - \varepsilon_2\, (\dot{m}_F - \Delta\dot{m})\, h_4 + \varepsilon_2\, (\dot{m}_F - \Delta\dot{m})\, h_0 + \varepsilon_2\, \left(1 - \frac{\Delta\dot{m}}{\dot{m}_F}\right)\, [\varepsilon_1\, (\dot{m}_D + \Delta\dot{m})\, (h_7 - h_0)] \qquad \text{S5.1+S5.2+S5.3+S5.9+S5.10}$$

$$\dot{Q}_{load} = \dot{m}_F\, h_3 - \dot{m}_F\, h_0 - \varepsilon_1\, (\dot{m}_D + \Delta\dot{m})\, h_7 + \varepsilon_1\, (\dot{m}_D + \Delta\dot{m})\, h_0 - \varepsilon_2\, (\dot{m}_F - \Delta\dot{m})\, h_4 + \varepsilon_2\, (\dot{m}_F - \Delta\dot{m})\, h_0 + \varepsilon_1\, (\dot{m}_D + \Delta\dot{m})\, \varepsilon_2\, \left(1 - \frac{\Delta m}{m_F}\right) h_7 - \varepsilon_1\, (\dot{m}_D + \Delta\dot{m})\, \varepsilon_2\, \left(1 - \frac{\Delta\dot{m}}{\dot{m}_F}\right) h_0 \qquad \text{S5.11a}$$

$$\dot{Q}_{load} = \dot{m}_F\,(h_3 - h_0) - \varepsilon_1\,(\dot{m}_D + \Delta\dot{m})\,(h_7 - h_0) - \varepsilon_2\,(\dot{m}_F - \Delta\dot{m})\,(h_4 - h_0) + \varepsilon_1\,(\dot{m}_D + \Delta\dot{m})\,\varepsilon_2\left(1 - \frac{\Delta\dot{m}}{\dot{m}_F}\right)(h_7 - h_0) \quad \text{S5.11b}$$

$$\dot{Q}_{load} = \dot{m}_F\,(h_3 - h_0) + \varepsilon_2\,(\dot{m}_F - \Delta\dot{m})\,(h_4 - h_0) + \varepsilon_1\,(\dot{m}_D + \Delta\dot{m})\left(\varepsilon_2\left(1 - \frac{\Delta\dot{m}}{\dot{m}_F}\right) - 1\right)(h_7 - h_0) \quad \text{S5.11c}$$

Treating the fluids as incompressible with some average specific heat capacity cp, we can define the thermal load as a function of the feed and distillate temperatures at the inlet and outlet of the MD unit $T_{F,in}$, $T_{F,out}$, $T_{D,in}$ and $T_{D,out}$, and the ambient temperature $T_{ambient}$.

$$\dot{Q}_{load} = \dot{m}_F\,cp\,(T_{F,in} - T_{ambient}) + \varepsilon_2\,(\dot{m}_F - \Delta\dot{m})\,cp\,(T_{F,out} - T_{ambient}) + \varepsilon_1\,(\dot{m}_D + \Delta\dot{m})\left(\varepsilon_2\left(1 - \frac{\Delta\dot{m}}{\dot{m}_F}\right) - 1\right)cp\,(T_{D,out} - T_{ambient}) \quad \text{S5.11d}$$

The expression can be greatly simplified in the special case where both heat exchangers are ideal with effectiveness $\varepsilon_1 = \varepsilon_2 = 1$, and where the feed flow rate is much greater than the mass of water transferred across the membrane $\dot{m}_F \gg \Delta\dot{m}$ (i.e. low recovery ratio). The simplified expression is shown in equation (S5.12). This simplified expression is commonly used throughout the literature to calculate the thermal load of MD.

$$\dot{Q}_{load} = \dot{m}_F\,cp\,(T_{F,in} - T_{F,out}) \quad \text{S5.12}$$

In some cases, it may be preferable to express the heating load in terms of the inlet and outlet distillate temperature. To do this, we combine the previous result from equation (S5.11) with the energy balance equations of the MD unit, equations (S5.4) and (S5.6).

$$\dot{Q}_{load} = \dot{m}_F\, h_3 - \dot{m}_F\, h_0 + \varepsilon_2\, (\dot{m}_F - \Delta\dot{m})\, (h_4 - h_0) + \varepsilon_1\, (\dot{m}_D + \Delta\dot{m})\, \left(\varepsilon_2\, \left(1 - \frac{\Delta\dot{m}}{\dot{m}_F}\right) - 1\right)\, (h_7 - h_0) \quad \text{S5.11c}$$

$$\dot{Q}_{load} = [(\dot{m}_D + \Delta\dot{m})\, h_7 - \dot{m}_D\, h_6 - (\dot{m}_F - \Delta\dot{m})\, h_4] - \dot{m}_F\, h_0 + \varepsilon_2\, (\dot{m}_F - \Delta\dot{m})\, (h_4 - h_0) + \varepsilon_1\, (\dot{m}_D + \Delta\dot{m})\, \left(\varepsilon_2\, \left(1 - \frac{\Delta\dot{m}}{\dot{m}_F}\right) - 1\right)\, (h_7 - h_0) \quad \text{S5.4+S5.6+S5.11}$$

Then, assuming that we have ideal heat exchangers $\varepsilon_1 = \varepsilon_2 = 1$, and relatively small quantities of water collected across the membrane $\dot{m}_F \gg \Delta\dot{m}$ and $\dot{m}_D \gg \Delta\dot{m}$, we obtain the simplified expression in equation (5.13). This simplified expression is commonly used throughout the literature to calculate the thermal load of MD.

$$\dot{Q}_{load} = \dot{m}_D\, cp\, \left(T_{D,out} - T_{D,in}\right) \quad \text{S5.13}$$

5.6.2 Supplementary Note 5.2: Analysis of Sensor Data

Figure S5.2 shows how experimental data from 10 sensors on the laboratory bench are used to calculate the specific heat and specific work input of the MD system. Sensors include temperature, pressure and mass flow at the MD inlets and outlet, $T_{F,in}$, $T_{F,out}$, $T_{D,in}$, $T_{D,out}$, $p_{F,in}$, $p_{F,out}$, $p_{D,in}$, $p_{D,out}$, $\dot{m}_{F,in}$, $\dot{m}_{D,in}$, and $\dot{m}_{D,out}$. Results for specific heat

are input to the perturb and observe algorithm which then updates command signals sent to the operating conditions.

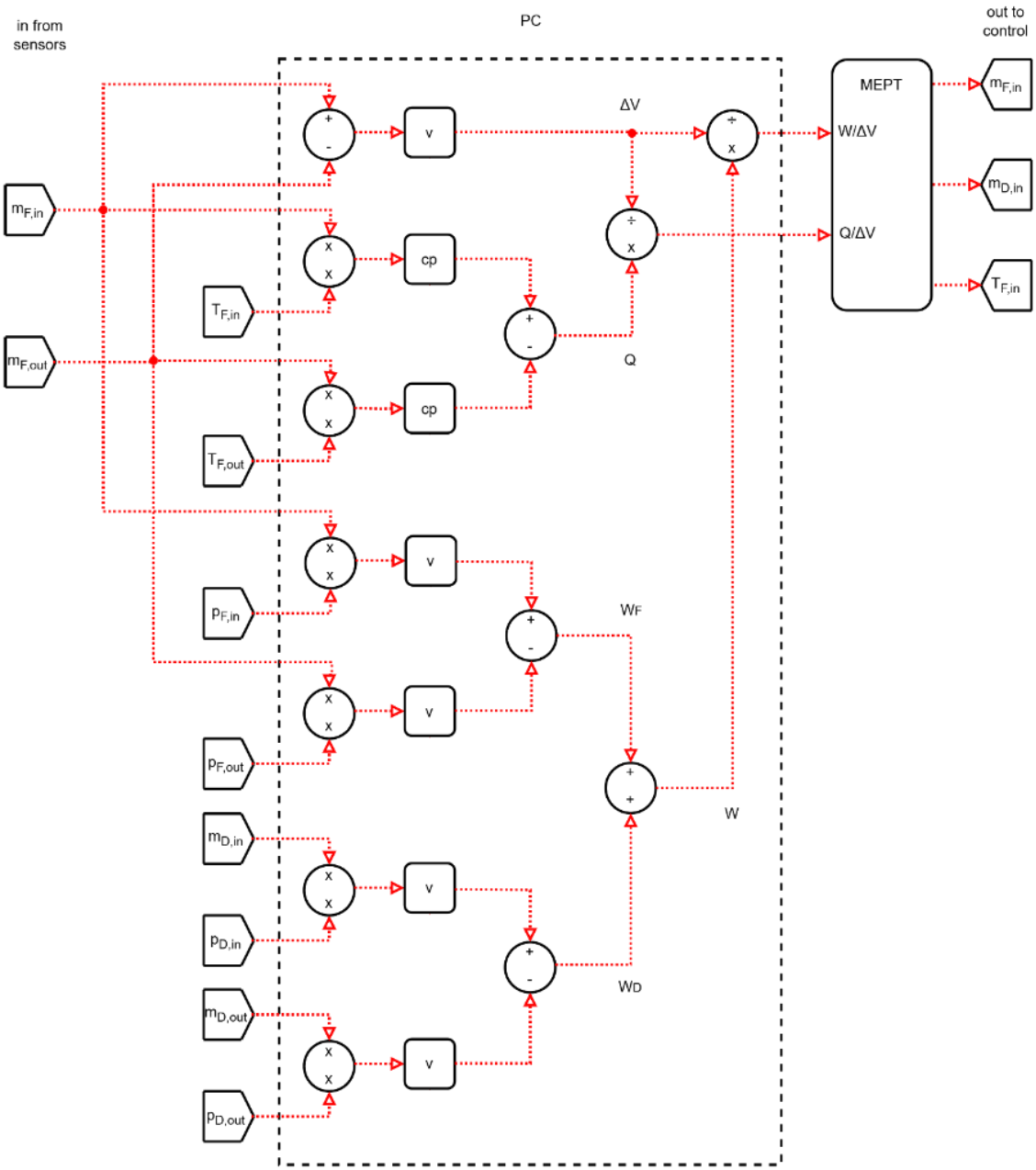

Figure S5.2. Real-time feedback loop for evaluating specific heat input and utilizing minimum energy tracker to adjust feed flow rate, distillate flow rate, and feed temperature

5.6.3 Supplementary Note 5.3: Sample Test Results, Data Analysis, and Propagation of Uncertainty

Table S5.1 provides a sample of the collected sensor data, along with analysis and propagation of experimental uncertainty.

Table S5.1 Analysis of sensor data with propagation of uncertainty.

Parameter	Value	Measurement or Analysis
Inlet feed temperature $T_{F,in}$	39.344 ± 0.465 °C	Temperature transmitter, 800-200-1-1-8-8-040-6 RTD, Noshok (Berea, OH), 200 ± 0.837 °F
Outlet feed temperature $T_{F,out}$	34.850 ± 0.465 °C	Temperature transmitter, 800-200-1-1-8-8-040-6 RTD, Noshok (Berea, OH), 200 ± 0.837 °F
Inlet distillate temperature $T_{D,in}$	20.638 ± 0.465 °C	Temperature transmitter, 800-200-1-1-8-8-040-6 RTD, Noshok (Berea, OH), 200 ± 0.837 °F
Outlet distillate temperature $T_{D,out}$	31.416 ± 0.465 °C	Temperature transmitter, 800-200-1-1-8-8-040-6 RTD, Noshok (Berea, OH), 200 ± 0.837 °F
Inlet feed flow rate $\dot{m}_{F,in}$	41.828 ± 0.025 ml/min	Feed mass flow controller, KD100A-SCF-S0A-KA-2X, Alicat Scientific (Tucson, AZ), 1 kg/h ± greater of 0.2 % full scale or 0.6 % reading
Inlet distillate flow rate $\dot{m}_{D,in}$	9.771 ± 0.059 ml/min	Distillate mass flow controller, KF-F200A-SCF-S0A-KA-2X, Alicat Scientific (Tucson, AZ), 10 kg/h ± greater of 0.2 % full scale or 0.6 % reading
Outlet distillate flow rate $\dot{m}_{D,out}$	10.119 ± 0.060 ml/min	Mass flow meter, KD100A-SCF-S0A-KA-2X, Alicat Scientific (Tucson, AZ), 1 kg/h ± 0.2 % full scale or 0.6 % reading
Feed pressure drop Δp_F	0.117 ± 0.0375 psi	Differential pressure sensor, PS-30PSID-D/5P, Alicat Scientific (Tucson, AZ), 15 ± 0.375 psi
Distillate pressure drop Δp_D	0.031 ± 0.0375 psi	Differential pressure sensor, PS-30PSID-D/5P, Alicat Scientific (Tucson, AZ), 15 ± 0.375 psi
Outlet distillate pressure $P_{D,out}$	5.24 ± 0.75 psi	Pressure controller, PCS-100PSIG-D-PCA17/5P, Alicat Scientific (Tucson, AZ), 300 ± 0.75 psi
Water distillation rate		
Water flux J_w	4.971 ± 1.205 lmh	$J_w = \frac{\dot{m}_{D,out} - \dot{m}_{D,in}}{A}$, $\delta J_w = \sqrt{\left(\delta\dot{m}_{D,out}\right)^2 + \left(\delta\dot{m}_{D,in}\right)^2}$
Thermal energy requirements		
Heat flux from feed $\dot{Q}_F$	13.109 ± 1.919 W	$\dot{Q}_F = \dot{m}_{F,in}\, cp\, (T_{F,in} - T_{F,out})$, $\delta Q_F = \left[\left(cp\,(T_{F,in} - T_{F,out})\,\delta\dot{m}_{F,in}\right)^2 + \left(\dot{m}_{F,in}\, cp\, \delta T_{F,in}\right)^2 + \left(-\dot{m}_{F,in}\, cp\, \delta T_{F,in}\right)^2\right]^{1/2}$

Table S5.1 - continued

Parameter	Value	Measurement or Analysis
Heat flux to distillation $\dot{Q}_D$	7.344 ± 0.450 W	$\dot{Q}_D = \dot{m}_{D,out}\, cp\, (T_{D,out} - T_{D,in})$, $\delta Q_D = \left[(cp\,(T_{D,out} - T_{D,in})\,\delta\dot{m}_{D,out})^2 + (\dot{m}_{D,out}\, cp\, \delta T_{D,out})^2 + (-\dot{m}_{D,out}\, cp\, \delta T_{D,in})^2\right]^{1/2}$
Specific heat input q	627.850 ± 177.885 kWh/m^3	$\dot{q} = \frac{\dot{Q}_D/A}{J_w}$, $\delta\dot{q} = \sqrt{\left(\frac{1}{J_w}\,\delta\dot{Q}_D\right)^2 + \left(\frac{\dot{Q}_D}{{J_w}^2}\,\delta J\right)^2}$
Gain output ratio GOR	1.062±0.300	$GOR = \frac{\dot{Q}_D}{\Delta H}$, $\delta GOR = \left(\frac{\Delta H}{{\dot{Q}_D}^2}\right)\delta\dot{Q}_D$ where ΔH =667 kWh/m^3
Mechanical energy requirements		
Feed pump work $\dot{W}_F$	54.865×10^{-5} ± 18.027×10^{-5} W	$\dot{W}_F = \dot{m}_F\, v\, (p_{F,in} - p_{F,out})$, $\delta\dot{W}_F = \sqrt{(v\,\Delta p_F\,\delta\dot{m}_F)^2 + (\dot{m}_F\, v\,\delta\Delta p_F)^2}$ where v = 0.001 m^3/kg
Distillate pump work $\dot{W}_D$	3.481×10^{-5} ± 4.210×10^{-5} W	$\dot{W}_D = \dot{m}_D\, v\, (p_{D,in} - p_{D,out})$, $\delta\dot{W}_D = \sqrt{(v\,\Delta p_D\,\delta\dot{m}_D)^2 + (\dot{m}_D\, v\,\delta\Delta p_D)^2}$ where v = 0.001 m3/kg
Specific work input w	0.027 ± 0.011 kWh/m^3	$\dot{w} = \frac{\dot{W}_F + \dot{W}_D}{J_w\, A}$, $\delta\dot{w} = \sqrt{\left(\frac{\delta\dot{W}_F}{J_w}\right)^2 + \left(\frac{\delta\dot{W}_D}{J_w}\right)^2 + \left(\frac{(\dot{W}_F + \dot{W}_D)\,\delta J_w}{{J_w}^2}\right)^2}$

5.6.4 Supplementary Note 5.4: Step Response of MD System

In the Results section 5.4.2, Figure 5.8 shows the response of key performance metrics to step changes in the operating conditions, including a change in feed circulation rate, distillate circulation rate, and feed temperature. Results are shown for key metrics such as water flux, heat flux, and specific heat input, which are obtained by analysis. Here in in Figures S5.3, S5.4, and S5.5 we report raw sensor data that was used in this analysis.

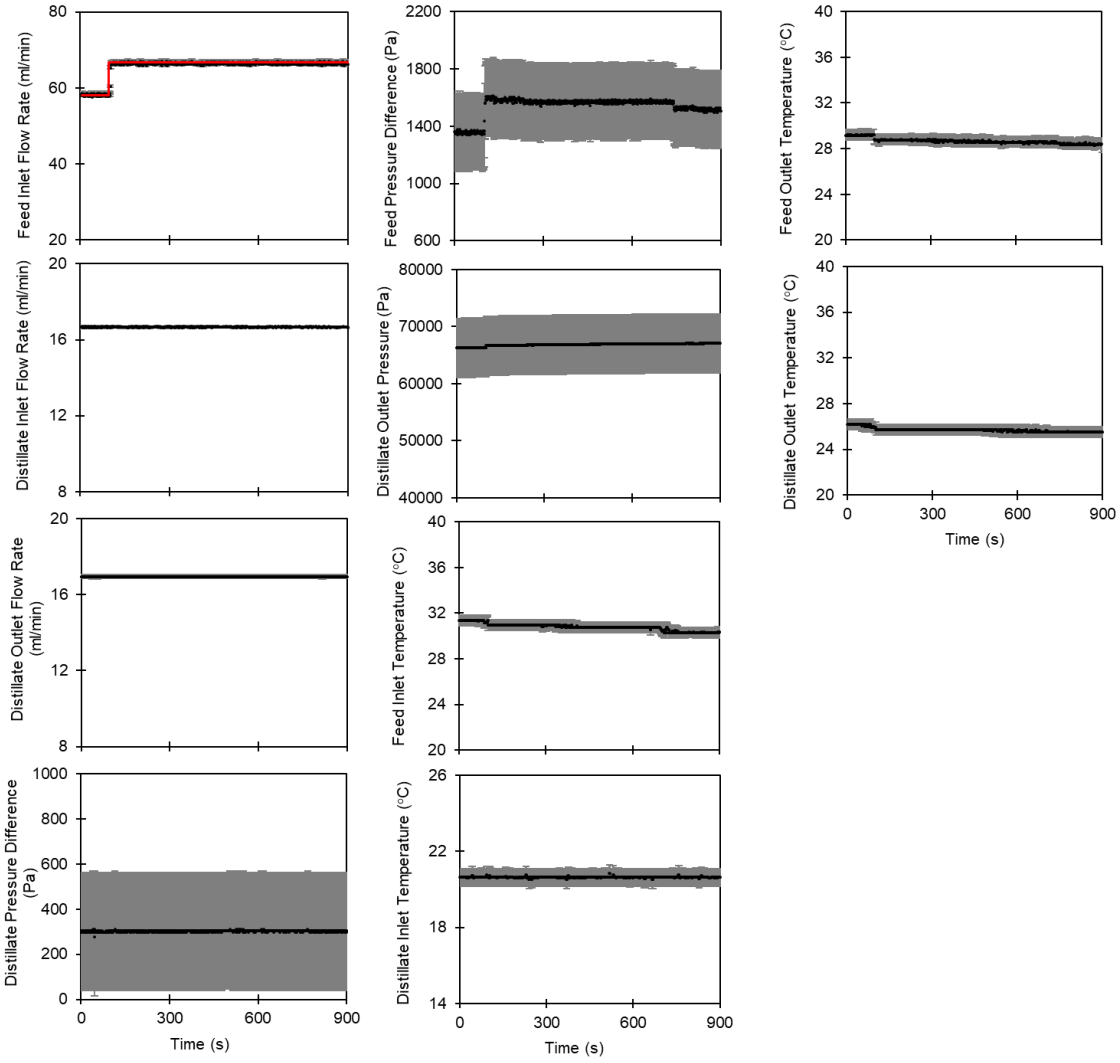

Figure S5.3 Raw sensor data used to prepare Figures 5.8(a), which shows the response of the MD system to a step change in feed circulation.

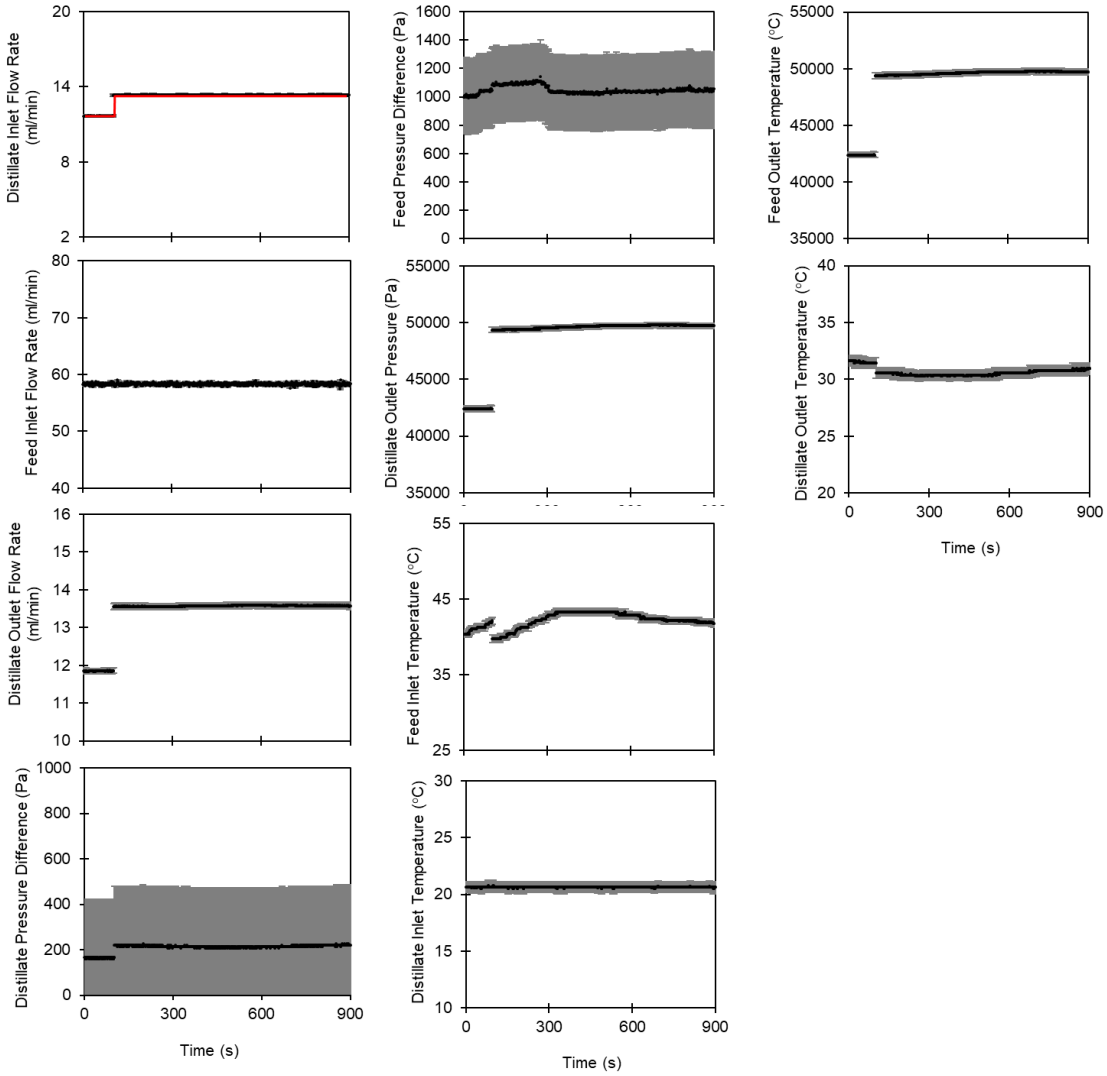

Figure S5.4 Raw sensor data used to prepare Figures 5.8(b), which shows the response of the MD system to a step change in distillate circulation.

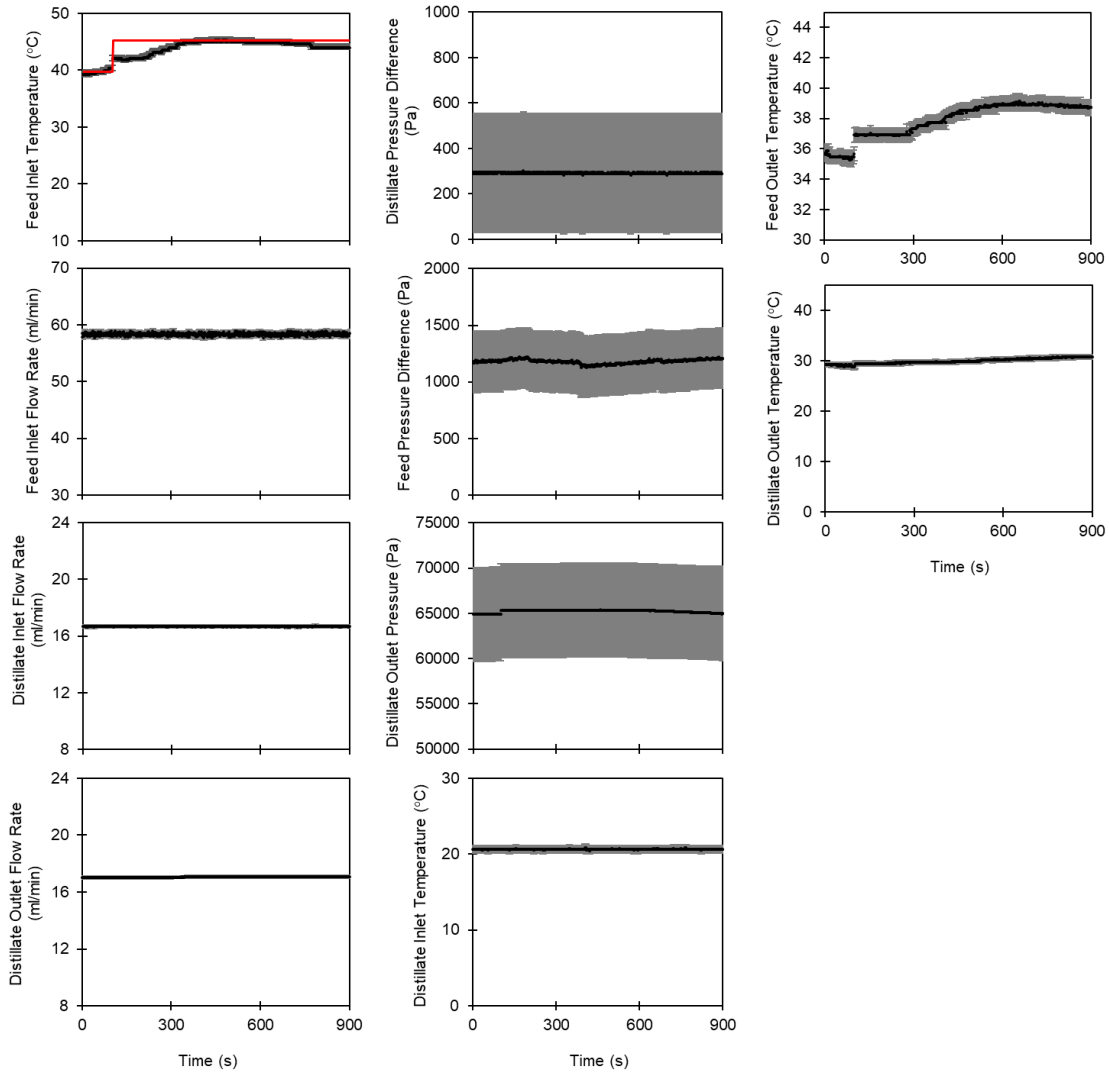

Figure S5.5 Raw sensor data used to prepare Figures 5.8(c), which shows the response of the MD system to a step change in feed temperature.

5.6.5 Supplementary Note 5.5: Tracking Minimum Specific Heat Input in Real-Time

In the Results sections 5.4.3 and 5.4.4, Figures 5.10 and 5.11 show the successful implementation of the proposed real-time tracker with specific thermal energy input steadily decreasing in response to coordinated changes in feed circulation rate, distillate circulation rate, and feed temperature. Here in Figures S5.6 we report raw sensor data that was used in this analysis.

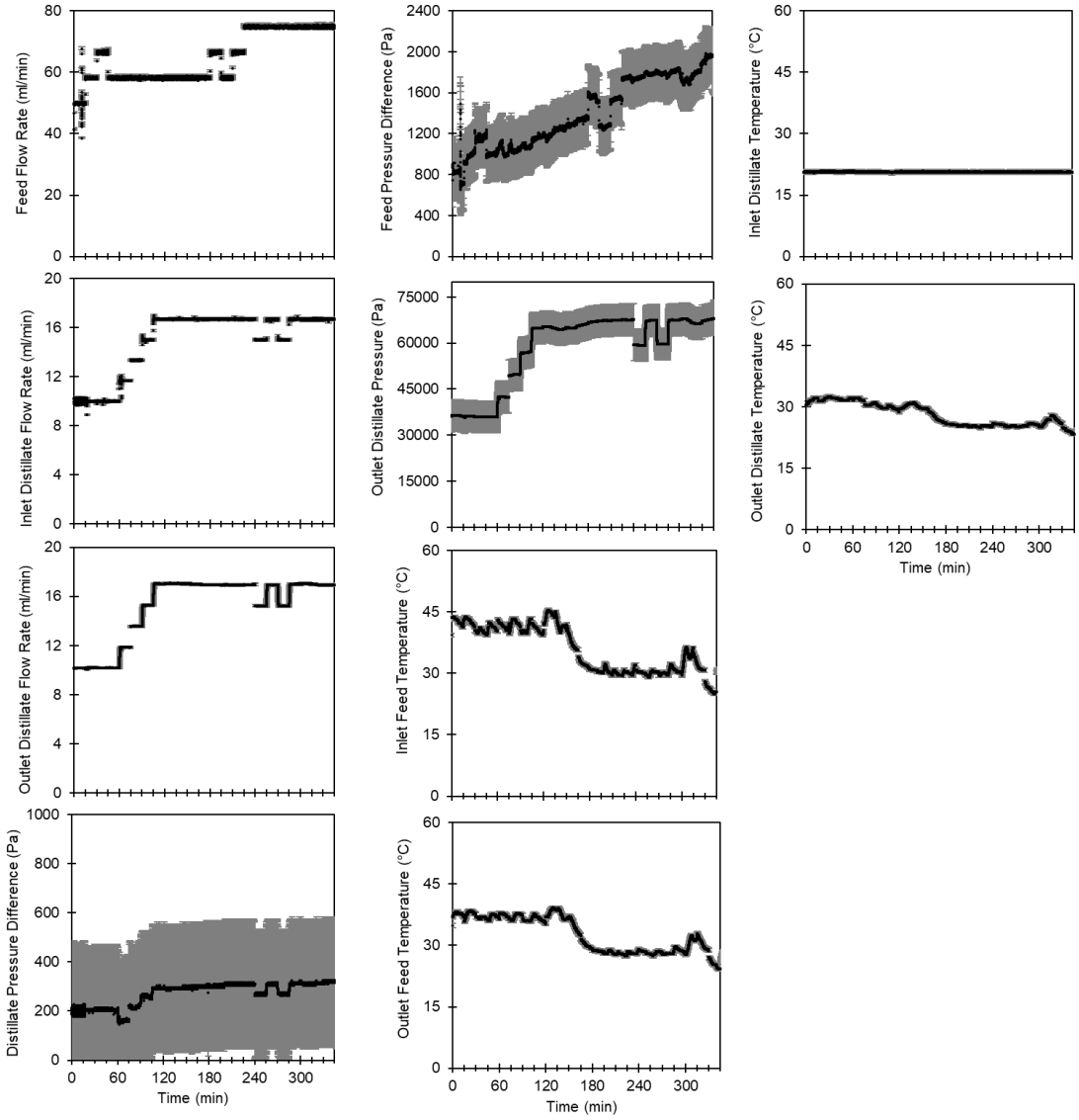

Figure S5.6 Raw sensor data used to prepare Figures 5.11 and 5.12, which show specific heat input and specific work as operating conditions are adjusted over time.

CHAPTER SIX

CONCLUSIONS

6.1 Contributions

6.1.1 Thermally Enhanced Reverse Osmosis for Reducing the Specific Energy Consumption of Seawater Desalination

Chapter Two contributes a new thermodynamic perspective to reverse osmosis desalination by establishing a framework for evaluating the integration of thermal energy into reverse osmosis systems. Unlike previous studies that largely overlook the cost of heating the feedwater, this work presents the first comprehensive energy balance for thermally enhanced reverse osmosis, capturing both mechanical and thermal energy inputs. The developed analytical model determines how feed temperature affects water flux, energy use, and permeate quality, and defines the conditions under which thermal assistance yields net energy savings. By introducing performance thresholds for thermal efficiency and heat recovery, this chapter identifies the operating conditions where heating the feedwater, using low-grade or waste heat, can improve the overall energy performance of reverse osmosis. These insights pave the way for hybrid thermal-RO configurations that more effectively leverage renewable heat sources in sustainable water treatment applications.

6.1.2 Thermally Driven Reverse Osmosis as a Novel Process Using Heat for Water Desalination

Chapter Three presents a novel thermally driven reverse osmosis system that utilizes thermal energy, available from various renewable or waste heat sources, as the primary driver for water desalination. In this study, the contribution lies in formulating a

comprehensive thermodynamic model of thermally driven reverse osmosis system, including design constraints such as piston configuration, working fluid thermophysical properties, and recovery ratios. By applying both the first and second laws of thermodynamics, the chapter calculates performance metrics, such as specific heat input, gain output ratio, and efficiencies, and demonstrates the feasibility of operating thermally driven reverse osmosis system with low-grade heat sources. This work provides a new pathway for leveraging renewable or waste thermal energy in desalination, bridging the gap between conventional reverse osmosis and thermal systems, and laying the foundation for future development of mechanically simplified, heat-driven water purification technologies.

6.1.3 Minimizing Thermal Energy Consumption in Membrane Distillation via Real-Time Control Strategies

Chapter Four introduces a novel, experimentally validated real-time control framework for improving the energy efficiency of membrane distillation systems. Unlike previous studies that rely on static optimization or simulation-based control, this work develops and implements a feedback-based perturb-and-observe algorithm to dynamically reduce specific heat input. The contribution lies in demonstrating, for the first time, a fully functional real-time control loop that adjusts feed temperature, feed circulation rate, and distillate flow rate based on live sensor feedback. The experimental setup and methodology provide a scalable template for membrane distillation system optimization in variable field conditions. This work establishes a new direction for energy efficient operation of membrane distillation systems, enabling them to self adjust

to reduce energy use, and making membrane distillation more viable for integration with low-grade heat and renewable sources.

6.1.4 Feasibility Study of an Ocean Thermal Membrane Distillation System

Chapter Four presents a comprehensive energy efficiency assessment of an ocean thermal membrane distillation, introducing a novel desalination approach that couples membrane distillation with ocean thermal gradients. The study focuses on evaluating the performance and energy requirements of ocean thermal membrane distillation in remote islands. Key contributions include the development and analysis of three ocean water intake configurations, quantification of cold water pumping work using detailed head loss models, and identification of design constraints for thermally preserving deep sea water. The chapter introduces a combined energy evaluation approach for bench-scale and ocean-scale pumping, highlighting the sensitivity of system performance to flow rate ratios and pipe dimensions. Notably, the study shows that with appropriate design, especially optimized flow conditions and intake pipe sizing, the specific energy consumption of ocean thermal membrane distillation can be lower than that of conventional reverse osmosis.

6.2 Publications

6.2.1 Journal Papers

1. S. Yagnambhatt, S. Khanmohammadi, and J. Maisonneuve, “Reducing the specific energy use of seawater desalination with thermally enhanced reverse osmosis,” Desalination, vol. 573, p. 117163, Nov. 2023, doi: 10.1016/j.desal.2023.117163.

2. S. Yagnambhatt, S. Khanmohammadi, and J. Maisonneuve, “Demonstration of a real-time maximum power point tracker for salt gradient osmotic power systems,” Applied Energy, vol. 376, p. 124205, Aug. 2024, doi: 10.1016/j.apenergy.2024.124205.
3. S. Khanmohammadi, S. Yagnambhatt, D. DelVescovo, and J. Maisonneuve, “Thermally driven reverse osmosis: thermodynamics of a novel process that uses heat for desalination and water purification,” Desalination, vol. 613, p. 119103, Oct. 2025, doi: 10.1016/j.desal.2025.119103.

6.2.2 Conference Presentations

1. S. Chintalacheruvu, S. Khanmohammadi, and J. Maisonneuve, “Effectively Using Heat to Thermally Enhance Reverse Osmosis and Reduce Specific Energy Consumption of Desalination.” Poster presentation, North American Membrane Society (NAMS), Tuscaloosa, AL, May 2023
2. S. Khanmohammadi, S. Yagnambhatt, J. Maisonneuve, “Demonstration of a Real-Time Maximum Power Point Tracker for Salt Gradient Osmotic Power Systems.” Poster presentation, North American Membrane Society (NAMS), Santa Fe, NM, May 2024.

6.2.3 Technical Reports

1. T. Ayanlade, F. Caragay, G. Griest, A. Kobus, S. Khanmohammadi, L. Markowitz, R. Younes, and J. Maisonneuve, “Ocean Thermal Membrane Distillation: Water & Energy Solutions for Remote Islands”, U.S. DOE Marine Energy Collegiate Competition, May 2025.

2. M. Brauer, G. Griest, S. Khanmohammadi, L. Markowitz, S. Yagnambhatt, M. Zheng, and J. Maisonneuve, “Using Ocean Thermal Gradients to Desalinate Water for Remote Island Communities”, U.S. DOE Marine Energy Collegiate Competition, May 2024.
3. S. Averitt, S. Chintalacheruvu, S. Khanmohammadi, N. Lemmons, D. Zehler, and J. Maisonneuve, “Harnessing the Energy of Saltwater Gradients to Improve the Efficiency of Seawater Desalination”, U.S. DOE Marine Energy Collegiate Competition, May 2023.

6.3 Future Work

6.3.1 Thermo-Kinetic Considerations and Practical Constraints in a Real TDRO Module

Based on the promising results of this study, I believe further research is needed to advance thermally driven reverse osmosis (TDRO) toward practical implementation. A deeper understanding of important factors is essential to optimize performance and design feasibility. In particular, the thermal kinetics of the process, including heat loss and heat recovery under realistic operating conditions, should be thoroughly examined. Additionally, challenges related to membrane selectivity, treatment of highly saline feeds, and achieving high recovery ratios, as commonly encountered in conventional RO systems, remain important areas for study. Long-term system performance, material durability, and effective integration with renewable heat sources also need to be evaluated to realize the full potential of TDRO as a sustainable and decentralized water desalination technology.

6.3.2 Real-Time Tracking of Maximum Exergy Efficiency in Membrane Distillation Systems

This dissertation focused on reducing the specific heat input of a membrane distillation (MD) system; however, I think future work should consider not only the quantity but also the quality of energy consumed. Specifically, the exergy content of thermal input, reflecting its thermodynamic usefulness, should be included into real-time optimization. For example, using a small amount of high exergy heat at 50 °C may, in some cases, be preferable to using a larger amount of low exergy heat at 30 °C, depending on the overall system context. Future studies could therefore integrate exergy-based control strategies alongside energy metrics to better reflect the true cost and value of thermal energy input. Additionally, broader optimization criteria, including environmental impacts such as CO_2, SO_x, and NO_x emissions, as well as economic cost could be included to support sustainable system design. This would allow for a more holistic, multi-criteria decision-making framework, particularly important when comparing systems that rely on high temperature versus low grade heat sources under real world environmental and policy constraints.

6.3.3 Advancing OTMD Through Hydraulic Design Improvements, Thermal Optimization and Renewable Integration

Future work should include full-scale hydraulic and thermal modeling of the ocean water intake and discharge system, with particular attention to factors such as biofouling, thermal losses, unsteady flow behavior, and structural durability under high-pressure deep-sea conditions. Insulation analysis of the intake pipe is especially critical, as cold water drawn from the ocean depths may experience significant temperature gain before

reaching the surface, thereby reducing system efficiency. Additionally, future studies could explore hybrid OTMD systems powered by renewable sources such as solar, wind, or ocean wave energy to enhance system independency in remote or off-grid regions. In such systems, smart control strategies would be needed to manage fluctuating energy inputs. Given the shared infrastructure and reliance on ocean thermal gradients, integrating OTMD with Ocean Thermal Energy Conversion (OTEC) systems could further improve overall system efficiency. Investigating thermal coupling mechanisms and potential heat recovery between the two processes represents a promising area for future research.

6.4 Outlook

This dissertation takes a broad look at how thermal energy can be used to improve desalination technologies. It explores several approaches, including thermally enhanced RO, thermally driven RO, controlled membrane distillation, and the use of ocean thermal energy for water treatment. Together, these studies show that low-temperature heat sources, such as waste heat, solar energy, or ocean thermal gradient, can play a key role in making desalination more energy-efficient and practical, especially in remote or off-grid areas. The work successfully meets the goals set out in the introduction and, in many ways, goes beyond them by offering new ways to design systems that use less energy and are better suited for real-world conditions. The models, experiments, and control methods developed here can be used to guide future research on hybrid systems, better automation, and stronger connections with renewable energy. Overall, this research helps move desalination toward being more sustainable, affordable, and widely available, with the potential to make a real difference in solving global water challenges.

REFERENCES

[1] "Imminent risk of a global water crisis, warns the UN World Water Development Report 2023 | UNESCO." Accessed: Jan. 29, 2025. [Online]. Available: https://www.unesco.org/en/articles/imminent-risk-global-water-crisis-warns-un-world-water-development-report-2023

[2] seametrics, "25 Facts You Should Know About the Global Water Crisis | Seametrics." Accessed: Feb. 11, 2025. [Online]. Available: https://www.seametrics.com/blog/global-water-crisis-facts/

[3] "Water action | Countries hunt for novel sources of water." Accessed: Feb. 11, 2025. [Online]. Available: https://www.unep.org/news-and-stories/story/shortages-mount-countries-hunt-novel-sources-water

[4] "U.S. Water Supply and Distribution Factsheet | Center for Sustainable Systems." Accessed: Feb. 11, 2025. [Online]. Available: https://css.umich.edu/publications/factsheets/water/us-water-supply-and-distribution-factsheet

[5] "Total Water Use in the United States | U.S. Geological Survey." Accessed: Feb. 11, 2025. [Online]. Available: https://www.usgs.gov/special-topics/water-science-school/science/total-water-use-united-states

[6] "AmericanSamoa-WUDR-Workplan.pdf." Accessed: Feb. 11, 2025. [Online]. Available: https://d9-wret.s3.us-west-2.amazonaws.com/assets/palladium/production/s3fs-public/atoms/files/AmericanSamoa-WUDR-Workplan.pdf

[7] "Water," Caribbean Green Technology Center. Accessed: Feb. 11, 2025. [Online]. Available: https://cgtc-usvi.org/water

[8] L. Cohen, "Hawaii is 'on the verge of a greater catastrophe,' locals say, as water crisis continues - CBS News." Accessed: Feb. 11, 2025. [Online]. Available: https://www.cbsnews.com/news/hawaii-water-crisis-climate-change/

[9] A. N. Angelakis *et al.*, "Desalination: From Ancient to Present and Future," *Water*, vol. 13, no. 16, Art. no. 16, Jan. 2021, doi: 10.3390/w13162222.

[10] Y. Orooji, "Father of reverse osmosis who made a huge impact on our world: Srinivasa Sourirajan (October 16, 1923–February 20, 2022)," *Npj Clean Water*, vol. 5, no. 1, p. 20, Jun. 2022, doi: 10.1038/s41545-022-00167-0.

[11] "United States Desalination Market, Size, Forecast 2023-2028." Accessed: Feb. 11, 2025. [Online]. Available: https://www.renub.com/

[12] "The Future of Desalination in Texas 2024 Biennial Report on Seawater and Brackish Groundwater Desalination in Texas".

[13] D. Curto, V. Franzitta, and A. Guercio, "A Review of the Water Desalination Technologies," *Appl. Sci.*, vol. 11, no. 2, Art. no. 2, Jan. 2021, doi: 10.3390/app11020670.

[14] M. Sarai Atab, A. J. Smallbone, and A. P. Roskilly, "An operational and economic study of a reverse osmosis desalination system for potable water and land irrigation," *Desalination*, vol. 397, pp. 174–184, Nov. 2016, doi: 10.1016/j.desal.2016.06.020.

[15] J. Kim, K. Park, D. R. Yang, and S. Hong, "A comprehensive review of energy consumption of seawater reverse osmosis desalination plants," *Appl. Energy*, vol. 254, p. 113652, Nov. 2019, doi: 10.1016/j.apenergy.2019.113652.
[16] D. O'Donnell, "Industrial Applications of Reverse Osmosis (RO) Systems," Sensorex Liquid Analysis Technology. Accessed: Feb. 12, 2025. [Online]. Available: https://sensorex.com/reverse-osmosis-ro-systems/
[17] Q. Thabit, A. Nassour, and M. Nelles, "Water Desalination Using the Once-through Multi-Stage Flash Concept: Design and Modeling," *Materials*, vol. 15, no. 17, p. 6131, Sep. 2022, doi: 10.3390/ma15176131.
[18] IChemE, "Fresh Nanotech Solutions to a Freshwater Problem." Accessed: Feb. 12, 2025. [Online]. Available: https://www.thechemicalengineer.com/features/fresh-nanotech-solutions-to-a-freshwater-problem/
[19] J. J. Feria-Díaz, M. C. López-Méndez, J. P. Rodríguez-Miranda, L. C. Sandoval-Herazo, and F. Correa-Mahecha, "Commercial Thermal Technologies for Desalination of Water from Renewable Energies: A State of the Art Review," *Processes*, vol. 9, no. 2, Art. no. 2, Feb. 2021, doi: 10.3390/pr9020262.
[20] Z. Rahimi-Ahar and M. S. Hatamipour, "Exergy analysis of thermal desalination processes: a review," *Clean Technol. Environ. Policy*, vol. 26, no. 5, pp. 1335–1362, May 2024, doi: 10.1007/s10098-023-02491-6.
[21] W. Jantaporn, A. Ali, and P. Aimar, "Specific energy requirement of direct contact membrane distillation," *Chem. Eng. Res. Des.*, vol. 128, pp. 15–26, Dec. 2017, doi: 10.1016/j.cherd.2017.09.031.
[22] M. Papapetrou, G. Kosmadakis, A. Cipollina, U. La Commare, and G. Micale, "Industrial waste heat: Estimation of the technically available resource in the EU per industrial sector, temperature level and country," *Appl. Therm. Eng.*, vol. 138, pp. 207–216, Jun. 2018, doi: 10.1016/j.applthermaleng.2018.04.043.
[23] G. Bianchi *et al.*, "Estimating the waste heat recovery in the European Union Industry," *Energy Ecol. Environ.*, vol. 4, no. 5, pp. 211–221, Oct. 2019, doi: 10.1007/s40974-019-00132-7.
[24] A. S. Rattner and S. Garimella, "Energy harvesting, reuse and upgrade to reduce primary energy usage in the USA," *Energy*, vol. 36, no. 10, pp. 6172–6183, Oct. 2011, doi: 10.1016/j.energy.2011.07.047.
[25] N. Garapati, B. M. Adams, M. R. Fleming, T. H. Kuehn, and M. O. Saar, "Combining brine or CO2 geothermal preheating with low-temperature waste heat: A higher-efficiency hybrid geothermal power system," *J. CO2 Util.*, vol. 42, p. 101323, Dec. 2020, doi: 10.1016/j.jcou.2020.101323.
[26] K. F. Beckers, A. Kolker, H. Pauling, J. D. McTigue, and D. Kesseli, "Evaluating the feasibility of geothermal deep direct-use in the United States," *Energy Convers. Manag.*, vol. 243, p. 114335, Sep. 2021, doi: 10.1016/j.enconman.2021.114335.
[27] J. Myer, "Pros and Cons of Geothermal Energy: the Earth's Sustainable Power - Kocher's Water Pumps & Tanks Inc." Accessed: Feb. 12, 2025. [Online]. Available: https://kochergeowelldrilling.com/geothermal-energy-pros-cons/
[28] "What Are the Pros and Cons of Geothermal Energy?" Accessed: Feb. 12, 2025. [Online]. Available: https://inspenet.com/en/articulo/pros-and-cons-of-geothermal-energy/

[29] “Geothermal Energy: Benefits & Challenges,” Vaia. Accessed: Feb. 12, 2025. [Online]. Available: https://www.vaia.com/en-us/explanations/environmental-science/living-environment/geothermal-energy-impact/
[30] A. Ghilardi, A. Baccioli, G. F. Frate, M. Volpe, and L. Ferrari, “Integration of ocean thermal energy conversion and pumped thermal energy storage: system design, off-design and LCOS evaluation,” *Appl. Therm. Eng.*, vol. 236, p. 121551, Jan. 2024, doi: 10.1016/j.applthermaleng.2023.121551.
[31] A. Etemadi, A. Emdadi, O. AsefAfshar, and Y. Emami, “Electricity Generation by the Ocean Thermal Energy,” *Energy Procedia*, vol. 12, pp. 936–943, Jan. 2011, doi: 10.1016/j.egypro.2011.10.123.
[32] Z. Wang *et al.*, “Pathways and challenges for efficient solar-thermal desalination,” *Sci. Adv.*, vol. 5, no. 7, p. eaax0763, Jul. 2019, doi: 10.1126/sciadv.aax0763.
[33] A. Deshmukh *et al.*, “Membrane distillation at the water-energy nexus: limits, opportunities, and challenges,” *Energy Environ. Sci.*, vol. 11, no. 5, pp. 1177–1196, May 2018, doi: 10.1039/C8EE00291F.
[34] M. Alsehli, J.-K. Choi, and M. Aljuhan, “A novel design for a solar powered multistage flash desalination,” *Sol. Energy*, vol. 153, pp. 348–359, Sep. 2017, doi: 10.1016/j.solener.2017.05.082.
[35] P. Godart, “Heat-driven direct reverse osmosis for high-performance and robust ad hoc seawater desalination,” *Desalination*, vol. 500, p. 114800, Mar. 2021, doi: 10.1016/j.desal.2020.114800.
[36] C. P. Koutsou, E. M. Kritikos, A. J. Karabelas, and M. Kostoglou, “Analysis of temperature effects on the specific energy consumption in reverse osmosis desalination processes,” *Desalination*, vol. 476, p. 114213, Feb. 2020, doi: 10.1016/j.desal.2019.114213.
[37] S. P. Agashichev and K. N. Lootahb, “Influence of temperature and permeate recovery on energy consumption of a reverse osmosis system,” *Desalination*, vol. 154, no. 3, pp. 253–266, May 2003, doi: 10.1016/S0011-9164(03)80041-3.
[38] S. Shaaban and H. Yahya, “Detailed analysis of reverse osmosis systems in hot climate conditions,” *Desalination*, vol. 423, pp. 41–51, Dec. 2017, doi: 10.1016/j.desal.2017.09.002.
[39] J. Kim, K. Park, and S. Hong, “Application of two-stage reverse osmosis system for desalination of high-salinity and high-temperature seawater with improved stability and performance,” *Desalination*, vol. 492, p. 114645, Oct. 2020, doi: 10.1016/j.desal.2020.114645.
[40] A. Jawor and E. M. V. Hoek, “Effects of feed water temperature on inorganic fouling of brackish water RO membranes,” *Desalination*, vol. 235, no. 1, pp. 44–57, Jan. 2009, doi: 10.1016/j.desal.2008.07.004.
[41] S. Chintalacheruvu, Y. Ren, and J. Maisonneuve, “Effectively using heat to thermally enhance pressure retarded osmosis,” *Desalination*, vol. 556, p. 116570, Jun. 2023, doi: 10.1016/j.desal.2023.116570.
[42] C. P. Koutsou, E. M. Kritikos, A. J. Karabelas, and M. Kostoglou, “Analysis of temperature effects on the specific energy consumption in reverse osmosis desalination processes,” *Desalination*, vol. 476, p. 114213, Feb. 2020, doi: 10.1016/j.desal.2019.114213.

[43] E. Sivertsen, T. Holt, and W. R. Thelin, “Concentration and Temperature Effects on Water and Salt Permeabilities in Osmosis and Implications in Pressure-Retarded Osmosis,” *Membranes*, vol. 8, no. 3, Art. no. 3, Sep. 2018, doi: 10.3390/membranes8030039.
[44] J. Kim, K. Park, and S. Hong, “Application of two-stage reverse osmosis system for desalination of high-salinity and high-temperature seawater with improved stability and performance,” *Desalination*, vol. 492, p. 114645, Oct. 2020, doi: 10.1016/j.desal.2020.114645.
[45] C. Chen, X. Huang, P. Prakash, S. Chilekar, and R. Franks, “Produced water desalination using high temperature membranes,” *Desalination*, vol. 513, p. 115144, Oct. 2021, doi: 10.1016/j.desal.2021.115144.
[46] S. Shaaban and H. Yahya, “Detailed analysis of reverse osmosis systems in hot climate conditions,” *Desalination*, vol. 423, pp. 41–51, Dec. 2017, doi: 10.1016/j.desal.2017.09.002.
[47] B. Moossa, P. Trivedi, H. Saleem, and S. J. Zaidi, “Desalination in the GCC countries- a review,” *J. Clean. Prod.*, vol. 357, p. 131717, Jul. 2022, doi: 10.1016/j.jclepro.2022.131717.
[48] S. Sundaramoorthy, G. Srinivasan, and D. V. R. Murthy, “An analytical model for spiral wound reverse osmosis membrane modules: Part I — Model development and parameter estimation,” *Desalination*, vol. 280, no. 1, pp. 403–411, Oct. 2011, doi: 10.1016/j.desal.2011.03.047.
[49] C. P. Koutsou, A. J. Karabelas, and M. Kostoglou, “Membrane desalination under constant water recovery – The effect of module design parameters on system performance,” *Sep. Purif. Technol.*, vol. 147, pp. 90–113, Jun. 2015, doi: 10.1016/j.seppur.2015.04.012.
[50] H. Sitaraman and I. Battiato, “Impact of large-scale effects on mass transfer and concentration polarization in Reverse Osmosis membrane systems,” *Sep. Purif. Technol.*, vol. 303, p. 122121, Dec. 2022, doi: 10.1016/j.seppur.2022.122121.
[51] F. Eleiwi, N. Ghaffour, A. S. Alsaadi, L. Francis, and T. M. Laleg-Kirati, “Dynamic modeling and experimental validation for direct contact membrane distillation (DCMD) process,” *Desalination*, vol. 384, pp. 1–11, Apr. 2016, doi: 10.1016/j.desal.2016.01.004.
[52] G. E. Dévora-Isiordia *et al.*, “Evaluation of Concentration Polarization Due to the Effect of Feed Water Temperature Change on Reverse Osmosis Membranes,” *Membranes*, vol. 13, no. 1, Art. no. 1, Jan. 2023, doi: 10.3390/membranes13010003.
[53] S. Kim and E. M. V. Hoek, “Modeling concentration polarization in reverse osmosis processes,” *Desalination*, vol. 186, no. 1, pp. 111–128, Dec. 2005, doi: 10.1016/j.desal.2005.05.017.
[54] A. Jawor and E. M. V. Hoek, “Effects of feed water temperature on inorganic fouling of brackish water RO membranes,” *Desalination*, vol. 235, no. 1, pp. 44–57, Jan. 2009, doi: 10.1016/j.desal.2008.07.004.
[55] B. A. Abdelkader and M. H. Sharqawy, “Temperature effects on salinity gradient energy harvesting and utilized membrane properties – Experimental and numerical investigation,” *Sustain. Energy Technol. Assess.*, vol. 48, p. 101666, Dec. 2021, doi: 10.1016/j.seta.2021.101666.

[56] M. R. Chowdhury and J. R. McCutcheon, “Elucidating the impact of temperature gradients across membranes during forward osmosis: Coupling heat and mass transfer models for better prediction of real osmotic systems,” *J. Membr. Sci.*, vol. 553, pp. 189–199, May 2018, doi: 10.1016/j.memsci.2018.01.004.
[57] E. Sivertsen, T. Holt, and W. R. Thelin, “Concentration and Temperature Effects on Water and Salt Permeabilities in Osmosis and Implications in Pressure-Retarded Osmosis,” *Membranes*, vol. 8, no. 3, Art. no. 3, Sep. 2018, doi: 10.3390/membranes8030039.
[58] C. P. Koutsou, E. M. Kritikos, A. J. Karabelas, and M. Kostoglou, “Analysis of temperature effects on the specific energy consumption in reverse osmosis desalination processes,” *Desalination*, vol. 476, p. 114213, Feb. 2020, doi: 10.1016/j.desal.2019.114213.
[59] J. Maisonneuve, P. Pillay, and C. B. Laflamme, “Pressure-retarded osmotic power system model considering non-ideal effects,” *Renew. Energy*, vol. 75, pp. 416–424, Mar. 2015, doi: 10.1016/j.renene.2014.10.011.
[60] K. Touati and F. Tadeo, “Study of the Reverse Salt Diffusion in pressure retarded osmosis: Influence on concentration polarization and effect of the operating conditions,” *Desalination*, vol. 389, pp. 171–186, Jul. 2016, doi: 10.1016/j.desal.2016.02.014.
[61] J. Kim and S. Hong, “Optimizing seawater reverse osmosis with internally staged design to improve product water quality and energy efficiency,” *J. Membr. Sci.*, vol. 568, pp. 76–86, Dec. 2018, doi: 10.1016/j.memsci.2018.09.046.
[62] G. Guillen and E. M. V. Hoek, “Modeling the impacts of feed spacer geometry on reverse osmosis and nanofiltration processes,” *Chem. Eng. J.*, vol. 149, no. 1, pp. 221–231, Jul. 2009, doi: 10.1016/j.cej.2008.10.030.
[63] J. Wang *et al.*, “A critical review of transport through osmotic membranes,” *J. Membr. Sci.*, vol. 454, pp. 516–537, Mar. 2014, doi: 10.1016/j.memsci.2013.12.034.
[64] “Effect of Internal and External Concentration Polarizations on the Performance of Forward Osmosis Process | IntechOpen.” Accessed: Mar. 10, 2025. [Online]. Available: https://www.intechopen.com/chapters/57339
[65] S. Adhikary, Md. S. Islam, K. Touati, S. Sultana, A. S. Ramamurthy, and Md. S. Rahaman, “Increased power density with low salt flux using organic draw solutions for pressure-retarded osmosis at elevated temperatures,” *Desalination*, vol. 484, p. 114420, Jun. 2020, doi: 10.1016/j.desal.2020.114420.
[66] S. J. Einarsson and B. Wu, “Thermal associated pressure-retarded osmosis processes for energy production: A review,” *Sci. Total Environ.*, vol. 757, p. 143731, Feb. 2021, doi: 10.1016/j.scitotenv.2020.143731.
[67] C. Chen, X. Huang, P. Prakash, S. Chilekar, and R. Franks, “Produced water desalination using high temperature membranes,” *Desalination*, vol. 513, p. 115144, Oct. 2021, doi: 10.1016/j.desal.2021.115144.
[68] C. P. Koutsou, E. M. Kritikos, A. J. Karabelas, and M. Kostoglou, “Analysis of temperature effects on the specific energy consumption in reverse osmosis desalination processes,” *Desalination*, vol. 476, p. 114213, Feb. 2020, doi: 10.1016/j.desal.2019.114213.

[69] "A computational fluid dynamics model to predict performance of hollow fiber membrane modules in forward osmosis," CoLab. Accessed: Mar. 10, 2025. [Online]. Available: https://colab.ws/articles/10.1016%2Fj.memsci.2020.117973
[70] "Densities and Viscosities of Ternary Systems of Water + Fructose + Sodium Chloride from 20 to 40 °C | Journal of Chemical & Engineering Data." Accessed: Mar. 10, 2025. [Online]. Available: https://pubs.acs.org/doi/10.1021/je000265t
[71] J. Maisonneuve, P. Pillay, and C. B. Laflamme, "Pressure-retarded osmotic power system model considering non-ideal effects," *Renew. Energy*, vol. 75, pp. 416–424, Mar. 2015, doi: 10.1016/j.renene.2014.10.011.
[72] O. US EPA, "Secondary Drinking Water Standards: Guidance for Nuisance Chemicals." Accessed: Mar. 10, 2025. [Online]. Available: https://www.epa.gov/sdwa/secondary-drinking-water-standards-guidance-nuisance-chemicals
[73] H. Canada, "Guidelines for Canadian Drinking Water Quality: Guideline Technical Document – Total Dissolved Solids (TDS)." Accessed: Mar. 10, 2025. [Online]. Available: https://www.canada.ca/en/health-canada/services/publications/healthy-living/guidelines-canadian-drinking-water-quality-guideline-technical-document-total-dissolved-solids-tds.html
[74] S. H. Aladwani, M. A. Al-Obaidi, and I. M. Mujtaba, "Performance of reverse osmosis based desalination process using spiral wound membrane: Sensitivity study of operating parameters under variable seawater conditions," *Clean. Eng. Technol.*, vol. 5, p. 100284, Dec. 2021, doi: 10.1016/j.clet.2021.100284.
[75] O. M. A. Al-hotmani, M. A. Al-Obaidi, Y. M. John, R. Patel, and I. M. Mujtaba, "Optimisation of hybrid MED-TVC and double reverse osmosis processes for producing different grades of water in a smart city," *Desalination*, vol. 534, p. 115776, Jul. 2022, doi: 10.1016/j.desal.2022.115776.
[76] A. Jawor and E. M. V. Hoek, "Effects of feed water temperature on inorganic fouling of brackish water RO membranes," *Desalination*, vol. 235, no. 1, pp. 44–57, Jan. 2009, doi: 10.1016/j.desal.2008.07.004.
[77] M. Xie, J. Lee, L. D. Nghiem, and M. Elimelech, "Role of pressure in organic fouling in forward osmosis and reverse osmosis," *J. Membr. Sci.*, vol. 493, pp. 748–754, Nov. 2015, doi: 10.1016/j.memsci.2015.07.033.
[78] "Energy Conservation Program for Consumer Products: Representative Average Unit Costs of Energy".
[79] A. A. Atia, N. Y. Yip, and V. Fthenakis, "Pathways for mal and zero liquid discharge with enhanced reverse osmosis technologies: Module-scale modeling and techno-economic assessment," *Desalination*, vol. 509, p. 115069, Aug. 2021, doi: 10.1016/j.desal.2021.115069.
[80] A. Alkhudhiri, N. Darwish, and N. Hilal, "Membrane distillation: A comprehensive review," *Desalination*, vol. 287, pp. 2–18, Feb. 2012, doi: 10.1016/j.desal.2011.08.027.
[81] S. H. Aladwani, M. A. Al-Obaidi, and I. M. Mujtaba, "Performance of reverse osmosis based desalination process using spiral wound membrane: Sensitivity study of operating parameters under variable seawater conditions," *Clean. Eng. Technol.*, vol. 5, p. 100284, Dec. 2021, doi: 10.1016/j.clet.2021.100284.

[82] S. Shaaban and H. Yahya, “Detailed analysis of reverse osmosis systems in hot climate conditions,” *Desalination*, vol. 423, pp. 41–51, Dec. 2017, doi: 10.1016/j.desal.2017.09.002.
[83] C. Chen, X. Huang, P. Prakash, S. Chilekar, and R. Franks, “Produced water desalination using high temperature membranes,” *Desalination*, vol. 513, p. 115144, Oct. 2021, doi: 10.1016/j.desal.2021.115144.
[84] D. Escarabajal-Henarejos, D. Parras-Burgos, L. Ávila-Dávila, F. J. Cánovas-Rodríguez, and J. M. Molina-Martínez, “Study of the Influence of Temperature on Boron Concentration Estimation in Desalinated Seawater for Agricultural Irrigation,” *Water*, vol. 13, no. 3, Art. no. 3, Jan. 2021, doi: 10.3390/w13030322.
[85] A. H. Haidari, R. Gonzalez-Olmos, and S. G. J. Heijman, “Scaling after remineralisation of reverse osmosis permeate,” *Desalination*, vol. 467, pp. 57–63, Oct. 2019, doi: 10.1016/j.desal.2019.06.002.
[86] “Membrane Technology and Applications | Wiley Online Books.” Accessed: Mar. 12, 2025. [Online]. Available: https://onlinelibrary-wiley-com.huaryu.kl.oakland.edu/doi/book/10.1002/9781118359686
[87] J. G. Wijmans and R. W. Baker, “The solution-diffusion model: a review,” *J. Membr. Sci.*, vol. 107, no. 1, pp. 1–21, Nov. 1995, doi: 10.1016/0376-7388(95)00102-I.
[88] D. Paul, “Reformulation of the solution-diffusion theory of reverse osmosis,” *J. Membr. Sci.*, vol. 241, no. 2, pp. 371–386, Oct. 2004, doi: 10.1016/j.memsci.2004.05.026.
[89] L. Feng, L. Xie, G. Suo, X. Shao, and T. Dong, “Influence of Temperature on the Performance of Forward Osmosis Using Ammonium Bicarbonate as Draw Solute,” *Trans. Tianjin Univ.*, vol. 24, no. 6, pp. 571–579, Nov. 2018, doi: 10.1007/s12209-018-0159-1.
[90] K. Touati, C. Hänel, F. Tadeo, and T. Schiestel, “Effect of the feed and draw solution temperatures on PRO performance: Theoretical and experimental study,” *Desalination*, vol. 365, pp. 182–195, Jun. 2015, doi: 10.1016/j.desal.2015.02.016.
[91] N.-N. Bui, J. T. Arena, and J. R. McCutcheon, “Proper accounting of mass transfer resistances in forward osmosis: Improving the accuracy of model predictions of structural parameter,” *J. Membr. Sci.*, vol. 492, pp. 289–302, Oct. 2015, doi: 10.1016/j.memsci.2015.02.001.
[92] Q. Wang, Z. Zhou, J. Li, Q. Tang, and Y. Hu, “Modeling and measurement of temperature and draw solution concentration induced water flux increment efficiencies in the forward osmosis membrane process,” *Desalination*, vol. 452, pp. 75–86, Feb. 2019, doi: 10.1016/j.desal.2018.11.001.
[93] W.-J. Kim, O. Campanella, and D. R. Heldman, “A stepwise approach to predict the performance of forward osmosis operation: Effect of temperature and flow direction,” *Desalination*, vol. 538, p. 115889, Sep. 2022, doi: 10.1016/j.desal.2022.115889.
[94] Q. She, X. Jin, and C. Y. Tang, “Osmotic power production from salinity gradient resource by pressure retarded osmosis: Effects of operating conditions and reverse solute diffusion,” *J. Membr. Sci.*, vol. 401–402, pp. 262–273, May 2012, doi: 10.1016/j.memsci.2012.02.014.

[95] K. Touati, F. Tadeo, C. Hänel, and T. Schiestel, “Effect of the operating temperature on hydrodynamics and membrane parameters in pressure retarded osmosis,” *Desalination Water Treat.*, vol. 57, no. 23, pp. 10477–10489, May 2016, doi: 10.1080/19443994.2015.1039600.
[96] H. Gong, D. D. Anastasio, K. Wang, and J. R. McCutcheon, “Finding better draw solutes for osmotic heat engines: Understanding transport of ions during pressure retarded osmosis,” *Desalination*, vol. 421, pp. 32–39, Nov. 2017, doi: 10.1016/j.desal.2017.03.030.
[97] D. D. Anastasio, J. T. Arena, E. A. Cole, and J. R. McCutcheon, “Impact of temperature on power density in closed-loop pressure retarded osmosis for grid storage,” *J. Membr. Sci.*, vol. 479, pp. 240–245, Apr. 2015, doi: 10.1016/j.memsci.2014.12.046.
[98] M. R. Chowdhury and J. R. McCutcheon, “Elucidating the impact of temperature gradients across membranes during forward osmosis: Coupling heat and mass transfer models for better prediction of real osmotic systems,” *J. Membr. Sci.*, vol. 553, pp. 189–199, May 2018, doi: 10.1016/j.memsci.2018.01.004.
[99] M. Xie, W. E. Price, L. D. Nghiem, and M. Elimelech, “Effects of feed and draw solution temperature and transmembrane temperature difference on the rejection of trace organic contaminants by forward osmosis,” *J. Membr. Sci.*, vol. 438, pp. 57–64, Jul. 2013, doi: 10.1016/j.memsci.2013.03.031.
[100] A. Abdelrasoul, H. Doan, A. Lohi, and C.-H. Cheng, “Mass Transfer Mechanisms and Transport Resistances in Membrane Separation Process,” in *Mass Transfer - Advancement in Process Modelling*, M. Solecki, Ed., InTech, 2015. doi: 10.5772/60866.
[101] S. Zhao and L. Zou, “Effects of working temperature on separation performance, membrane scaling and cleaning in forward osmosis desalination,” *Desalination*, vol. 278, no. 1–3, pp. 157–164, Sep. 2011, doi: 10.1016/j.desal.2011.05.018.
[102] K. Touati, F. Tadeo, C. Hänel, and T. Schiestel, “Effect of the operating temperature on hydrodynamics and membrane parameters in pressure retarded osmosis,” *Desalination Water Treat.*, vol. 57, no. 23, pp. 10477–10489, May 2016, doi: 10.1080/19443994.2015.1039600.
[103] M. M. Mekonnen and A. Y. Hoekstra, “Four billion people facing severe water scarcity,” *Sci. Adv.*, vol. 2, no. 2, p. e1500323, Feb. 2016, doi: 10.1126/sciadv.1500323.
[104] M. Naddaf, “The world faces a water crisis - 4 powerful charts show how,” *Nature*, vol. 615, no. 7954, pp. 774–775, Mar. 2023, doi: 10.1038/d41586-023-00842-3.
[105] C. He *et al.*, “Future global urban water scarcity and potential solutions,” *Nat. Commun.*, vol. 12, no. 1, p. 4667, Aug. 2021, doi: 10.1038/s41467-021-25026-3.
[106] “The Future of Municipal Wastewater Reuse Concentrate Management: Drivers, Challenges, and Opportunities | Environmental Science & Technology.” Accessed: Sep. 25, 2024. [Online]. Available: https://pubs.acs.org/doi/10.1021/acs.est.3c06774
[107] E. Jones, M. Qadir, M. T. H. van Vliet, V. Smakhtin, and S. Kang, “The state of desalination and brine production: A global outlook,” *Sci. Total Environ.*, vol. 657, pp. 1343–1356, Mar. 2019, doi: 10.1016/j.scitotenv.2018.12.076.

[108] “Pathways and challenges for efficient solar-thermal desalination | Science Advances.” Accessed: Sep. 25, 2024. [Online]. Available: https://www.science.org/doi/10.1126/sciadv.aax0763
[109] S. Chintalacheruvu, Y. Ren, and J. Maisonneuve, “Effectively using heat to thermally enhance pressure retarded osmosis,” *Desalination*, vol. 556, p. 116570, Jun. 2023, doi: 10.1016/j.desal.2023.116570.
[110] S. Yagnambhatt, S. Khanmohammadi, and J. Maisonneuve, “Reducing the specific energy use of seawater desalination with thermally enhanced reverse osmosis,” *Desalination*, vol. 573, p. 117163, Mar. 2024, doi: 10.1016/j.desal.2023.117163.
[111] A. Deshmukh *et al.*, “Membrane distillation at the water-energy nexus: limits, opportunities, and challenges,” *Energy Environ. Sci.*, vol. 11, no. 5, pp. 1177–1196, May 2018, doi: 10.1039/C8EE00291F.
[112] O. Younis *et al.*, “Comprehensive Review on Solar Stills—Latest Developments and Overview,” *Sustainability*, vol. 14, no. 16, Art. no. 16, Jan. 2022, doi: 10.3390/su141610136.
[113] S. Rajesh and C. Chiranjeevi, “Hybrid thermal desalination systems for sustainable development – A critical review,” *Sol. Energy*, vol. 270, p. 112364, Mar. 2024, doi: 10.1016/j.solener.2024.112364.
[114] M. H. Sharqawy, J. H. Lienhard, and S. M. Zubair, “Thermophysical properties of seawater: a review of existing correlations and data,” *Desalination Water Treat.*, vol. 16, no. 1–3, pp. 354–380, Apr. 2010, doi: 10.5004/dwt.2010.1079.
[115] A. J. Schunke, G. A. Hernandez Herrera, L. Padhye, and T.-A. Berry, “Energy Recovery in SWRO Desalination: Current Status and New Possibilities,” *Front. Sustain. Cities*, vol. 2, Apr. 2020, doi: 10.3389/frsc.2020.00009.
[116] L. Wang, C. Violet, R. M. DuChanois, and M. Elimelech, “Derivation of the Theoretical Minimum Energy of Separation of Desalination Processes,” *J. Chem. Educ.*, vol. 97, no. 12, pp. 4361–4369, Dec. 2020, doi: 10.1021/acs.jchemed.0c01194.
[117] A. S. Stillwell and M. E. Webber, “Predicting the Specific Energy Consumption of Reverse Osmosis Desalination,” *Water*, vol. 8, no. 12, Art. no. 12, Dec. 2016, doi: 10.3390/w8120601.
[118] M. Raninga, A. Mudgal, V. Patel, and J. Patel, “Desalination of brackish water using cascade Rankine cycle based reverse osmosis system,” *IOP Conf. Ser. Mater. Sci. Eng.*, vol. 1146, no. 1, p. 012007, May 2021, doi: 10.1088/1757-899X/1146/1/012007.
[119] D. Manolakos, G. Kosmadakis, S. Kyritsis, and G. Papadakis, “Identification of behaviour and evaluation of performance of small scale, low-temperature Organic Rankine Cycle system coupled with a RO desalination unit,” *Energy*, vol. 34, no. 6, pp. 767–774, Jun. 2009, doi: 10.1016/j.energy.2009.02.008.
[120] O. N. Igobo and P. A. Davies, “Isothermal Organic Rankine Cycle (ORC) driving Reverse Osmosis (RO) desalination: Experimental investigation and case study using R245fa working fluid,” *Appl. Therm. Eng.*, vol. 136, pp. 740–746, May 2018, doi: 10.1016/j.applthermaleng.2018.02.056.
[121] A. Naminezhad and M. Mehregan, “Energy and exergy analyses of a hybrid system integrating solar-driven organic Rankine cycle, multi-effect distillation, and reverse

osmosis desalination systems," *Renew. Energy*, vol. 185, pp. 888–903, Feb. 2022, doi: 10.1016/j.renene.2021.12.076.
[122] G. Xia, Q. Sun, J. Wang, X. Cao, Y. Yu, and L. Wang, "Theoretical analysis of a reverse osmosis desalination system driven by solar-powered organic Rankine cycle and wind energy," *Desalination Water Treat.*, vol. 53, no. 4, pp. 876–886, Jan. 2015, doi: 10.1080/19443994.2014.927185.
[123] B. Peñate and L. García-Rodríguez, "Seawater reverse osmosis desalination driven by a solar Organic Rankine Cycle: Design and technology assessment for medium capacity range," *Desalination*, vol. 284, pp. 86–91, Jan. 2012, doi: 10.1016/j.desal.2011.08.040.
[124] D. Manolakos, G. Kosmadakis, S. Kyritsis, and G. Papadakis, "On site experimental evaluation of a low-temperature solar organic Rankine cycle system for RO desalination," *Sol. Energy*, vol. 83, no. 5, pp. 646–656, May 2009, doi: 10.1016/j.solener.2008.10.014.
[125] A. M. Delgado-Torres and L. García-Rodríguez, "Design recommendations for solar organic Rankine cycle (ORC)–powered reverse osmosis (RO) desalination," *Renew. Sustain. Energy Rev.*, vol. 16, no. 1, pp. 44–53, Jan. 2012, doi: 10.1016/j.rser.2011.07.135.
[126] T. Hai *et al.*, "Performance analysis and optimization of a novel geothermal trigeneration system with enhanced Organic Rankine cycle, Kalina cycle, reverse osmosis, and supercritical CO2 cycle," *Renew. Energy*, vol. 211, pp. 539–562, Jul. 2023, doi: 10.1016/j.renene.2023.04.080.
[127] A. Farsi and M. A. Rosen, "Multi-Objective Optimization of a Geothermal Steam Turbine Combined With Reverse Osmosis and Multi-Effect Desalination for Sustainable Freshwater Production," *J. Energy Resour. Technol.*, vol. 144, no. 052102, Jan. 2022, doi: 10.1115/1.4053298.
[128] M. Raninga, A. Mudgal, V. K. Patel, and J. Patel, "Design of ORC-RO system for utilizing waste heat from flue gases of coal-fired thermal power plant," *Mater. Today Proc.*, vol. 77, pp. 105–110, Jan. 2023, doi: 10.1016/j.matpr.2022.10.143.
[129] A. F. Kareem, A. Akroot, H. A. Abdul Wahhab, W. Talal, R. M. Ghazal, and A. Alfaris, "Exergo–Economic and Parametric Analysis of Waste Heat Recovery from Taji Gas Turbines Power Plant Using Rankine Cycle and Organic Rankine Cycle," *Sustainability*, vol. 15, no. 12, Art. no. 12, Jan. 2023, doi: 10.3390/su15129376.
[130] P. Godart, "Design and simulation of a heat-driven direct reverse osmosis device for seawater desalination powered by solar thermal energy," *Appl. Energy*, vol. 284, p. 116039, Feb. 2021, doi: 10.1016/j.apenergy.2020.116039.
[131] P. Godart, "Heat-driven direct reverse osmosis for high-performance and robust ad hoc seawater desalination," *Desalination*, vol. 500, p. 114800, Mar. 2021, doi: 10.1016/j.desal.2020.114800.
[132] K. S. Spiegler and Y. M. El-Sayed, "The energetics of desalination processes," *Desalination*, vol. 134, no. 1, pp. 109–128, Apr. 2001, doi: 10.1016/S0011-9164(01)00121-7.
[133] L. Wang, C. Violet, R. M. DuChanois, and M. Elimelech, "Derivation of the Theoretical Minimum Energy of Separation of Desalination Processes," *J. Chem.*

Educ., vol. 97, no. 12, pp. 4361–4369, Dec. 2020, doi: 10.1021/acs.jchemed.0c01194.
[134] J. E. Thompson and A. S. Paluch, "Revisiting the Clausius/Clapeyron Equation and the Cause of Linearity," *Thermo*, vol. 3, no. 3, Art. no. 3, Sep. 2023, doi: 10.3390/thermo3030025.
[135] "Generalized Least Energy of Separation for Desalination and Other Chemical Separation Processes." Accessed: Apr. 08, 2025. [Online]. Available: https://www.mdpi.com/1099-4300/15/6/2046
[136] T. Altmann, J. Robert, A. Bouma, J. Swaminathan, and J. H. Lienhard, "Primary energy and exergy of desalination technologies in a power-water cogeneration scheme," *Appl. Energy*, vol. 252, p. 113319, Oct. 2019, doi: 10.1016/j.apenergy.2019.113319.
[137] N. Li *et al.*, "Development of a modified gas turbine-based sustainable power generation and water treatment system; Economical/environmental considerations and data-driven optimization," *J. Clean. Prod.*, vol. 450, p. 141904, Apr. 2024, doi: 10.1016/j.jclepro.2024.141904.
[138] H. R. Abbasi and H. Pourrahmani, "Multi-objective optimization and exergoeconomic analysis of a continuous solar-driven system with PCM for power, cooling and freshwater production," *Energy Convers. Manag.*, vol. 211, p. 112761, May 2020, doi: 10.1016/j.enconman.2020.112761.
[139] H. Shakibi *et al.*, "Design and multi-objective optimization of a multi-generation system based on PEM electrolyzer, RO unit, absorption cooling system, and ORC utilizing machine learning approaches; a case study of Australia," *Energy*, vol. 278, p. 127796, Sep. 2023, doi: 10.1016/j.energy.2023.127796.
[140] H. Kianfard, S. Khalilarya, and S. Jafarmadar, "Exergy and exergoeconomic evaluation of hydrogen and distilled water production via combination of PEM electrolyzer, RO desalination unit and geothermal driven dual fluid ORC," *Energy Convers. Manag.*, vol. 177, pp. 339–349, Dec. 2018, doi: 10.1016/j.enconman.2018.09.057.
[141] O. A. Hamed, "Thermal Desalination: Performance and Challenges," in *Corrosion and Fouling Control in Desalination Industry*, V. S. Saji, A. A. Meroufel, and A. A. Sorour, Eds., Cham: Springer International Publishing, 2020, pp. 29–47. doi: 10.1007/978-3-030-34284-5_2.
[142] M. Z. AL-Nabulsi, M. A. Antar, M. A. Abido, and D. U. Lawal, "Multi-Objective Optimization of Parallel Cross Multi-Effect Desalination Systems with Thermal Vapor Compression," *Arab. J. Sci. Eng.*, vol. 47, no. 12, pp. 16505–16522, Dec. 2022, doi: 10.1007/s13369-022-07063-2.
[143] J. J. Feria-Díaz, M. C. López-Méndez, J. P. Rodríguez-Miranda, L. C. Sandoval-Herazo, and F. Correa-Mahecha, "Commercial Thermal Technologies for Desalination of Water from Renewable Energies: A State of the Art Review," *Processes*, vol. 9, no. 2, Art. no. 2, Feb. 2021, doi: 10.3390/pr9020262.
[144] I. Ullah and M. G. Rasul, "Recent Developments in Solar Thermal Desalination Technologies: A Review," *Energies*, vol. 12, no. 1, Art. no. 1, Jan. 2019, doi: 10.3390/en12010119.

[145] I. B. Askari and M. Ameri, “Thermodynamic analysis of multi effect desalination unit with thermal vapor compression feed by different motive steam pressures,” *Desalination Water Treat.*, vol. 184, pp. 57–71, Apr. 2020, doi: 10.5004/dwt.2020.25387.
[146] M. C. MacDonald *et al.*, “Mitigating drought impacts in remote island atolls with traditional water usage behaviors and modern technology,” *Sci. Total Environ.*, vol. 741, p. 140230, Nov. 2020, doi: 10.1016/j.scitotenv.2020.140230.
[147] C. Matos, P. Cabrera, J. A. Carta, and N. Melián-Martel, “Wind-Powered Desalination on Islands: A Review of Energy–Water Pathways,” *J. Mar. Sci. Eng.*, vol. 12, no. 3, Art. no. 3, Mar. 2024, doi: 10.3390/jmse12030464.
[148] M. Palmeros Parada *et al.*, “Resource recovery from desalination, the case of small islands,” *Resour. Conserv. Recycl.*, vol. 199, p. 107287, Dec. 2023, doi: 10.1016/j.resconrec.2023.107287.
[149] B. Chelliah, S. Manoj, and N. Srikanth, “Renewable Powered Desalination System for Remote Islands in Singapore,” in *2018 Asian Conference on Energy, Power and Transportation Electrification (ACEPT)*, Oct. 2018, pp. 1–7. doi: 10.1109/ACEPT.2018.8610863.
[150] G. Kyriakarakos, G. Papadakis, and C. A. Karavitis, “Renewable Energy Desalination for Island Communities: Status and Future Prospects in Greece,” *Sustainability*, vol. 14, no. 13, Art. no. 13, Jan. 2022, doi: 10.3390/su14138176.
[151] J. Bundschuh, M. Kaczmarczyk, N. Ghaffour, and B. Tomaszewska, “State-of-the-art of renewable energy sources used in water desalination: Present and future prospects,” *Desalination*, vol. 508, p. 115035, Jul. 2021, doi: 10.1016/j.desal.2021.115035.
[152] B. Zolghadr-Asli *et al.*, “A review of limitations and potentials of desalination as a sustainable source of water,” *Environ. Sci. Pollut. Res. Int.*, vol. 30, no. 56, pp. 118161–118174, 2023, doi: 10.1007/s11356-023-30662-x.
[153] F. Succetti, A. Rosato, R. Araneo, G. Di Lorenzo, and M. Panella, “Challenges and Perspectives of Smart Grid Systems in Islands: A Real Case Study,” *Energies*, vol. 16, no. 2, Art. no. 2, Jan. 2023, doi: 10.3390/en16020583.
[154] D. Ochoa-Correa, P. Arévalo, and S. Martinez, “Pathways to 100% Renewable Energy in Island Systems: A Systematic Review of Challenges, Solutions Strategies, and Success Cases,” *Technologies*, vol. 13, no. 5, Art. no. 5, May 2025, doi: 10.3390/technologies13050180.
[155] M. Soto Calvo and H. S. Lee, “Ocean thermal energy conversion (OTEC) potential in central American and Caribbean regions: A multicriteria analysis for optimal sites,” *Appl. Energy*, vol. 394, p. 126182, Sep. 2025, doi: 10.1016/j.apenergy.2025.126182.
[156] D. Vera, A. Baccioli, F. Jurado, and U. Desideri, “Modeling and optimization of an ocean thermal energy conversion system for remote islands electrification,” *Renew. Energy*, vol. 162, pp. 1399–1414, Dec. 2020, doi: 10.1016/j.renene.2020.07.074.
[157] CSIRO, “Commonwealth Scientific and Industrial Research Organisation, Australian Government.” Accessed: Jul. 21, 2025. [Online]. Available: https://www.csiro.au/en/

[158] “Twenty Thousand Leagues Under the Seas by Jules Verne: Part 1 Chapter 12 (continued) - The Literature Page.” Accessed: Jun. 23, 2025. [Online]. Available: https://www.literaturepage.com/read/twentythousandleagues-91.html
[159] H.-J. Kim, H.-S. Lee, S.-T. Lim, and M. Petterson, “The Suitability of the Pacific Islands for Harnessing Ocean Thermal Energy and the Feasibility of OTEC Plants for Onshore or Offshore Processing,” *Geosciences*, vol. 11, no. 10, Art. no. 10, Oct. 2021, doi: 10.3390/geosciences11100407.
[160] “OTEC-2018-Report.pdf.” Accessed: Jun. 23, 2025. [Online]. Available: https://www.hnei.hawaii.edu/wp-content/uploads/OTEC-2018-Report.pdf?utm_source=chatgpt.com
[161] “Okinawa OTEC Demonstration Facility.” Accessed: Jun. 23, 2025. [Online]. Available: http://otecokinawa.com/en/
[162] A. Habibic, “Global OTEC partners with French firm to develop its floating OTEC platform,” Offshore Energy. Accessed: Jun. 23, 2025. [Online]. Available: https://www.offshore-energy.biz/global-otec-partners-with-french-firm-to-develop-its-floating-otec-platform/
[163] A. S. Kim, H.-J. Kim, H.-S. Lee, and S. Cha, “Dual-use open cycle ocean thermal energy conversion (OC-OTEC) using multiple condensers for adjustable power generation and seawater desalination,” *Renew. Energy*, vol. 85, pp. 344–358, Jan. 2016, doi: 10.1016/j.renene.2015.06.014.
[164] C. Fan, C. Zhang, and Y. Chen, “Dynamic operation characteristics of ocean thermal energy conversion using Kalina cycle,” *Renew. Energy*, vol. 231, p. 120909, Sep. 2024, doi: 10.1016/j.renene.2024.120909.
[165] A. Giostri, A. Romei, and M. Binotti, “Off-design performance of closed OTEC cycles for power generation,” *Renew. Energy*, vol. 170, pp. 1353–1366, Jun. 2021, doi: 10.1016/j.renene.2021.02.047.
[166] “Performance analysis of open, closed and hybrid OTEC cycles based on working fluid type and system location - McDowellDylan_Fall2022_508CompliantCopy - California State University, Sacramento.” Accessed: Jun. 23, 2025. [Online]. Available: https://s3.amazonaws.com/na-st01.ext.exlibrisgroup.com/01CALS_USL/storage/alma/3E/84/B7/4C/7E/40/7C/B5/41/3B/69/B0/55/28/BE/2A/McDowellDylan_Fall2022_508CompliantCopy.pdf?response-content-type=application%2Fpdf&X-Amz-Algorithm=AWS4-HMAC-SHA256&X-Amz-Date=20250623T153538Z&X-Amz-SignedHeaders=host&X-Amz-Expires=119&X-Amz-Credential=AKIAJN6NPMNGJALPPWAQ%2F20250623%2Fus-east-1%2Fs3%2Faws4_request&X-Amz-Signature=191ae48b1b58b70e3532705c3132c771cec0f3f00ffe98a7eaabc27541eb5b92
[167] M. Al-Salmi, M. Laqbaqbi, S. Al-Obaidani, R. S. Al-Maamari, M. Khayet, and M. Al-Abri, “Application of membrane distillation for the treatment of oil field produced water,” *Desalination*, vol. 494, p. 114678, Nov. 2020, doi: 10.1016/j.desal.2020.114678.
[168] C. M. Tolentino Filho, R. de S. Silva, C. D. Á. K. Cavalcanti, M. A. Granato, R. A. F. Machado, and C. Marangoni, “Membrane distillation for the recovery textile

wastewater: Influence of dye concentration," *J. Water Process Eng.*, vol. 46, p. 102611, Apr. 2022, doi: 10.1016/j.jwpe.2022.102611.
[169] M. B. Abid, R. A. Wahab, M. A. Salam, I. A. Moujdin, and L. Gzara, "Desalination technologies, membrane distillation, and electrospinning, an overview," *Heliyon*, vol. 9, no. 2, p. e12810, Feb. 2023, doi: 10.1016/j.heliyon.2023.e12810.
[170] S. M. Shalaby *et al.*, "Membrane distillation driven by solar energy: A review," *J. Clean. Prod.*, vol. 366, p. 132949, Sep. 2022, doi: 10.1016/j.jclepro.2022.132949.
[171] X. Zhu *et al.*, "Geothermal direct contact membrane distillation system for purifying brackish water," *Desalination*, vol. 500, p. 114887, Mar. 2021, doi: 10.1016/j.desal.2020.114887.
[172] E. U. Khan, Å. Nordberg, and P. Malmros, "Waste Heat Driven Integrated Membrane Distillation for Concentrating Nutrients and Process Water Recovery at a Thermophilic Biogas Plant," *Sustainability*, vol. 14, no. 20, Art. no. 20, Jan. 2022, doi: 10.3390/su142013535.
[173] H. J. Hwang, K. He, S. Gray, J. Zhang, and I. S. Moon, "Direct contact membrane distillation (DCMD): Experimental study on the commercial PTFE membrane and modeling," *J. Membr. Sci.*, vol. 371, no. 1, pp. 90–98, Apr. 2011, doi: 10.1016/j.memsci.2011.01.020.
[174] B. B. Ashoor, S. Mansour, A. Giwa, V. Dufour, and S. W. Hasan, "Principles and applications of direct contact membrane distillation (DCMD): A comprehensive review," *Desalination*, vol. 398, pp. 222–246, Nov. 2016, doi: 10.1016/j.desal.2016.07.043.
[175] V. T. Shahu and S. B. Thombre, "Air gap membrane distillation: A review," *J. Renew. Sustain. Energy*, vol. 11, no. 4, p. 045901, Jul. 2019, doi: 10.1063/1.5063766.
[176] I. Janajreh, K. El Kadi, R. Hashaikeh, and R. Ahmed, "Numerical investigation of air gap membrane distillation (AGMD): Seeking optimal performance," *Desalination*, vol. 424, pp. 122–130, Dec. 2017, doi: 10.1016/j.desal.2017.10.001.
[177] R. Baghel, S. Upadhyaya, K. Singh, S. P. Chaurasia, A. B. Gupta, and R. K. Dohare, "A review on membrane applications and transport mechanisms in vacuum membrane distillation," *Rev. Chem. Eng.*, vol. 34, no. 1, pp. 73–106, Jan. 2018, doi: 10.1515/revce-2016-0050.
[178] M. A. E.-R. Abu-Zeid, Y. Zhang, H. Dong, L. Zhang, H.-L. Chen, and L. Hou, "A comprehensive review of vacuum membrane distillation technique," *Desalination*, vol. 356, pp. 1–14, Jan. 2015, doi: 10.1016/j.desal.2014.10.033.
[179] N. N. Safi *et al.*, "A Systematic Framework for Optimizing a Sweeping Gas Membrane Distillation (SGMD)," *Membranes*, vol. 10, no. 10, Art. no. 10, Oct. 2020, doi: 10.3390/membranes10100254.
[180] I. A. Said, T. Chomiak, J. Floyd, and Q. Li, "Sweeping gas membrane distillation (SGMD) for wastewater treatment, concentration, and desalination: A comprehensive review," *Chem. Eng. Process. - Process Intensif.*, vol. 153, p. 107960, Jul. 2020, doi: 10.1016/j.cep.2020.107960.
[181] Y. Chen, S. Yang, Z. Wang, and M. Elimelech, "Transforming membrane distillation to a membraneless fabric distillation for desalination," *Nat. Water*, vol. 2, no. 1, pp. 52–61, Jan. 2024, doi: 10.1038/s44221-023-00174-6.

[182] W. P. Parker, J. D. Kocher, and A. K. Menon, “Brine concentration using air gap diffusion distillation: A performance model and cost comparison with membrane distillation for high salinity desalination,” *Desalination*, vol. 580, p. 117560, Jul. 2024, doi: 10.1016/j.desal.2024.117560.
[183] M. Baghbanzadeh, D. Rana, C. Q. Lan, and T. Matsuura, “Zero thermal input membrane distillation, a zero-waste and sustainable solution for freshwater shortage,” *Appl. Energy*, vol. 187, pp. 910–928, Feb. 2017, doi: 10.1016/j.apenergy.2016.10.142.
[184] N. O. of D. and Informatics, “Water.” Accessed: Jun. 24, 2025. [Online]. Available: https://webbook.nist.gov/cgi/cbook.cgi?ID=C7732185&Mask=4&Type=ANTOINE&Plot=on%20(stull,%201947)
[185] *Seasave*. (2017). Sea-Bird Scientific. [Online]. Available: https://www.seabird.com/software/seasave-v7/family-downloads
[186] J. Cai and F. Guo, “Study of mass transfer coefficient in membrane desalination,” *Desalination*, vol. 407, pp. 46–51, Apr. 2017, doi: 10.1016/j.desal.2016.12.013.
[187] P. López-Porfiri, S. Ramos-Paredes, P. Núñez, and P. Gorgojo, “Towards the technological maturity of membrane distillation: the MD module performance curve,” *Npj Clean Water*, vol. 6, no. 1, pp. 1–9, Mar. 2023, doi: 10.1038/s41545-023-00234-0.
[188] M. Tian, Y. Yin, Y. Zhang, and L. Han, “Membrane distillation goes green: Advancements in green membrane preparation and renewable energy utilization,” *Desalination*, vol. 597, p. 118344, Mar. 2025, doi: 10.1016/j.desal.2024.118344.
[189] A. Alenezi and Y. Alabaiadly, “Emerging technologies in water desalination: A review and future outlook,” *Energy Nexus*, vol. 17, p. 100373, Mar. 2025, doi: 10.1016/j.nexus.2025.100373.
[190] A. Christou *et al.*, “Sustainable wastewater reuse for agriculture,” *Nat. Rev. Earth Environ.*, vol. 5, no. 7, pp. 504–521, Jul. 2024, doi: 10.1038/s43017-024-00560-y.
[191] M. G. O’Connell, N. Rajendran, M. Elimelech, J. Gilron, and J. B. Dunn, “Analysis of energy, water, land and cost implications of zero and minimal liquid discharge desalination technologies,” *Nat. Water*, vol. 2, no. 11, pp. 1116–1127, Nov. 2024, doi: 10.1038/s44221-024-00327-1.
[192] H. Quon and S. Jiang, “Decision making for implementing non-traditional water sources: a review of challenges and potential solutions,” *Npj Clean Water*, vol. 6, no. 1, pp. 1–14, Aug. 2023, doi: 10.1038/s41545-023-00273-7.
[193] T. Oki and S. Kanae, “Global Hydrological Cycles and World Water Resources,” *Science*, vol. 313, no. 5790, pp. 1068–1072, Aug. 2006, doi: 10.1126/science.1128845.
[194] T. G. Huntington, “Evidence for intensification of the global water cycle: Review and synthesis,” *J. Hydrol.*, vol. 319, no. 1, pp. 83–95, Mar. 2006, doi: 10.1016/j.jhydrol.2005.07.003.
[195] H. Quon and S. Jiang, “Decision making for implementing non-traditional water sources: a review of challenges and potential solutions,” *Npj Clean Water*, vol. 6, no. 1, pp. 1–14, Aug. 2023, doi: 10.1038/s41545-023-00273-7.
[196] P. López-Porfiri, S. Ramos-Paredes, P. Núñez, and P. Gorgojo, “Towards the technological maturity of membrane distillation: the MD module performance

curve," *Npj Clean Water*, vol. 6, no. 1, pp. 1–9, Mar. 2023, doi: 10.1038/s41545-023-00234-0.
[197] K. J. Lu, Z. L. Cheng, J. Chang, L. Luo, and T.-S. Chung, "Design of zero liquid discharge desalination (ZLDD) systems consisting of freeze desalination, membrane distillation, and crystallization powered by green energies," *Desalination*, vol. 458, pp. 66–75, May 2019, doi: 10.1016/j.desal.2019.02.001.
[198] C. Liu, L. Zhu, R. Ji, and H. Xiong, "Zero liquid discharge treatment of brackish water by membrane distillation system: Influencing mechanism of antiscalants on scaling mitigation and biofilm formation," *Sep. Purif. Technol.*, vol. 282, p. 120157, Feb. 2022, doi: 10.1016/j.seppur.2021.120157.
[199] T. Tong and M. Elimelech, "The Global Rise of Zero Liquid Discharge for Wastewater Management: Drivers, Technologies, and Future Directions," *Environ. Sci. Technol.*, vol. 50, no. 13, pp. 6846–6855, Jul. 2016, doi: 10.1021/acs.est.6b01000.
[200] G. Zaragoza, J. A. Andrés-Mañas, and A. Ruiz-Aguirre, "Commercial scale membrane distillation for solar desalination," *Npj Clean Water*, vol. 1, no. 1, pp. 1–6, Oct. 2018, doi: 10.1038/s41545-018-0020-z.
[201] A. Alkhudhiri, N. Darwish, and N. Hilal, "Membrane distillation: A comprehensive review," *Desalination*, vol. 287, pp. 2–18, Feb. 2012, doi: 10.1016/j.desal.2011.08.027.
[202] M. Rezaei, D. M. Warsinger, J. H. Lienhard V, M. C. Duke, T. Matsuura, and W. M. Samhaber, "Wetting phenomena in membrane distillation: Mechanisms, reversal, and prevention," *Water Res.*, vol. 139, pp. 329–352, Aug. 2018, doi: 10.1016/j.watres.2018.03.058.
[203] O. R. Lokare, S. Tavakkoli, V. Khanna, and R. D. Vidic, "Importance of feed recirculation for the overall energy consumption in membrane distillation systems," *Desalination*, vol. 428, pp. 250–254, Feb. 2018, doi: 10.1016/j.desal.2017.11.037.
[204] F. Banat, N. Jwaied, M. Rommel, J. Koschikowski, and M. Wieghaus, "Performance evaluation of the 'large SMADES' autonomous desalination solar-driven membrane distillation plant in Aqaba, Jordan," *Desalination*, vol. 217, no. 1, pp. 17–28, Nov. 2007, doi: 10.1016/j.desal.2006.11.027.
[205] H. C. Duong, P. Cooper, B. Nelemans, T. Y. Cath, and L. D. Nghiem, "Evaluating energy consumption of air gap membrane distillation for seawater desalination at pilot scale level," *Sep. Purif. Technol.*, vol. 166, pp. 55–62, Jun. 2016, doi: 10.1016/j.seppur.2016.04.014.
[206] J. Koschikowski, M. Wieghaus, and M. Rommel, "Solar thermal-driven desalination plants based on membrane distillation," *Desalination*, vol. 156, no. 1, pp. 295–304, Aug. 2003, doi: 10.1016/S0011-9164(03)00360-6.
[207] R. Ullah *et al.*, "Energy efficiency of direct contact membrane distillation," *Desalination*, vol. 433, pp. 56–67, May 2018, doi: 10.1016/j.desal.2018.01.025.
[208] P. López-Porfiri, S. Ramos-Paredes, P. Núñez, and P. Gorgojo, "Towards the technological maturity of membrane distillation: the MD module performance curve," *Npj Clean Water*, vol. 6, no. 1, pp. 1–9, Mar. 2023, doi: 10.1038/s41545-023-00234-0.

[209] L. Francis, F. E. Ahmed, and N. Hilal, “Advances in Membrane Distillation Module Configurations,” *Membranes*, vol. 12, no. 1, p. 81, Jan. 2022, doi: 10.3390/membranes12010081.
[210] S. Parani and O. S. Oluwafemi, “Membrane Distillation: Recent Configurations, Membrane Surface Engineering, and Applications,” *Membranes*, vol. 11, no. 12, Art. no. 12, Dec. 2021, doi: 10.3390/membranes11120934.
[211] L. MARTÍNEZ-DÍEZ, FLORIDO-DÍAZ ,F. J., and M. I. and VÁZQUEZ-GONZÁLEZ, “Study of Polarization Phenomena in Membrane Distillation of Aqueous Salt Solutions,” *Sep. Sci. Technol.*, vol. 35, no. 10, pp. 1485–1501, Jan. 2000, doi: 10.1081/SS-100100237.
[212] H. Bi, H. Yuan, Z. Xu, Z. Liang, and Y. Du, “Research on the Performance and Computational Fluid Dynamics Numerical Simulation of Plate Air Gap Membrane Distillation Module,” *Membranes*, vol. 14, no. 8, Art. no. 8, Aug. 2024, doi: 10.3390/membranes14080162.
[213] J. Phattaranawik, R. Jiraratananon, and A. G. Fane, “Heat transport and membrane distillation coefficients in direct contact membrane distillation,” *J. Membr. Sci.*, vol. 212, no. 1, pp. 177–193, Feb. 2003, doi: 10.1016/S0376-7388(02)00498-2.
[214] M. R. Elmarghany, A. H. El-Shazly, M. S. Salem, M. N. Sabry, and N. Nady, “Thermal analysis evaluation of direct contact membrane distillation system,” *Case Stud. Therm. Eng.*, vol. 13, p. 100377, Mar. 2019, doi: 10.1016/j.csite.2018.100377.
[215] H. C. Duong, P. Cooper, B. Nelemans, T. Y. Cath, and L. D. Nghiem, “Evaluating energy consumption of air gap membrane distillation for seawater desalination at pilot scale level,” *Sep. Purif. Technol.*, vol. 166, pp. 55–62, Jun. 2016, doi: 10.1016/j.seppur.2016.04.014.
[216] M. Khayet and C. Cojocaru, “Air gap membrane distillation: Desalination, modeling and optimization,” *Desalination*, vol. 287, pp. 138–145, Feb. 2012, doi: 10.1016/j.desal.2011.09.017.
[217] Q. Guo *et al.*, “Enhancement and optimization of membrane distillation processes: A systematic review of influential mechanisms, optimization and applications,” *Desalination*, vol. 586, p. 117862, Oct. 2024, doi: 10.1016/j.desal.2024.117862.
[218] A. Zhu, P. D. Christofides, and Y. Cohen, “Energy Consumption Optimization of Reverse Osmosis Membrane Water Desalination Subject to Feed Salinity Fluctuation,” *Ind. Eng. Chem. Res.*, vol. 48, no. 21, pp. 9581–9589, Nov. 2009, doi: 10.1021/ie900729x.
[219] E. Ali, “Optimal Control of a Reverse Osmosis Plant for Brackish Water Desalination Driven by Intermittent Wind Power,” *Membranes*, vol. 12, no. 4, p. 375, Mar. 2022, doi: 10.3390/membranes12040375.
[220] Q. Zhang, A. Jiang, M. Gong, H. Wang, J. Wang, and S. Jiangzhou, “Real Time Operational Optimization of a Seawater Desalination System Based on Rolling Prediction of Hourly Freshwater Demand,” *Ind. Eng. Chem. Res.*, vol. 57, no. 31, pp. 10528–10538, Aug. 2018, doi: 10.1021/acs.iecr.8b01449.
[221] J. D. Gil, A. Bueso, L. Roca, G. Zaragoza, and M. Berenguel, “Data-driven online feedback optimization of solar membrane distillation systems operating in batch mode,” *J. Process Control*, vol. 129, p. 103056, Sep. 2023, doi: 10.1016/j.jprocont.2023.103056.

[222] L. Eykens, I. Hitsov, K. De Sitter, C. Dotremont, L. Pinoy, and B. Van der Bruggen, "Direct contact and air gap membrane distillation: Differences and similarities between lab and pilot scale," *Desalination*, vol. 422, pp. 91–100, Nov. 2017, doi: 10.1016/j.desal.2017.08.018.
[223] M. Khayet, P. Godino, and J. I. Mengual, "Theory and experiments on sweeping gas membrane distillation," *J. Membr. Sci.*, vol. 165, no. 2, pp. 261–272, Feb. 2000, doi: 10.1016/S0376-7388(99)00236-7.
[224] A. F. Reza, R. Singh, R. K. Verma, A. Singh, Y.-H. Ahn, and S. S. Ray, "An integral and multidimensional review on multi-layer perceptron as an emerging tool in the field of water treatment and desalination processes," *Desalination*, vol. 586, p. 117849, Oct. 2024, doi: 10.1016/j.desal.2024.117849.
[225] Q. He, H. Zheng, X. Ma, L. Wang, H. Kong, and Z. Zhu, "Artificial intelligence application in a renewable energy-driven desalination system: A critical review," *Energy AI*, vol. 7, p. 100123, Jan. 2022, doi: 10.1016/j.egyai.2021.100123.
[226] M. Ibnouf, H. Jaber, H. Abukhalifeh, M. Ghazal, M. Ramadan, and M. Alkhedher, "A Comprehensive Review of AI Algorithms for Performance Prediction, Optimization, and Process Control in Desalination Systems," *Desalination Water Treat.*, vol. 321, p. 100892, Jan. 2025, doi: 10.1016/j.dwt.2024.100892.
[227] W. He, X. Luo, O. Kiselychnyk, J. Wang, and M. H. Shaheed, "Maximum power point tracking (MPPT) control of pressure retarded osmosis (PRO) salinity power plant: Development and comparison of different techniques," *Desalination*, vol. 389, pp. 187–196, Jul. 2016, doi: 10.1016/j.desal.2016.01.022.
[228] H. H. H. Mousa, A.-R. Youssef, and E. E. M. Mohamed, "State of the art perturb and observe MPPT algorithms based wind energy conversion systems: A technology review," *Int. J. Electr. Power Energy Syst.*, vol. 126, p. 106598, Mar. 2021, doi: 10.1016/j.ijepes.2020.106598.
[229] E. Ayala and S. Simani, "Perturb and Observe Maximum Power Point Tracking Algorithm for Permanent Magnet Synchronous Generator Wind Turbine Systems," in *15th European Workshop on Advanced Control and Diagnosis (ACD 2019)*, E. Zattoni, S. Simani, and G. Conte, Eds., Cham: Springer International Publishing, 2022, pp. 1007–1017. doi: 10.1007/978-3-030-85318-1_59.
[230] I. Toumi *et al.*, "Robust Variable-Step Perturb-and-Observe Sliding Mode Controller for Grid-Connected Wind-Energy-Conversion Systems," *Entropy*, vol. 24, no. 5, Art. no. 5, May 2022, doi: 10.3390/e24050731.
[231] G. Guan, X. Yang, R. Wang, R. Field, and A. G. Fane, "Evaluation of hollow fiber-based direct contact and vacuum membrane distillation systems using aspen process simulation," *J. Membr. Sci.*, vol. 464, pp. 127–139, Aug. 2014, doi: 10.1016/j.memsci.2014.03.054.
[232] N. Dow *et al.*, "Pilot trial of membrane distillation driven by low grade waste heat: Membrane fouling and energy assessment," *Desalination*, vol. 391, pp. 30–42, Aug. 2016, doi: 10.1016/j.desal.2016.01.023.
[233] A. Criscuoli, M. C. Carnevale, and E. Drioli, "Modeling the performance of flat and capillary membrane modules in vacuum membrane distillation," *J. Membr. Sci.*, vol. 447, pp. 369–375, Nov. 2013, doi: 10.1016/j.memsci.2013.07.044.

[234] M. I. Ali, E. K. Summers, H. A. Arafat, and J. H. L. V, “Effects of membrane properties on water production cost in small scale membrane distillation systems,” *Desalination*, vol. 306, pp. 60–71, Nov. 2012, doi: 10.1016/j.desal.2012.07.043.
[235] G. Zakrzewska-Trznadel, M. Harasimowicz, and A. G. Chmielewski, “Concentration of radioactive components in liquid low-level radioactive waste by membrane distillation,” *J. Membr. Sci.*, vol. 163, no. 2, pp. 257–264, Nov. 1999, doi: 10.1016/S0376-7388(99)00171-4.